Design Aspects of a Failure Resistant 70 MPa Type IV Composite Overwrapped Pressure Vessels for Hydrogen Storage

A Thesis Submitted

in Partial Fulfilment of the Requirements

for the Degree of

DOCTOR OF PHILOSOPHY

by

Mukesh Kumar

(2017MEZ0017)



DEPARTMENT OF MECHANICAL ENGINEERING
INDIAN INSTITUTE OF TECHNOLOGY ROPAR

October, 2024

 $Mukesh\ Kumar$ Copyright ©2024, Indian Institute of Technology Ropar All Rights Reserved

This thesis is dedicated to my teachers and parents (For their endless love, support, and encouragement)

Declaration of Originality

I hereby declare that the work being presented in the thesis entitled **Design Aspects** of a Failure Resistant 70 MPa Type IV Composite Overwrapped Pressure Vessels for Hydrogen Storage has been solely authored by me. It presents the result of my independent investigation and research conducted during the period from January 2018 to June 2024 under the supervision of Dr. Dhiraj K. Mahajan, Associate Professor, Department of Mechanical Engineering. To the best of my knowledge, it is an original work, both in terms of research content and narrative, and has not been submitted or accepted elsewhere, in part or in full, for the award of any degree, diploma, fellowship, associateship, or similar title of any university or institution. Further, due credit has been attributed to the relevant state-of-the-art, collaborations with appropriate citations and acknowledgments, in line with established ethical norms and practices. I also declare that any idea, data, fact, or source stated in my thesis has not been fabricated, falsified, or misrepresented. All the principles of academic honesty and integrity have been followed. I fully understand that if the thesis is found to be unoriginal, fabricated, or plagiarized, the Institute reserves the right to withdraw the thesis from its archive and revoke the associated Degree conferred. Additionally, the Institute also reserves the right to appraise all concerned sections of society of the matter for their information and necessary action. If accepted, I hereby consent for my thesis to be available online in the Institute's Open Access repository, on an inter-library loan, and the title & abstract to be made available to outside organizations.

Signature

Name: Mukesh Kumar

Entry Number: 2017MEZ0017

Program: PhD

Department: Mechanical Engineering Indian Institute of Technology Ropar

Mukesh kuman.

Rupnagar, Punjab 140001

Date: 24/10/2024

Acknowledgement

I would like to express my heartfelt gratitude to the individuals whose unwavering support and guidance have been indispensable during my tenure as a PhD candidate. First and foremost, my deepest appreciation goes to my advisor and mentor, Dr. Dhiraj K. Mahajan, whose guidance, patience, and encouragement have been instrumental in my academic journey.

I extend my sincere thanks to my esteemed doctoral committee members: Dr. Amar Nath Roy Chaudhary, Dr. Manish Agrawal, and Dr. Samir Chandra Roy. Their consistent assessment of my progress and the invaluable feedback and suggestions they provided on a timely basis has been immensely beneficial.

A heartfelt thank you goes out to my friends, lab mates, and colleagues—Tushita Rohilla and her family members, Vishal Singh, Rakesh Kumar, Navneet Singh, Dharmendra Kumar Tyagi, Gaje Singh, M.Tech. juniors, and many others, who have been my companions on this remarkable and fruitful journey toward my PhD at IIT Ropar.

I wish to extend my sincere thanks to the Ministry of Human Resource Development, Project IMPRINT-5815, Government of India, for providing support during the initial years of my PhD. I also thank the Indian Institute of Technology Ropar for providing the Institute Fellowship for this research.

Finally, I extend my profound gratitude to my mother, father, wife, and my lovely son Shivansh and daughter Manashvi. Without their unwavering love and support, completing this PhD work would not have been possible. They consistently provided me with a conducive environment for concentration during this significant period of my life.

Thank you Mukesh Kumar

Certificate

This is to certify that the thesis titled Design Aspects of a Failure Resistant 70 MPa Type IV Composite Overwrapped Pressure Vessels for Hydrogen Storage, submitted by Mukesh Kumar (2017MEZ0017) for the award of the degree of Doctor of Philosophy at Indian Institute of Technology Ropar, is a record of bonafide research work carried out under my guidance and supervision. To the best of my knowledge and belief, the work presented in this thesis is original and has not been submitted, either in part or full, for the award of any other degree, diploma, fellowship, associateship, or similar title at any other university or institution.

In my opinion, the thesis has reached the standard fulfilling the requirements of the regulations relating to the Degree.

Signature of the Supervisor

Dr. Dhiraj K. Mahajan

Department of Mechanical Engineering Indian Institute of Technology Ropar

Rupnagar, Punjab 140001

Date: 24/10/2024

Lay Summary

Hydrogen has emerged as a zero-emission solution for light to heavy-duty transport as well as various stationary applications. Type IV composite overwrapped pressure vessels (COPVs) are standardized to store gaseous hydrogen (H₂) at a nominal working pressure (p_{nwp}) of up to 70 MPa or more so as to achieve a competitive driving range for commercially available hydrogen fuel cell electric vehicles (HFCEVs) and hydrogen internal combustion engine vehicles (HICEVs). As per various national and international standards, Type IV COPVs are tested up to the burst pressure (p_b) which is around 2.25 times of p_{nwp} to provide a sufficient factor of safety for regular operations at p_{nwp} .

Although Type IV COPV for H₂ storage has been standardized and commercialized, there are several challenges associated with it such as high cost, limited temperature range of usage, safety, etc. which are linked to the materials, design, and manufacturing processes used to fabricate these COPVs. Therefore, a good understanding of the role of materials used for their manufacturing, design along with the manufacturing defects on their failure behavior under critical operational conditions of high-pressure H₂ is absolutely necessary. Materials used for manufacturing Type IV COPV include hydrogen embrittlement resistant metals used for the manufacturing boss (required for holding the gas filling valve), a suitable grade of polymer used for manufacturing liner to control the H₂ permeation, and carbon fiber-reinforced plastic (CFRP) that has a suitable matrix material along with the suitable grade of fibers as reinforcement to provide the required strength for holding high-pressure H₂. Design aspects of COPVs include length to diameter ratio, shape of dome section and coupling of metallic boss with polymeric liner. Manufacturing defects on the other hand, can include defects in the polymeric liner, gaps at the interface of various components of COPV, sharp thickness variation in CFRP winding, etc. These defects are known to cause several kinds of failures in Type IV COPVs that include buckling of the liner, reduced p_b , leakage of gas, as well as an overall reduction in the operational life.

This thesis aims to address the critical challenges of developing a failure resistant Type IV COPV with p_{nwp} of 70 MPa focusing on materials, design aspects, and manufacturing defects. A computational framework is developed that considers manufacturing defects, and design variation and correctly accounts for H_2 permeation in the liner material to significantly improve our understanding of complex phenomena happening in Type IV COPVs during operational life. At first, a small Type IV COPV with an internal water volume of 18 liter is designed progressively using netting analysis, classical laminate theory, and finite element analysis, to elucidate the role of design parameters and defects responsible for its failure at the p_b . Next, a novel hydrogen transport model has been developed to investigate the transport behavior of hydrogen in polymer liner material to predict the optimal thickness of the liner required to control the H_2 permeation. Lastly, the role of defects in polymer liner and at the liner-composite interface has been analyzed

under the filling-defilling cycles of Type IV COPVs.

Abstract

Hydrogen has emerged as a zero-emission solution for light to heavy-duty transport as well as various stationary applications. Type IV composite overwrapped pressure vessels (COPVs) are standardized to store gaseous hydrogen (H₂) at a nominal working pressure (p_{nwp}) of up to 70 MPa or more so as to achieve a competitive driving range for commercially available hydrogen fuel cell electric vehicles (HFCEVs) and hydrogen internal combustion engine vehicles (HICEVs). As per various national and international standards, Type IV COPVs are tested up to the burst pressure (p_b) which is around 2.25 times of p_{nwp} to provide a sufficient factor of safety for regular operations at p_{nwp} .

Although Type IV COPV for H₂ storage has been standardized and commercialized, there are several challenges associated with it such as high cost, limited temperature range of usage, safety, etc. which are linked to the materials, design, and manufacturing processes used to fabricate these COPVs. Therefore, a good understanding of the role of materials used for their manufacturing, design along with the manufacturing defects on their failure behavior under critical operational conditions of high-pressure H₂ is absolutely necessary. Materials used for manufacturing Type IV COPV include hydrogen embrittlement resistant metals used for the manufacturing boss (required for holding the gas valve), a suitable grade of polymer used for manufacturing liner to control the H₂ permeation, and carbon fiber-reinforced plastic (CFRP) that has a suitable matrix material along with the suitable grade of fibers as reinforcement to provide the required strength for holding high-pressure H₂. Design aspects of COPVs include length to diameter ratio, shape of dome section and coupling of metallic boss with polymeric liner. Manufacturing defects on the other hand, can include defects in the polymeric liner, gaps at the interface of various components of COPV, sharp thickness variation in CFRP winding, etc. These defects are known to cause several kinds of failures in Type IV COPVs that include buckling of the liner, reduced p_b , leakage of gas, as well as an overall reduction in the operational life.

To gain a competitive edge on Type IV COPVs, simulation-assisted manufacturing technologies must be developed to reduce test requirements, boost production rates, and reduce rejections or failures under service conditions. To improve such understanding, in this thesis, at first a small Type IV COPV with an internal water volume of 18 liter is designed progressively using netting analysis, classical laminate theory, and finite element analysis, to elucidate the role of various design parameters and defects responsible for its failure at the p_b . The failure behavior of Type IV COPV is found to be highly sensitive to the placement of the CFRP lay-up, the outer shape of the metallic boss that interacted with the CFRP winding while the junction points of the liner, boss, and CFRP winding are shown to be the hot spots for failure. Lastly, failure prevention strategies at these hot spots are discussed in terms of the CFRP failure criteria.

Next, a novel modeling framework is developed and implemented using UMATHT (user-defined material with heat transfer) subroutines in the commercial FE solver Abaqus. UMATHT is used to solve the H_2 permeation equation, following the analogy between heat transfer and the diffusion equation. The variation in hydrogen transport properties in liner material based on the morphological properties of polymer with applied pressure has been implemented in the model to investigate the H_2 permeation mechanism. The developed modeling framework is first calibrated w.r.t experimental data available in the literature, and thereafter, the model with calibrated constants is extended to simulate the optimal thickness of liner material for a 70 MPa p_{nwp} Type IV COPV.

Lastly, to explore the mechanism of $\rm H_2$ permeation and failure based on pre-existing micro-defects in the polymeric liner material, two defect cases are considered for analyzing the role of defects in polymer liner and at liner-composite interface under filling-defilling cycles of Type IV COPVs. A quarter model of the cross-section of cylindrical part of the Type IV COPV with both the defects incorporated is subjected to an operational filling and defilling cycle typically associated with Type IV COPV. A multi-variable $\rm H_2$ permeation analysis is conducted using the extended governing equations of Fick's law for hyper-elastic polymeric liner material and defilling-induced blistering model. Filling is carried out up to 70 MPa in 5 minutes, and maintained for several hours, then fast defilling is carried up to a minimum pressure up to 2 MPa as followed in realistic situations. Simulation results provide an understanding of $\rm H_2$ pressure build-up inside defects during the filling and defilling cycle clearly highlighting the effect of location of micro-defects on damage initiation under operational conditions of Type IV COPVs.

List of Publications

Journal Publications

- Mukesh Kumar, and Dhiraj K. Mahajan, Role of Design and Manufacturing Defects on Failure Behavior of Type IV COPV for H₂ Storage (To be Submitted)
- Mukesh Kumar, and Dhiraj K. Mahajan, Modeling of H₂ Permeation in Liner Materials of Type IV Composite Overwrapped Pressure Vessel (To be Submitted)
- Mukesh Kumar, and Dhiraj K. Mahajan, Role of Micro-Defects on Blistering Behavior of 70 MPa Type IV Composite Overwrapped Pressure Vessels due to H₂ Permeation (To be Submitted)

Patent

Dhiraj K. Mahajan, Srikant Shekhar Padhee, Ravi Mohan Prasad and Mukesh Kumar, A Leak Proof Liner-Boss Assembly for Type IV Hydrogen Storage Tank, Patent Grant No. 478710, Application No. IN202011022281, Date of Grant: 07/12/2023, Country of filing: India.

International and National Conferences

- Mukesh Kumar, Dhiraj K. Mahajan, Role of Polymeric Liner Defect on Failure Behavior of Type IV Composite Overwrapped Pressure Vessels. ASATM-2023, 11th to 13th January 2023, NTU Singapore
- Mukesh Kumar, Dhiraj K. Mahajan, Modeling of Hydrogen Permeation in Liner Materials of Type IV Composite Overwrapped Pressure Vessels, National Conference on Energy Materials and Devices, 16th to 18th December 2022, Department of Physics, IIT Jodhpur, Rajasthan, India
- Mukesh Kumar, Srikant Shekhar Padhee, Ravi Mohan Prasad and Dhiraj K. Mahajan, Design, Development, and Demonstration of Indigenous 700-bar Type IV Hydrogen Storage Tank for Mobile Applications, 8th International Engineering Sourcing Show (IESS VIII 2019), 14th to 16th March 2019, Chennai Trade Centre, Chennai-600089, India

Workshop

- Composite 4.0, 01st to 04th December 2022, IIT Kharagpur, Mechanical Engineering Department, IIT Kharagpur, India
- Energy Storage, The Future of Energy 11th to 15th March 2019, Centre for Energy and Environment, AICTE sponsored, MNIT Jaipur, Rajasthan-302017, India
- Automation of Finite Element Analysis from 23rd to 27th August 2019, Centre for Continuing Education, IIT Madras, India

Contents

D	eclar	ration	iv
\mathbf{A}	ckno	wledgement	\mathbf{v}
\mathbf{C}	ertifi	cate	vi
La	ay Su	ımmary	vii
\mathbf{A}	bstra	nct	ix
Li	st of	Publications	xi
Li	st of	'Figures x	vii
Li	st of	Tables	xxi
N	omei	nclature & Abbreviations xx	xiii
1	Inti	roduction	1
	1.1	Introduction	1
	1.2	Background and Motivation	4
		COPV	4
	1.3	Objectives and Scope	7
	1.4	Outline of the thesis	8
2	Lite	erature Review on Failure Study of High Pressure Type IV COPVs	11
	2.1	Introduction	11
	2.2	Design and Failure Study of Type IV COPVs	11
	2.3	Hydrogen Permeation-Induced Failure Study of Type IV COPVs	15
3		e of Manufacturing Defects on Failure Behavior of 70 MPa Type IV	
		${ m PV} \; { m for} \; { m H}_2 \; { m Storage}$	19
	3.1	Introduction	19
	3.2	Mathematical Formulation Used for Design of Type IV COPVs	22
		3.2.1 Prediction of composite thickness based on netting analysis	22
		3.2.2 Classical laminate theory based stress analysis	24
		3.2.3 Tsai-Wu failure index	26
		3.2.4 Stress ratio	27
	3.3	Design Aspects and Finite Element Method used for the Analysis of Type	
		IV COPV	27

References

		3.3.1	CAD model and material properties	27
		3.3.2	Boundary condition and meshing	30
		3.3.3	Manufacturing defects found and need to analyze using FEA $$	31
	3.4	Result	s	32
	3.5	Discus	ssion	41
	3.6	Conclu	usion	42
4	Mo	deling	of H_2 Permeation through the Liner Materials of 70 MPa Type	
	IV	COPV		45
	4.1	Introd	uction	45
	4.2	Mathe	ematical Modelling to Implement in FE Analysis	48
		4.2.1	Methods of permeability prediction and process of H ₂ diffusion	
			through polymeric liner material	48
		4.2.2	Governing equation for H_2 diffusion in terms of chemical potential .	49
		4.2.3	Henry's law for polymer-H ₂ interaction and time-lag method for	
			transport properties estimation	
		4.2.4	Effect of concentration and pressure on diffusivity	
		4.2.5	Effect of crystallinity on diffusivity	
	4.3		odelling Framework to Validate the Experimental Results	
	4.4		and Discussion	
	4.5	Concli	usion	65
5			icro-Defects on Blistering Behavior in 70 MPa Type IV COPV	
		_	Permeation	67
	5.1		uction	
	5.2		ematical Model Used for the Analysis	
			Effect of hydrogen concentration on pressure buildup inside the defect	
	r 0	5.2.2	Effect of pore pressure inside the defect	
	5.3		odeling Framework	
		5.3.1	Pressurization-depressurization cycle of hydrogen for Type IV COPVs	
		5.3.2	Geometrical coupon sample with loading and boundary conditions.	
		5.3.3	Mesh and element type used for modeling COPV material and defect	12
		5.3.4	Material model used for polymeric liner, composite material, and defect	73
	5.4	Result	s and Discussion	73
	5.5	Conclu	usion	78
6	Cor	nclusio	n and Future Scope	7 9
	6.1	Conclu	usion	79
	6.2	Scope	for future studies	80

83

\mathbf{A}	App	pendix	103
	A.1	CFRP Winding Sequence Used for FW on Liner-boss Assembly of Type IV	
		COPV	. 103
	A.2	Finite Element Formulation of Hydrogen Transport Model for Polymeric	
		Liners in Type IV COPVs	. 104

List of Figures

1.1	Schematic of types of PVs for hydrogen storage with integrated parts and corresponding materials. The metallic boss, metallic liner, composite, and	
	polymeric liner are shown in red, black, gray, and green colors, respectively.	2
1.2	An illustration of a typical Type IV hydrogen COPV with a wall showing	
	the polymer liner core wrapped with fiber-reinforced composite [1]	3
1.3	Schematic of Type IV COPV under (a) buckling, (b) blistering, (c)	
	cavitation (scale mark is approximate) [2]	4
1.4	A schematic of (a) metallic boss, and (b) polymeric liner	5
1.5	(a) Polymer liner procured from Crompton Mouldings, U.K., and (b)	
	liner-boss assembly fabricated at IIT Ropar	5
1.6	Winding of CFRP on the liner-boss assembly during FW process	6
1.7	Curing of fabricated composite cylinder after wrapping to cure the epoxy	
	resin	7
1.8	(a) Picture of site preparation for burst test and (b) remote monitoring of	
	cylinder during burst test	8
3.1	A schematic of doily layer inserted with hoop and helical layers on liner-boss	
	assembly	20
3.2	A schematic flow diagram for design and analysis of Type IV COPV	22
3.3	Schematic of COPV with winding over (a) the polymeric liner part, (b)	
	only the dome part along with associated geometrical parameters, and (c)	
	free body diagram of a netting-based element	23
3.4	Schematic of CLT for (a) multi-layer lamina, (b) a schematic diagram with	
	local $(1,2)$ and global (X,Y) coordinate system	25
3.5	A 2-D CAD model of the liner-boss assembly of Type IV COPV used in	
	this study	27
3.6	A 3-D Type IV COPV model with integrated parts	28
3.7	Load and boundary condition used to simulate p_b test of Type IV COPV	30
3.8	Manufacturing defects considered in the liner-boss-composite model	31
3.9	(a) Contour plots of $F.I$ in composite layers, and (b) variation in the	
	F.I along the first helical and first hoop layer of Type IV COPV with	
	manufacturing defects considered as per case I	32
3.10	(a) Contour plots of von Mises stress in composite layers, and (b) variation	
	in the von Mises stress along the first helical and first hoop layer of Type	33
	IV COPV with manufacturing defects considered as per case I	5.3

3.11	Design of Type IV COPV with the removal of manufacturing defect D1 from $$	
	the cylindrical-dome part transition, with thickness buildup at different	
	locations for safer design for open dome part and closed dome part	34
3.12	Variation of $F.I$ of Type IV COPV with the removal of sharp transition at	
	dome-cylinder interface manufacturing defect (a) the contour plot variation,	
	and (b) the line plot for the first helical and hoop layer	35
3.13	von Mises stress distribution in composite layers and plastic liner after	
	removal of sharp transition at dome-cylinder interface manufacturing defect	
	(a) contour plot variation and (b) line plot for the first helical and hoop layer.	36
3.14	Type IV COPV axisymmetric model with sleeve material used to fill the	
	liner-boss-composite materials gap	36
3.15	F.I at multi-material interface of both end domes	37
3.16	Various composite-boss interface designs for the open dome end and closed	
	dome end, (a) pure cylindrical type, (b) cylindrical with curvature in	
	starting of the composite, (c) curvature provided with cylindrical profile	
	with more thickness	37
3.17	F.I variation for composite-boss interface designs for the open dome end and	
	closed dome end, (a) pure cylindrical type, (b) cylindrical with curvature in	
	starting of composite, (c) curvature provided with cylindrical profile with	
	more thickness	38
3.18	F.I for various profiles of boss shape	39
3.19	von Mises stress distribution in composite layers after removal of all	
	manufacturing defects (a) contour plot variation and (b) line plot for the	
	first helical and hoop layer	39
3.20	$F.I$ at various design pressures (minimum p_b to ultimate $p_{ult.}$ value)	40
4.1	An illustration of a typical Type IV H_2 COPV kept in a sealed chamber for	
4.1	permeation testing	45
4.2	A schematic of hydrogen transport modeling framework	
4.2	(a) H_2 interaction with the polymeric sample at a given state, (b) steps	41
4.0	involved in the diffusion process	49
4.4	H_2 interaction with polymeric coupon sample	51
4.5	H ₂ flux vs. time plot for permeation testing by the time-lag method	52
4.6	Diffusivity dependent on C and p w.r.t to its coefficient of semicrystalline	02
4.0	polymer	53
4.7	Morphology of semicrystalline polymer, consists of crystalline and	00
1.1	amorphous region	54
4.8	Schematic representation of rectangular coupon sample (a) geometric	94
4.0	parameters and physical loading condition, and (b) cartesian coordinate	
	system with boundary condition	57
4.9	Contour for C of H_2 across the thickness of the sample, corresponding to	91
1.0	an increase in pressure 10, 20, 30, 40, 50, 60, 70, 80, and 90 MPa	59

4.10	H_2 flux contour across the thickness of the sample with increases in pressure	
	with time at 10 MPa	60
4.11	Contour for H_2 flux for various pressures (a) till saturation reached and (b)	
	the unsteady state in zoomed view	60
4.12	Permeability variation with an increase in H_2 pressure for HDPE	61
4.13	Diffusivity variation with pressure for HDPE polymer sample	62
4.14	Solubility coefficient variation with pressure for HDPE polymer sample. $$	62
4.15	Variation of pressure affecting the crystallinity of polymer sample	63
4.16	Permeability coefficient variation with thickness at p_{nwp} of 70 MPa	64
4.17	Diffusivity coefficient variation with thickness of the sample, at p_{nwp} of 70	
	MPa	65
5.1	Typical pressurization-depressurization cycle of H_2 for Type IV COPVs	70
5.2	Schematic representation of (a) geometry, loading and boundary conditions,	
	and (b) location of defect in polymeric liner material	71
5.3	Schematic representation of (a) geometry, loading and boundary conditions,	
	and (b) location of defect at liner-composite interface	71
5.4	Contour for J (a) across the thickness of the sample, and (b) with defect	
	at the center of polymeric liner material	74
5.5	Contour for J (b) across the thickness of the sample, and (b) with defect	
	at the interface of liner-composite material	74
5.6	Pressure variation with time for the defect inside the polymer (p_{cd}) and	
	defect at the liner-composite interface (p_{psd}) concerning the similar applied	
	p_i for first cycle	75
5.7	Pressure variation with time for the defect inside the polymer (p_{cd}) and	
	defect at the liner-composite interface (p_{psd}) concerning the similar applied	
	p_i for two cycle	76
5.8	Concentration variation with time for the defect inside the polymer (C_{cd})	
	and defect at the liner-composite interface (C_{scd}) for single cycle	77

List of Tables

2.1	Various design parameters and failure criterion used for Type IV COPVs	13
2.2	Hydrogen permeation-induced failure study of Type IV COPVs material. $$.	17
3.1	Composite layup design description from netting analysis for a given load,	
	material, and geometrical parameters	25
3.2	Design parameters of liner-boss assembly with composite specifications used	
	for Type IV COPV design (all dimensions are in mm)	28
3.3	Mechanical properties of the metallic boss (Al6061-T6), matrix	
	(LY556-XY54) and polymeric liner (HDPE) material used for Type IV COPV.	29
3.4	Mechanical properties of T700S-12K-50C carbon fiber reinforcement and	
	composite lamina.	29
3.5	Strength properties of the composite lamina	30
3.6	Mechanical properties of the sleeve material	35
3.7	Design parameters of three profiles of open-end and closed-end bosses	
	studied in case IV	38
3.8	F.I for different cases considered for manufacturing defect	40
4.1	H_2 transport material properties of the polymeric liner material	54
4.2	HDPE crystallinity parameters require density, crystalline, and amorphous	
	region	55
4.3	FE mesh and element type specifications	58
4.4	Experimental data and FEA simulation study parameters for the various	
	pressures	64
5.1	Geometrical parameters used in the FE model	72
5.2	FE model parameters used in mesh model	72
5.3	Material model parameters used for polymeric liner, and defect	73
5.4	Modeling parameters used for polymeric liner, defect, and composite material.	73

Nomenclature & Abbreviations

β	Pressure coefficient
ϵ_o	Mid-plane strain vector
Δt	Time increment
η	Concentration coefficient
γ	Chain immobilization factor accounting for the amorphous part
μ	Chemical potential of hydrogen in the polymer
μ^0	Reference chemical potential
ϕ	Crystallinity of semicrystalline polymer
ϕ_f	Crystallinity of semicrystalline polymer after pressurization
ϕ_i	Crystallinity of semicrystalline polymer before pressurization
$ ho_a$	Amorphous phase density of polymeric material
$ ho_c$	Crystalline phase density of polymeric material
$ ho_s$	Semicrystalline density of polymeric material
σ_{90}	Stress in the hoop layer
σ_{lpha}	Stress in the helical layer
σ_{p_b}	Stress at p_b
σ_p	Stress at p_{nwp}
$ au_a$	Characteristic parameter accounted for the enhancement of diffusion path in polymeric material
J	Hydrogen flux
ζ	Coefficient of concentration expansion
A	Laminate extensional stiffness
A_f	Cross-sectional area of tow
В	Laminate coupling stiffness
C	Hydrogen concentration

 C_i Hydrogen concentration on inside boundary of the sample $C_O - C_t$ Concentration difference C_t Hydrogen concentration at time, t C_O Initial hydrogen concentration in material C_{o} Hydrogen concentration on the outside boundary of sample DLaminate bending stiffness dFilament diameter Overall diffusion coefficient for hydrogen in polymer D_o Diffusion coefficient for hydrogen in semicrystalline polymer D_{sc} Depressurization rate dpF.ITsai Wu failure index FV_f Free volume available in the polymer after pressurization FV_i Free volume available in the polymer before pressurization kCurvature vector LTotal length of the cylinder MResultant couple moment Order of polynomial of the Ogden model NFilament per tow nNumber of spool N_s Total number of layers n_t N_X Resultant force component in hoop direction Resultant force component in axial direction N_Y Number of helical layers n_{he} Number of hoop layers n_{ho} Burst pressure p_b Nominal working pressure p_{nwp} RUniversal gas constant

r Radial distance along the diameter which varies in the dome

 R_b Radius of the boss

 R_c Outer radius of the polymeric liner over which the filament is wound

 r_{iv} Internal radius of boss that interacts with the valve

SR Stress ratio

T Absolute temperature

 t_c Total thickness of composite in cylindrical part

 t_f Thickness of single tow fibers

 $t_h(r)$ Helical layer thickness buildup in the dome

 t_{90} Total hoop layer thickness

 t_{α} Total helical layer thickness

 V_f Fiber volume fraction

 V_H Partial molar volume of hydrogen in polymer

 W_f Bandwidth of single tow

1-D One dimensional

12000 12K

2-D Two dimensional

3-D Three dimensional

CF Carbon fiber

CFRP Carbon fiber reinforced plastic

CLT Classical laminate theory

COPV Composite overwrapped pressure vessel

EPDM Ethylene propylene diene monomer

FE Finite element

FEM Finite element method

FW Filament winding

GC Gas chromatography

H₂ Gaseous hydrogen

HDPE High-density polyethylene

HE Hydrogen embrittlement

HPHP High-pressure hydrogen permeation

hr Hour

HTM Hydrogen transport model

L Liters

LDPE Low-density polyethylene

LLDPE Linear low-density polyethylene

NA Netting analysis

NTP Normal temperature and pressure

PA6 Polyamide 6

PE Polyethylene

PET Polyethylene terephthalate

PU Polyurethane

RVE Representative volume element

s Second (sec)

TGA Thermal desorption analysis

UD Unidirectional

UMATHT User defined material for heat transfer

WA Winding angle

Chapter 1

Introduction

1.1 Introduction

The world is facing the greatest challenge of climate change due to the excessive use of fossil fuels (coal, oil, and natural gas). This has led to increased usage of renewable energy sources to meet the energy requirement. However, the irregular, seasonal variation of most known renewable sources (including solar, wind, geothermal, hydro, tidal, and biomass) leads to an imbalance between energy supply and demand. Green H₂ as a clean energy source overcomes both the shortcomings of conventional and renewable energy sources. It has thus been identified as the most important energy vector. It also has the highest specific energy (nearly 142 MJ/kg, almost 3 times more than gasoline). It generates water as a by-product, making it one of the most environment-friendly fuels, with the potential to fulfill all types of energy requirements for global needs [3, 4].

Green H_2 can be produced using any renewable energy source; however, its efficient utilization is significantly challenged due to issues associated with its value chain (such as cost of production, storage, transmission, utilization, and safety). One of the challenges for bulk H_2 production is storage and transportation for its effective utilization. Due to its low volumetric energy density, the volume required for storage at normal temperature and pressure (NTP) (20°C, 0.10 MPa) is quite large e.g., approximately 11,000 liters (L) water volume is required to store 1 kg of H_2 at NTP with a density of 0.09 kg/m³ [5]. For mobile applications, a typical hydrogen fuel cell electric vehicle (HFCEV) e.g. a sedan gives a mileage of 100 kms per kg of H_2 [6]. Thus storage of H_2 is required at very high pressures to be utilized for mobile applications such as as a fuel in hydrogen internal combustion engine vehicles (HICEV) or as an energy medium in the case of HFCEV. As an example, H_2 stored at 70 MPa requires 24 L of water volume to store 1 kg of H_2 at 20°C with a density of 42 Kg/m³ [7].

Based on the components of the gaseous H_2 storage pressure vessels (PVs), they are classified into four categories, i.e., Type I, Type II, Type III, and Type IV PVs, as illustrated in the schematic shown in Fig. 1.1. In Type I to Type III PVs (as shown in Fig. 1.1(a), 1.1(b), 1.1(c)), H_2 remains in physical contact with the metallic material that can cause hydrogen embrittlement (HE) at high pressure, thus limiting their storage capacity [8, 9]. Residual moisture in stored H_2 is prone to corrosion and HE, leading to the reduction in the strength and fracture toughness of metallic materials, which may lead

to catastrophic failure of Type I, Type II, and Type III PVs. In addition, a higher density of metals causes more weight, making them unsuitable for vehicular applications [10, 11]. Type II and Type III PVs have a carbon fiber reinforced plastic (CFRP) wrapped over the metallic liner to increase the pressure rating H₂ storage compared to Type I PV.

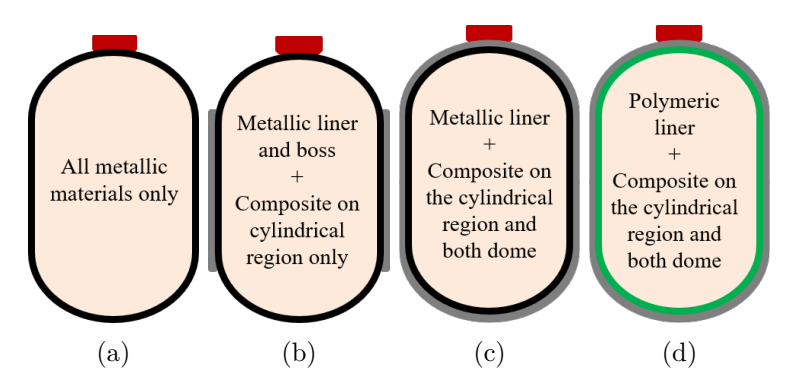


Figure 1.1: Schematic of types of PVs for hydrogen storage with integrated parts and corresponding materials. The metallic boss, metallic liner, composite, and polymeric liner are shown in red, black, gray, and green colors, respectively.

The most promising candidate for high-capacity gaseous H₂ storage is the Type IV composite overwrapped pressure vessel (COPV) as shown in Fig. 1.1(d) [5]. In Type IV COPVs, the polymeric liner material provides the H₂ permeation barrier, while high strength fibers (e.g. carbon fiber) based reinforced plastic composite winding envelops the liner-boss assembly to provide the required strength to hold highly pressurized H₂. These COPVs are standardized and utilized efficiently nowadays for various mobile applications (e.g., cars, buses, trains, drones) as onboard H₂ storage. Type IV COPVs offer several advantages compared to their counterparts, such as high gravimetric energy density, lightweight, improved cycle life, corrosion resistance, etc. However, there are also several challenges associated with it such as high cost, limited temperature range of usage, safety, etc. which are linked to the materials, design, and manufacturing processes used to fabricate these COPVs. These issues need to be solved to further improve their performance with regards to the storage capacity, safety, and applications by reducing the unit cost.

Due to the proprietary nature of work done by several companies who have commercialized Type IV COPVs, most of the parameters associated with the materials, design, and manufacturing processes such as H₂ permeability rate of polymeric liner material, boss-liner interface design, and composite wrapping orientations are little known or not available in the open literature. However, several experimental and simulation studies related to academic research are reported in the open literature related to the design and testing of Type IV COPVs based on their capacity, operating parameters, and selection of materials. For the design calculations, the netting analysis (NA) and classical laminate theory (CLT) are used for finding the overall thickness and stresses in the composite wrapping for given operating conditions, respectively [12, 13]. CFRP with unidirectional (UD) fibers has unique strength properties that meet the requirement

of high p_{nwp} of these COPVs. To validate the p_{nwp} of COPVs, they are tested using a hydraulic medium in a controlled environment up to the burst pressure (p_b) , defined as the maximum pressure required for initiating a failure in PVs. For enhanced safety, p_b is set at $2.25 \times p_{nwp}$ or more as per various national and international standards (ISO 19881) for COPVs.

Finite element (FE) simulations are commonly used to optimize COPVs design that involves optimizing the boss design, winding sequence, liner-boss interface design as well as the failure behavior using selective failure criterion at the p_b [14, 15]. An improper boss design and liner-boss interface cause leakage and failure of the costly Type IV COPVs. For storing 5.6 kg of usable H_2 at 70 MPa, the cost comparison of baseline components of Type IV COPVs, which includes carbon fiber, resin matrix, selling, general and administrative (SG&A), scrap, manufacturing, boss, and liner (without boss) is shown in Fig. 1.2. As shown, 76% of the total cost of Type IV COPV is contributed by carbon fiber used as reinforcement of plastic matrix in CFRP based overwrapping.

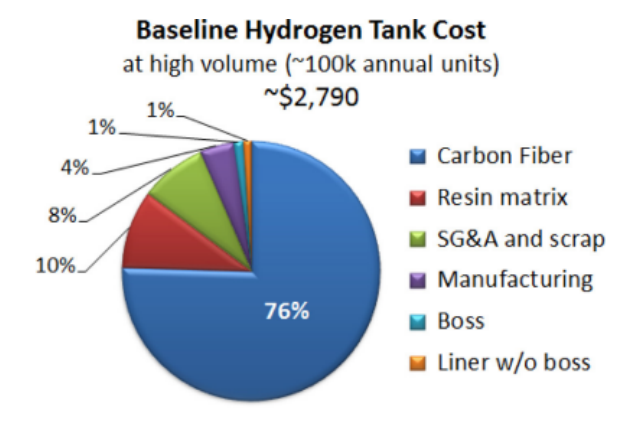


Figure 1.2: An illustration of a typical Type IV hydrogen COPV with a wall showing the polymer liner core wrapped with fiber-reinforced composite [1].

The polymeric liner of Type IV COPV protects the metallic boss and the composite material from direct physical contact with H₂ to avoid HE and leakage. However, due to the small size of H₂ molecule, it can permeate through most materials, including polymeric liners. Several studies have focused on the H₂ permeability in polymers under low-pressure conditions, and little is discussed in the open literature about the behavior of these materials under high-pressure H₂. It is reported that the H₂ permeation properties of semi-crystalline polymer material (permeability, diffusivity, and solubility) are functions of the operating pressure of H₂ gas [16, 17, 18]. Excessive H₂ permeation in polymeric liners can cause various kinds of failures in Type IV COPV, such as liner buckling, blistering at the interface of composite winding and liner, and cavitation in the liner (as shown in Fig. 1.3 [19]) that are generally promoted by various manufacturing defects observed in the liner, such as the inclusion of air, foreign particles, and others [20, 21, 22]. This results in liner collapse and failure of Type IV COPVs during the operational cycles (filling-defilling) [2].

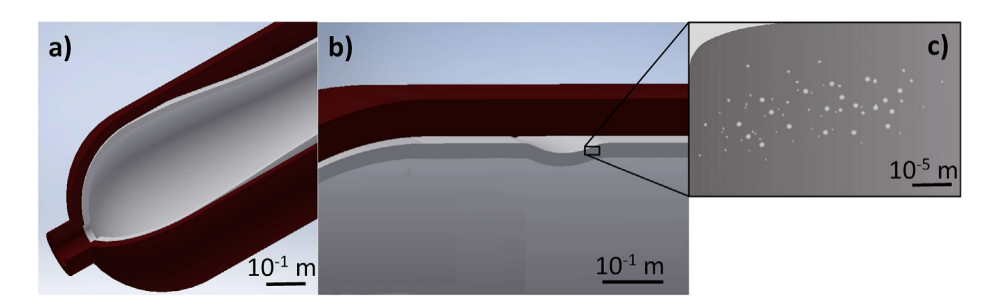


Figure 1.3: Schematic of Type IV COPV under (a) buckling, (b) blistering, (c) cavitation (scale mark is approximate) [2].

The failure of this costly H₂ storage system causes a huge economic loss along with increasing the risk of causing catastrophic failure. These factors make Type IV COPV an active area of research to further improve their performance w.r.t storage capacity, cost reduction, safety, and applications while taking practical issues like manufacturing defects into consideration.

1.2 Background and Motivation

Development of Type IV COPVs involves multiple materials, components, and manufacturing processes as mentioned above. Since the beginning of the PhD, author was involved in development of a Type IV COPV with p_{nwp} of 70 MPa as part of a sponsored project¹ where the role of author was to design and fabricate the components of COPV such as bosses, design of Filament Winding (FW) on a prefabricated liner-boss assembly along with providing support in the fabrication and testing of the designed COPV. A brief description of the design, manufacturing and testing process adopted for a custom-made Type IV COPV is mentioned below:

1.2.1 Experimental work on design, fabrication, and testing of Type IV COPV

An 18 L internal water volume capacity Type IV COPV with p_{nwp} of 70 MPa is chosen for design, fabrication, and testing work. Considering the non-availability of in-house manufacturing facilties like rotomolding and FW machinery, a pre-fabricated roto-molded polymer liner made of HDPE material (as per the design offered) was procured from an international vendor (Crompton Mouldings, U.K). A custom-designed metallic boss was then fabricated at IIT Ropar. A schematic of metallic boss and polymeric liner is shown in Fig. 1.4 (a detailed description is shown in Fig. 3.5). Metallic bosses were pasted over liner using structural adhesive (3M DP460) after treatment of the contact surface on boss to generate roughness using emery paper. The procured polymer liner and fabricated liner-boss assembly are shown in the Fig. 1.5.

¹Project No. 5815; Title: Design, development, and demonstration of Indigenous hydrogen storage and fuel cell system for mobile and stationary applications of 5 kW capacity

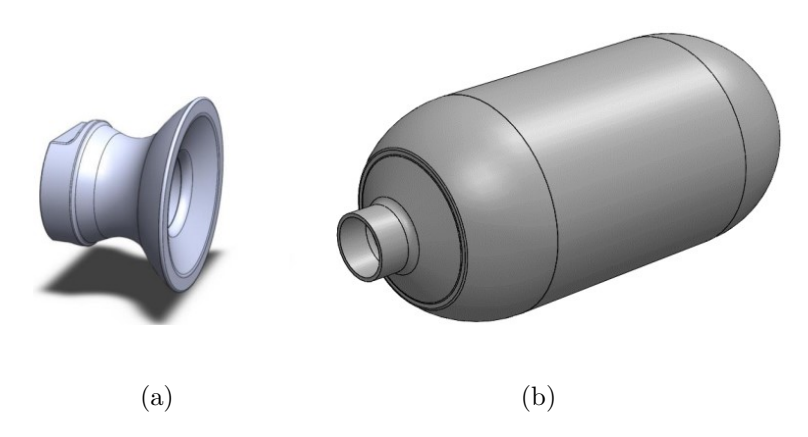


Figure 1.4: A schematic of (a) metallic boss, and (b) polymeric liner.



Figure 1.5: (a) Polymer liner procured from Crompton Mouldings, U.K., and (b) liner-boss assembly fabricated at IIT Ropar.

On the liner-boss assembly, wet FW was performed at CNC Technics Pvt. Ltd, Hyderabad, India as per the optimized winding sequence provided to CNC Technics by the author. Optimization of winding sequence was obtained through finite element analysis (FEA) performed using WCM plugin in ABAQUS simulation software. The liner-boss

assembly undergoing FW process at CNC Technics is shown in Fig. 1.6.



Figure 1.6: Winding of CFRP on the liner-boss assembly during FW process.

Following steps were followed during the FW process at CNC Technics:

- 1. Fiber Type: The carbon fibers T700S-12K-50C from Toray were considered for FW. The bobbins of carbon fiber were placed on the creel system.
- 2. Resin Preparation: A 2:1 blend of epoxy (LY556) and hardener (XY54) was utilized as the resin (matrix) material for fiber impregnation towards wet winding.
- 3. Mandrel Mounting: The liner-boss assembly was mounted on the 4-axis FW machine, supported by the chucks. It ensured that the liner-boss assembly was securely held during the winding process, allowing for precise control during the fiber placement.
- 4. Band Width: A single spool of fiber was used for winding with a bandwidth of 2 mm at the pay-out eye mounted on the carriage that moves along the axis of the rotating mandrel.
- 5. Winding: Fibers were wound on the mandrel surface (according to the optimized winding pattern obtained from from FEA), completing the manufacturing of Type IV COPV.

After the completion of composite wrapping, the Type IV COPV was subjected to curing in an oven for 1 hour at 100 °C as shown in Fig. 1.7. The fabricated Type IV COPV was tested for identifying the burst pressure while hydraulically pressurizing up to 157.5 MPa at GEM Pressure Systems Pvt Ltd., Hyderabad, India. The site of p_b test and remote monitoring arrangement during testing is shown in Fig. 1.8. During the test, a leakage of water was observed from the dome region at the pressure values of 10 MPa only confirming the leakage of water from open end boss-liner interface. Due to financial constraints, only

one Type IV COPV was developed and tested. However, the observed failure of tested COPV provided several insights into the role of boss design, manufacturing, winding defects, and interfaces in Type IV COPV. This failure actually formed the basis for setting the objectives and scope of this thesis work as mentioned in following sections.



Figure 1.7: Curing of fabricated composite cylinder after wrapping to cure the epoxy resin.

1.3 Objectives and Scope

This thesis aims to address the critical challenges in design and development of a Type IV COPV with p_{nwp} of 70 MPa, focusing on possible defects in such vessels that may lead to early failure. As explained in the introduction and shown in the background work, several parameters are crucial for the development of failure resistant Type IV COPVs. Besides mechanical failure at burst pressure, polymeric liner material failure due to H_2 permeation has been reported during their operational cycles. The improper selection of material, liner thickness, and defects during manufacturing can lead to costly failure of these storage systems. A computational framework that considers manufacturing defects and correctly accounts for H_2 permeation in the liner material can significantly improve our understanding of complex phenomena happening in Type IV COPVs during their operational life. Thus, based on computational studies, this work aims at improving the cycle life, cost, and safety aspects of Type IV COPVs by developing a modeling framework that accounts for the manufacturing defects and H_2 permeation in liner material to simulate the failure behavior of Type IV COPVs.

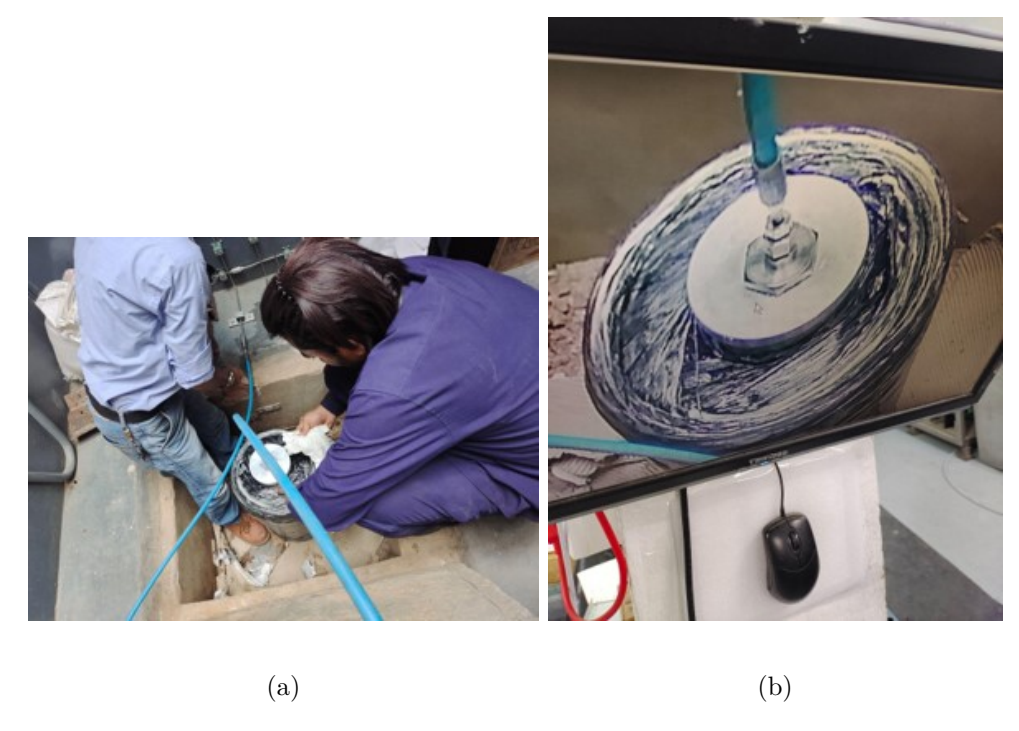


Figure 1.8: (a) Picture of site preparation for burst test and (b) remote monitoring of cylinder during burst test.

The defined objectives of this thesis work are summarized as follows:

- 1. Development of a computational framework that accounts for manufacturing defects to investigate the mechanical failure at p_b .
- 2. Development of a novel material modeling framework of H₂ permeation through the liner material that accounts for polymer morphology, density, and thickness to achieve the desired permeation limit in Type IV COPVs.
- 3. To analyze the role of H₂ permeation on manufacturing defect-based failure in liner and liner-composite interface under filling-defilling cycles of Type IV COPVs.

1.4 Outline of the thesis

The research objectives of the present work are structured and elaborated in five chapters, as outlined below:

In **Chapter 1**, a general introduction, background, objectives and scope, and layout of the thesis is provided. The challenges associated with the onboard gaseous H_2 storage are explained along with the motivation for this thesis.

In **Chapter 2**, the design and material aspects related to the failure of Type IV COPVs for high-pressure applications are summarized. The chapter also describes failures associated with H_2 permeation phenomena and pre-existing defects relevant to Type IV COPVs during operation.

Chapter 3 focuses on Objective 1, where a computational investigations were performed

to simulate possible scenarios of manufacturing defects in Type IV COPV and their effect on the failure behavior at p_b .

Chapter 4 focuses on the development of the H₂ permeation model in a commercial FE software, ABAQUS. The modeling framework considers the gradients of concentration and pressure-driven mass diffusion at a constant temperature. Variations in the diffusion coefficient are implemented in the model based on operational parameters and the structural properties of the liner material. The modeling framework incorporates H₂ permeability reduction in liner material with increasing H₂ pressure.

Chapter 5 extends objective 2 towards safety concerns involving Type IV COPV that are crucial due to the occurrence of decompression damage, influenced by the H₂ transport properties in liner material and H₂ gas operating parameters. The influence of pre-existing micro-defects present inside the polymeric liner and at the interface of polymer-composite on H₂ permeation through the wall of Type IV COPV is investigated for a given H₂ filling and defilling cycle using FE simulation. This comparative study provided a valuable understanding of the role of defect size and location to avoid catastrophic failures during the operational cycle of Type IV COPVs for onboard H₂ storage applications.

Chapter 6 Summarizes the findings in this thesis and discusses the future scope of the work.

Chapter 2

Literature Review on Failure Study of High Pressure Type IV COPVs

2.1 Introduction

High pressure Type IV COPVs, primarily used for storing and transporting gases such as H₂ and hydrogen-blended compressed natural gas (HCNG) in various applications, face several technical challenges. The studies, along with recent work on the design, manufacturing defects, and H₂ permeation-based failure analysis of Type IV COPVs, are summarized in the following sections.

2.2 Design and Failure Study of Type IV COPVs

Type IV COPVs use a polymeric liner and boss assembly, over which composite layers are wrapped by filament winding (FW). The inner carbon fiber (CF) layer, which is thicker, provides the strength needed to resist the stored H₂ gas pressure of Type IV COPVs, while the thinner outer glass fiber (GF) layer protects it from damage caused by drops or impacts [23, 24, 25]. The blow-moulded polymeric liners (BMPLs), glued to the metallic boss, caused failure during cyclic pressure tests. The failure occurred due to a crack oriented perpendicular to the liner's parison pinch-off seam in the hemispherical dome region. This crack originated from the parting line of the mold and was further exacerbated by a gap in the glued region [26].

Recently, the topology optimization of boss has been reported to ensure safety and sealing behavior [27]. The boss design and the liner interface have been analyzed to enhance the performance with the connection of CFRP [28]. The heat-treated aluminium alloys (e.g., Al6061-T6, Al6082-T6, 7075-T6) are anodized via methods like sulphuric acid anodizing or plasma electrolytic oxidation to form oxide layers, which electrically isolate the two electrically conductive materials having dissimilar electrochemical potential [29, 30]. This barrier disrupts the electrochemical pathway or contact between the aluminium alloy (anode) and CFRP (cathode), preventing contact-based galvanic corrosion (GC) in the presence of electrolytes like water present in atmospheric air [31]. Without such protection, aluminium undergoes oxidation, forming porous aluminium hydroxide and leading to gradual mass loss and interface failure [32, 33]. During H₂ cycling tests of Type IV COPVs, grounding the metallic end boss (which supports the filling/defueling valve)

can mitigate triboelectric charging that originates from frictional interactions between high-velocity H₂ and the polymer liner, generating significant surface potentials. The resultant electrostatic discharge (ESD) poses an ignition risk due to H₂'s wide flammability range (4–75% volume in air) [34]. Grounding the end boss provides a conductive pathway to neutralize accumulated charges, prevent sparking, reduce ESD-induced damage, and minimize risks of fatigue cracking and deterioration, as recommended by ISO 19881 and the safety of H₂ storage technologies [35]. The study has reported on torque enhancement of liner-boss with CFRP coupling, considering SUS31603 and AA6061-T6 as boss materials. S31603 boss material has been recommended for better performance in fatigue loading [36].

Among CF, GF, and kevlar fiber (KF) reinforced plastic composite materials, it has been predicted using FEA that KFRP has been evaluated for critical buckling load for larger applications [37]. The weight reduction and performance enhancement were achieved using larger sizes of CF among T700S, T800S, and T1100G with an increase of V_f by 60%. Furthermore, the stress concentration at the dome-cylindrical interface was reduced to an p_{nwp} of 70 MPa, with a p_b value of 157.5 MPa. The measured critical stresses were 2574 MPa, 3126 MPa and 3391 MPa, which are safer compared to the tensile strength of 2860 MPa, 3290 MPa, and 3460 MPa, respectively [38]. Advanced fiber placement (AFP) reinforces high-stress zones (e.g., dome-cylinder interfaces) in high-pressure Type IV COPVs, enhancing structural integrity while minimising CF usage. Towpreg/prepreg winding—using epoxy-impregnated fibers enables rapid, low-void fabrication, outperforming wet winding in cycle times and consistency. T700, M40, IM7, T800, and T800S CFs achieve tensile strengths up to 4950 MPa and moduli of 275 GPa (IM7), balancing stiffness and elongation (1.4–2.0%) [39]. AFP excels in precision thermoset layups, while towpreg's cost-performance efficiency makes it ideal for H₂ storage COPVs and aerospace structures. This improvement is attributed to these materials' higher tensile strength, modulus, and lower yield strain [40].

Composite failure is categorized based on the various mechanisms like delamination, matrix and fiber cracking [41], etc. In Table 2.1, the experimental (Exp.), analytical, and FEA studies are summarized based on the design and failure criteria of Type IV COPV. Non-destructive testing (NDT) employs independent failure criteria associated with various failure modes, including Tsai-Wu, Tsai-Hill, Azzi-Tsai, Hoffman, and Chamis [42]. The Puck failure criterion analyzes inter-fiber failures by categorizing matrix cracking into stress-dependent modes and distinguishes them from fiber failures [43, 44]. While enabling precise failure prediction, its implementation in FEA requires complex user-defined subroutines, extensive material testing for parameter calibration, and struggles with modeling progressive damage degradation [45, 46, 47].

Table 2.1: Various design parameters and failure criterion used for Type IV COPVs.

Test	Material &	Design & analysis	Method and
parameters	component	parameters	software
p_{nwp} 70 MPa	Nylon 6, CFRP	WA, thickness, Max.	ANSYS [48]
1 1000	,	principal, and Eq. stress	
p_{nwp} 70 MPa	CFRP	CLT thick wall model,	ABAQUS,
Filmp 1 o and a		Stress component	Analytical [49]
$p_b 8.0 \text{ MPa}$	Nylon, ABS,	Load cycle, deformation	Exp. [50]
<i>p</i> ₀ 0.0 MH a	GFRP, AL	Load cycle, deformation	Exp. [60]
p_b 47 MPa	HDPE, GFRP,	Tsai-Wu, Tsai-Hill, Max.	ABAQUS
p_b 41 MH a	Boss	stress, stacking sequence	WoundSim &
	Doss	stress, stacking sequence	Exp. [51]
$p_b 60.5 \text{ MPa}$	HDPE, CFRP	Stress, stacking sequence	ABAQUS WCM &
p_b 00.5 M1 a	IIDI E, OFILI	Stress, stacking sequence	•
150 MDa	HDDE CEDD	Strong along than	Exp. [52]
p_b 158 MPa,	HDPE, CFRP, Boss	Stress along fiber	ABAQUS [53]
2.25		direction, doilies layer	A D A OLIC
p_{nwp} 52 MPa,	PA6, CFRP,	Max. principal stress,	ABAQUS
2.25	Boss	predefined crack effect	WCM2017 & Exp.
00 T MD	IIDDE 11 1	TD : 117	[54]
$p_{nwp} \ 20.7 \ \text{MPa},$	HDPE blend,	Tsai-Wu, von Mises stress	Abaqus6.8, WCM
2.0	CFRP, AA		[55]
p_{nwp} 166.95	PA6, 316L,	Progressive failure, strain	Exp., ANSYS [56]
MPa, 2.25	CFRP	critera	
p_{nwp} 70 MPa	HDPE, CFRP,	Failure strain	Abaqus WCM[57]
	Boss		
$p_b \ 166.11 \ \mathrm{MPa}$	PA6, CFRP,	Cylinder-dome interface	Exp., Analytical
	AA Boss	failure	[58]
p_{nwp} 70 MPa	PE, CFRP,	Dome thickness	FEM [59]
	Boss	prediction, Tsai-Wu	
		failure	
$p_b 113.4 \text{ MPa}$	HDPE, CFRP	Transverse shear stress,	Abaqus, Analytical
		interface failure	[60]
p_b 185 MPa	PA6, CFRP,	Tsai-Wu failure criteria	Abaqus, WCM [46]
	Boss		
p_{nwp} 70 MPa,	HDPE, CFRP	Tsai-Wu failure criteria	Analytical,
2.25			ANSYS14.0 [61]
$p_b \ 166.19 \ {\rm MPa}$	PA6, AA,	Displacement 6 mm	ABAQUS2017 [62]
	CFRP	without damage	
Thermo-mech.	PU, CFRP,	Temperature affects p_b	Abaqus, WCM [41]
load, p_{nwp} 70	316L		
MPa			
p_{nwp} 70 MPa	HDPE, CFRP,	Equivalent stress	MATLAB, Abaqus
			[63]
p_b 40 MPa	HDPE, CFRP	Tsai-Hill, von Mises stress	MATLAB [64]
$p_b \ 26.76 \ {\rm MPa}$	HDPE, CFRP	Max. stress, Max. strain	Abaqus, WCM,
		·	Exp.[65]
p_{nwp} 20 MPa	Graphite/epoxy	Hoop, axial, von Mises	ANSYS [66]
		stress, Tsai-Hill	
L	l .	· · · · · · · · · · · · · · · · · · ·	

Tsai-Wu criterion is widely acknowledged for its precision in predicting failure pressure in composite materials. Although this criterion is inherently conservative, it plays a crucial role in ensuring safety throughout the design process [67]. The stress and Tsai-Hill failure indices were analyzed for a symmetrical cross-ply graphite/epoxy composite cylinder, focusing only on the first two layers. The Tsai-Hill failure index values for the second layer are 2.07 when the ends of the domes are fixed and 1.84 when they are free as a boundary condition [66]. A 2-D axisymmetric model with a total composite thickness of 32.54 has been analyzed for p_b of 117 MPa [54]. The 1/36 part of Type IV COPV without boss has been analyzed using FEA and burst at 60.5 MPa near the head, and the error is 9.6% with the Exp. test [52]. A blend of 95 wt.% LLDPE and 5 wt.% HDPE material rotomolded liner with a prototype of 1 litre and actual liner of internal water capacity 22 litres has been tested for p_b . The theoretical and Exp. thickness of the polymeric liner is estimated to be in the range of 15–16 mm and to withstand a maximum pressure of 2.0–2.2 MPa. CFRP wrapped over the liner and tested using FEA for 20.7 MPa with a safety factor of 2.0, and it has been reported that the Tsai-Wu failure index value was critical for the second layer [55]. Utilizing ANSYS composite pre/post (ACP), the prepreg winding configuration (angle, orientation, arrangement, and number of layers) has been analyzed for stress analysis. The ultimate strength of the composite is 1979 MPa, corresponding to applied p_{nwp} 70 MPa; for hoop layers, the maximum principal stress generated is 1874.2 MPa, which results in p_b 73.91 MPa. The low helical angle provides a durable result compared to other helical angles. The boss geometry is missing through the analysis [48]. The closed-form analytical model was used to analyze the cylindrical part of Type IV COPV. The symmetric and asymmetric models were analysed and validated using the FEA tool [49]. A Type IV COPV with 3-D printed polyamide and acrylonitrile butadiene styrene (ABS) liner with GFRP wrapped and tested for 8.0 MPa [50]. A rotomolded polymeric liner with end bosses was wrapped with GFRP and tested for 47 MPa for various stacking sequences utilizing WoundSim ABAQUS [51]. The CFRP with 2.0 mm thickness of LLDPE, LLDPE/HDPE, and HDPE liner material has sustained the pressure of 20, 30, and 40 MPa for the yield stress of 10, 15, and 25 MPa, respectively [64].

Research and development efforts for Type IV COPVs continue to address diverse application requirements – such as H₂ storage, aerospace, and automotive – across varying geometric configurations (water capacity, diameter, and length). Each configuration demands unique design and manufacturing parameters, even for dimensional adjustments (e.g., length or diameter) at a fixed water capacity, necessitating validation of process parameters and design integrity. Modifications to fiber specifications (e.g., CF, KF, or GF), fiber precursors, fiber manufacturers, structural materials, or cylinder designs require full type approval testing. While minor variations may qualify for reduced testing as per ISO 11119-3. To minimize reliance on physical trials, simulation-driven optimization-such as FEA for stress distribution and progressive damage modeling, is critical for achieving scalable, high-performance Type IV COPV development.

2.3 Hydrogen Permeation-Induced Failure Study of Type IV COPVs

H₂ permeation through the polymeric liner material is a critical challenge of high-pressure Type IV COPVs. High-pressure high-permeation (HPHP), thermal decomposition analysis (TDA), and FE-based methods are most common in analysing the H₂ permeation behavior through the polymeric liners. BMPLs with a length of 720 mm, a diameter of 365 mm, and a uniform thickness of 3.5 mm were analyzed for H₂ permeation using RC's BlowView software. The analysis found a pressure-independent permeation rate of 17.2 Nml/hr/l (normalized liters of H_2 per hour per litre of tank volume), while the pressure-dependent analysis showed a maximum reduction to 3.5 Nml/hr/l [68]. These values should be compared to the regulated maximum allowable limit at 20 °C, which is 8.0 Nml/hr/l [69]. According to ISO 11119-3, the allowable H₂ permeation rate for Type IV COPVs with polymeric liners is ≤ 2 ml/hr per liter of water capacity, which is notably higher than the ≤ 0.25 ml/hr/l limit specified for air, nitrogen, or CNG. The permeation through the semicrystalline polymers is a complex phenomenon due to its little-known behavior under high-pressure conditions. The diffusion occurs exclusively in the amorphous regions of the polymer, with crystalline regions acting as effective barriers; thus, highly crystalline HDPE liners are more effective at reducing H₂ permeation. However, while increased crystallinity decreases H₂ permeation, it can also negatively impact the liner's mechanical properties, such as elongation [70].

Nylon exhibits good mechanical properties and H₂ barrier performance, but absorbs water due to the carbonyl oxygen in its amide groups. Moisture absorption is typically measured to qualify liner materials selection according to ISO 62 [71]. The absorbed moisture acts as a plasticizer, causing the plastic to swell and resulting in decreased strength and stiffness [72]. As more water accumulates, the free volume within the polymer matrix increases, and the intermolecular bonds are weakened, which reduces the H₂ barrier properties and causes dimensional changes [73, 74]. To address this, surface modification techniques such as direct fluorination have been applied to polymer materials. These methods have been shown to significantly reduce water uptake, thereby improving the long-term performance of Type IV COPV liners [75, 76, 77]. At low temperatures (-40 °C and 0 °C), brittle fracture occurs in both neat PA6 and PA6/organo-modified montmorillonite nanocomposite liner materials [78].

Explosive decompression failure (XDF) is a common failure mechanism in liner materials during cyclic pressure testing under conditions ranging from 2 MPa to $1.25 \times p_{nwp}$ [79]. The pressure relief time critically influences the H₂ permeability and structural integrity of PA6 and PA11 liners in Type IV COPVs. At 6-second decompression, H₂ permeability decreased due to microstructural damage (tiny holes in PA6 and clustered holes in PA11), while 60-second and 3600-second cycles caused < 2% permeability change but introduced

cracks. Tensile strength remained stable, but nominal strain surged by 100% (PA6) and 53% (PA11) under rapid decompression, indicating strain-rate sensitivity. Optimal pressure relief times (60–3600 s) balance permeability control and structural stability, which are crucial for designing durable H₂ storage systems [80]. In recent years, extensive Exp. and numerical studies have investigated H₂ permeation through polymeric liners and polymer blends, highlighting its critical role in the failure mechanisms of Type IV COPVs under cyclic decompression loading. The literature on H₂ permeation and its contribution to liner and Type IV COPV material failures, such as delamination of liner-composite, blister formation, XDF and cavity formation, is summarised in Table 2.2.

In summary, ongoing research is addressing critical challenges in the design, manufacturing and permeation-based failure study of Type IV COPVs for high-pressure H₂ storage through numerical modeling, and design optimization.

Table 2.2: Hydrogen permeation-induced failure study of Type IV COPVs material.

Liner	Operating parameters	Test, Failure parameters	Method, Software
HDPE	70 MPa, 27°C, 55°C, 72	Collapse, buckling,	Exp. and FE [81]
	hrs.	Liner-Composite Interface	
PE grades	90 MPa, 30°C, 24 hrs	Permeation wrt pressure	HPHP and TDA [18]
		and crystallinity	
HDPE, PA	87.5 MPa, 25°C, 13 hrs	Depressurization-induced	COMSOL [20]
		blistering	
HDPE,	86 MPa, -30 to 85°C,	Permeability vs pressure	Exp. HPT [82]
PET, PA6	16.38 hrs	for various Young's	
		modulus	
EPDM	27 MPa, 25°C, 13 hrs	XDF with volume fraction	FE Abaqus [83]
		of cavity	
HDPE, PA,	87.5-0.1 MPa, 50-25°C,	XDF cause cavitation,	Numerical [21]
EPDM	13 hrs	depressurization	
HDPE	0.71 MPa, 25°C, 5.83 hrs	Permeation and Fracture	COMSOL, Exp. [84]
Elastomer	9 MPa, 25°C, 13 minutes	Decompressed at different	Exp. [85]
		rates, pressure	
HDPE,	10.3 MPa, 25°C, 1	Permeability and	Numerical [86]
LDPE	seconds	diffusivity wrt pressure	
HDPE	100 MPa, -40 to 85°C, 7	Permeability and strength	Exp. [87]
	days	wrt pressure	
HDPE	90 MPa, 30°C, 24 hrs	HTM properties	Exp. [88]
EPDM	10 MPa, 30°C, 24 hrs	Failure in polymer	Exp. [89]
CFRP	196 MPa, 23°C	Permeability, damage,	Exp. [90]
		orientation	
EPDM	5.75 MPa, 25°C, 13.9 hrs	Concentration	Exp. [91]
PE100,	2-0.5 MPa, 20-50°, 450	Permeability vs time,	Exp. [92]
PA11	days	temperature	
HDPE	2 MPa, 20-50°C, 4 hrs	Permeability, diffusivity	Exp. [93]
		formulation	
PA6, PA12	35 MPa, 65°C, 7 days	CTE difference,	Abaqus [2]
		delamination	
BMPL	70 MPa, 20°C, 48 hrs	Effect of pressure on	NRC's BlowView [68]
HDPE		permeability	
PA6, PA11	70-1 MPa, 15°C, 7 days	Effect on decompression on	Exp. [80]
		permeability & strength	

Chapter 3

Role of Manufacturing Defects on Failure Behavior of 70 MPa Type IV COPV for H₂ Storage

3.1 Introduction

To achieve sustainability with respect to world's energy requirement in future, it is important to develop storage systems for H₂ that can store H₂ without any loss. This is particularly difficult due to the small size of H₂ gas molecules, that can lead to easy diffusion or leakage of H₂ in any gaseous storage system. In addition, gaseous H₂ need to be stored at high pressure to provide sufficient quantity of H₂ required for meeting the operational requirements. Such high pressure storage of H₂, can lead to the premature failure of a pressure vessels (PVs) made completely of metals, called Type I PVs, due to hydrogen embrittlement phenomenon [94, 95, 96, 97, 98]. Looking at such limitations, several new technologies are being explored for large-scale H₂ storage. These include Type II PVs that has a metallic vessel wrapped with fiber reinforced plastic (FRP) based composite over cylindrical part, Type III composite overwrapped PVs (COPVs) that has metallic liner (vessel) wrapped with FRP composite over both dome and cylindrical part, Type IV COPVs that has plastic liner wrapped with FRP composite over both dome and cylindrical part, cryo, cryo-compressed and materials-based storage, among other alternatives [99, 100].

Among various options available, Type IV COPV is one of the prime option available for H_2 storage so as to provide a competitive driving range for fuel cell electric vehicles (FCEVs). A major design requirement for Type IV COPVs is the necessary demonstration of a burst pressure, p_b , that is more than 2.0 times their nominal working pressure, p_{nwp} , as per the international standards for refillable composite gas cylinders [101]. One of the main advantages of these COPVs is that they allow FCEVs to be quickly refueled while providing driving range comparable to IC engine based vehicles [102]. However, they are costlier due to the high usage of carbon fiber (CF) material, which contributes to 70% of their cost. Additionally, because of its plastic liner, it has low toughness, low damage tolerance, and is vulnerable to impact loads. The p_b test is one of the top-rated tests other than free-fall drop impact, bullet penetration, extreme temperature pressure cycling, bonfire test, etc. to qualify the Type IV COPV as per international standards.

Unlike metallic PVs (Type I, II, III), Type IV COPVs exhibit significant performance variations with slight changes in geometry, material composition, and design parameters. Several experiment and simulation based studies are available in the literature that discuss the design process and assess the performance of mechanical behavior of complex multi-material structures of Type IV COPVs [65, 103, 53, 56, 104, 105, 106]. Many of these studies focus on the design of individual parts such as polymer liner [55], dome shape [107, 59, 60], CF stacking sequence [47, 108], etc. for their performance evaluation. The manufacturing methods used for polymeric liner development affects the performance of Type IV COPVs. Typically, highly efficient high-pressure Type IV COPV is produced using filament winding (FW), and it can be very difficult to maintain accuracy due to several manufacturing design variables, including volume fraction (V_f) , winding angle (WA), stacking sequence, bandwidth [109], cut-uncut helical layers [110], ply-drop location [47], and the requirement of an ideal relationship between FW tension [111] and winding time. The fiber bandwidth (BW) is related to the number of tangent points, which directly affects the cylinder-dome interface and fiber placement near the polar boss region. It is known that a decrease in BW increases the layer thickness of the dome region [112]. An increase in the number of tangent points reduces fiber overlap and enables smooth thickness distribution along the circumferential direction [113]. The V_f , WA, and strength properties are random parameters directly related to the manufacturing uncertainties of composite layup [114]. The conventional netting analysis (NA) for the design and manufacturing of the dome-cylinder interface shows a jump due to a sharp geometry change. This causes the failure at the dome-cylinder interface due to secondary stresses and differences in stiffness [60, 115, 116]. These COPVs are designed based on safe and unsafe burst modes. In the case of safe burst mode, the failure occurs along the axis of the center of the cylindrical part in the circumferential direction, resulting in the boss going inward of Type IV COPV [15]. In case of unsafe mode, failure occurs in the dome region, which could lead to the ejection of the boss due to the liner-boss junction and dome-cylinder interface failure [56, 106, 15, 117, 118]. The dome-cylinder interface failure is found to be due to thickness transition which can be prevented by the use of doily layers (strips of CF as shown in black color in Fig. 3.1) placed to ensure the safety of COPVs [53, 119, 120, 121, 122, 123]. A few failure behaviors of Type IV COPVs are also studied concerning various factors that control their burst strength [56, 124], and failures such as liner collapse during decompression [2].

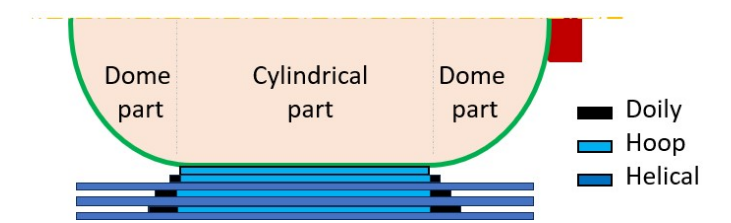


Figure 3.1: A schematic of doily layer inserted with hoop and helical layers on liner-boss assembly.

In finite element analysis (FEA), a half or full axisymmetric model was generally considered for the symmetric polymeric mandrel, and a symmetric load case was considered [46, 125, 126]. The failure criterion was employed to ensure the strength of a safe COPV design, although the majority of the literature only took the stress, strain, and deformation-based criterion into account for its design and analysis. The static burst pressure and thermo-mechanical loading were considered and analyzed by ABAQUS tools and experimentally tested. In the analysis, a gap was reported at the polymeric liner-boss junction and the boss-composite interface, but we didn't consider as a serious issue and part of the research [15, 46, 63, 127, 128].

The air gap was detected by reverberation NDT at the aluminium-polymer liner interface. Interfacial strength is reported in very few works of literature for metallic liner-composite interactions [129] and thermoplastic PA6 liner and composite material [46, 130]. Manufacturing defects arise in a composite layup during the FW process on the liner-boss assembly due to the shape or improper design of the liner-boss assembly. It could be caused by the filament slipping while being wound, the hoop winding being placed incorrectly at the end of the cylindrical section, the air gap between the liner-boss connection, and other factors [47]. The uniformity and defect detection on the LDPE and HDPE polymer liner samples were detected by ultrasonic NDT, which contains an artificial defect [131]. Application of putty, a patch, filler, or sleeve material is used to repair a damaged area of gas pipelines for metal or polymer pipelines and also for COPVs [132, 133].

Despite such vast studies available in the literature, the role of design and manufacturing defects on failure behavior of Type IV COPVs is not clearly understood. To ensure safety and further improvement in the upper pressure limits of H_2 storage, it is important to understand the role of design parameters and manufacturing defects on their failure behavior at p_b . In this paper, few critical design and manufacturing defects such as shape of composite winding, metallic boss and possible gap at the liner-metallic boss-composite winding interface are considered in an 18 litre Type IV COPV to analyse their individual role in failure. Such defects are found to be hot spots for failure of Type IV COPVs which is characterized in terms of Tsai-Wu failure criterion for composite winding. These findings are then corroborated with the experimental failure observed in a similar Type IV COPV to provide guidelines for developing a failure resistant Type IV COPV.

This chapter is organized as shown in Fig. 3.2 and follows: after providing a brief introduction to the topic and relevance of this work, the following section provides the analytical relationships related to NA, CLT, and failure criteria that form the basis of designing the proposed Type IV COPVs. The list of material properties, dimensions of various parts, and FE modelling details are then provided in the next section. The results section provides the distribution of equivalent von Mises stress and Tsai-Wu failure

index (F.I) based investigations in the composite winding, followed by discussion and conclusions.

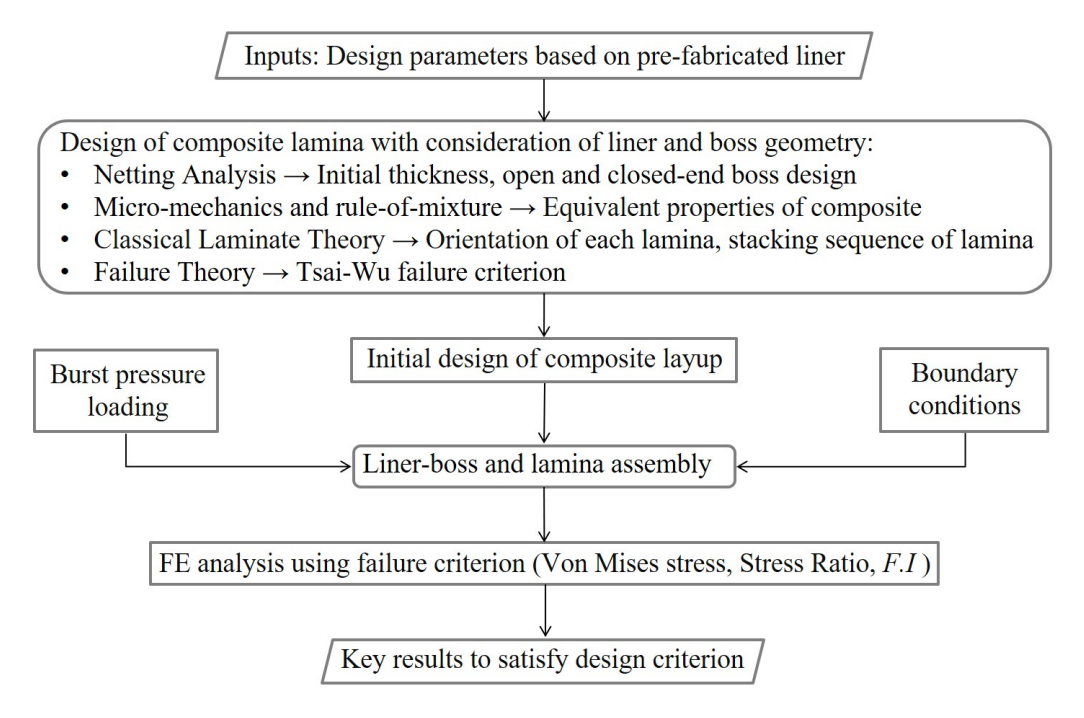


Figure 3.2: A schematic flow diagram for design and analysis of Type IV COPV.

3.2 Mathematical Formulation Used for Design of Type IV COPVs

In this section, the analytical relations used for the design of Type IV COPV based on NA and CLT are discussed first. Based on these relationships, the design parameters of COPV are selected for FE modeling.

3.2.1 Prediction of composite thickness based on netting analysis

FW is a widely used technique for manufacturing axisymmetric composite PVs using continuous unidirectional (UD) fibers. The inner liner geometry acts as the base geometry and serves as a mandrel for the FW process. The NA is a preliminary sizing step to estimate the thickness of the helical and hoop layers for a given p_b and ultimate fiber strength. A few assumptions are adopted when performing NA, as mentioned below [107, 13]:

- 1. There are negligible or low shear stresses at the interface between matrix and fiber, and the matrix does not contribute to carrying any part of the load in tension.
- 2. The fiber and the matrix have equal strain during tensile and compressive loading.
- 3. Load sharing contribution from the polymeric liner is considered to be non-existent.

- 4. COPV is designed for p_b using the ultimate strength of the fiber.
- 5. All the materials used in the structure obey Hooke's law.
- 6. The fibers are straight and continuous.

The schematic of a COPV section with inner radius R_c subjected to internal pressure p and helical layers wound at an angle α is shown in Fig. 3.3(a). The stresses in the hoop and helical layers are σ_{90} , and σ_{α} respectively. The dome part is only wounded by helical layers as shown in the schematic Fig. 3.3(b), where R_b is the outer boss radius, F_a is the axial force that varies with radial distance r of the dome region from the axis of rotation along y-direction and F_c is the circumferential force in the cylindrical part. Due to only helical winding, the fiber strength in the dome part is unable to achieve a level similar to that in the cylindrical part. This is compensated by an increase in the thickness of the helical layer with a decreasing radius in the dome part.

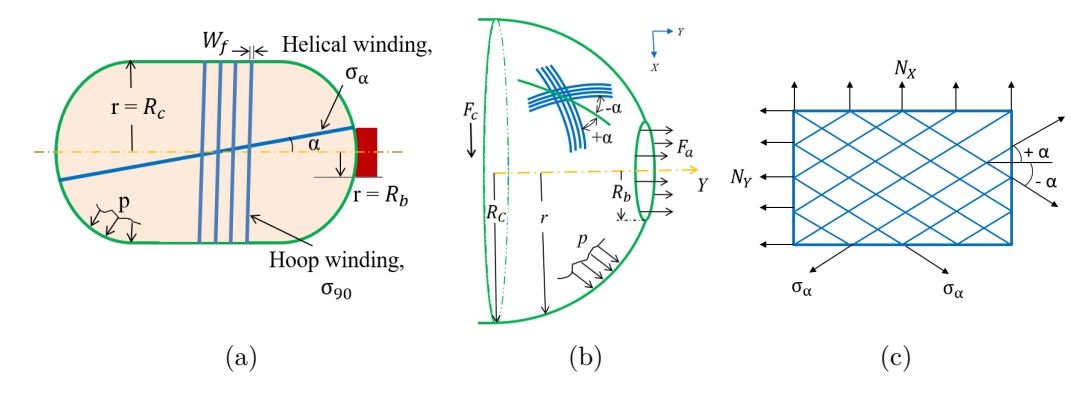


Figure 3.3: Schematic of COPV with winding over (a) the polymeric liner part, (b) only the dome part along with associated geometrical parameters, and (c) free body diagram of a netting-based element.

For the cylindrical part of COPV, a free body diagram of a unit length is shown in Fig. 3.3(c). The total helical (t_{α}) and hoop (t_{90}) layer thickness in cylindrical part is given as [13], where $F_a = pR_c/2$ and $F_c = pR_c$ are the axial and circumferential forces, respectively:

$$t_{\alpha} = \frac{pR_c}{2\sigma_{\alpha}cos^2\alpha} \tag{3.1}$$

$$t_{90} = \frac{pR_c(2 - tan^2\alpha)}{2\sigma_{90}},\tag{3.2}$$

Based on this, the total thickness (t_c) of the composite in the cylindrical part is given as:

$$t_c = t_{\alpha} + t_{90} = \frac{pR_c}{2\sigma_{\alpha}} \left[\frac{1}{\cos^2 \alpha} + (2 - \tan^2 \alpha) \right] = \frac{3pR_c}{2\sigma_{\alpha}}$$
 (3.3)

where it is assumed that $\sigma_{\alpha} = \sigma_{90}$ are the same as per NA. The thickness of the tow fibers (t_f) impregnated with resin with volume fraction (V_f) , cross-sectional area (A_f) , number of spools (N_s) is given as:

$$t_f = \frac{N_s A_f}{W_f V_f} \tag{3.4}$$

where W_f is bandwidth, as shown in Fig. 3.3(a). With the decrease in radius from the cylindrical part to the boss end there is variation in WA. This results in an increase in the thickness and decrease in BW of the composite in the polar region of the dome region which changes the dome geometry [134, 112]. Helical layer thickness buildup $t_h(r)$ as a function of radius r in the dome section is given as:

$$t_h(r) = \frac{t_{90}\cos\alpha(R_b)}{\cos\alpha(r)} \frac{R_c}{r + 2W_f(\frac{R_c - r}{R_c - R_t})^4}$$
(3.5)

where $\alpha(r)$ and $\alpha(R_b)$ are WA at a varying radius r in the dome part and at the end of the dome part respectively. Using Clairault's method, the variations of WA with radius r in the dome section are given as [135]:

$$\alpha(r) = \sin^{-1}\left(\frac{R_b}{r}\right) + \delta\left(\frac{r - R_b}{R_c - R_b}\right)^n \tag{3.6}$$

where friction effect is included by an exponential factor n for wet winding and its value is zero for frictionless winding for dry winding based on prepregs [136, 137]. δ is the WA deviation from frictional to frictionless helical winding [138]. The variation of WA over the dome part to ensure the no fiber slippage $\alpha(r)$ is given as [139]:

$$\alpha(r) = \sin^{-1}(\frac{R_b}{r}) \tag{3.7}$$

The linear density (TEX) is 800 g/km for Toray 700S 12,000 (12K) CF. The amount of resin and fiber required depends on the CFRP properties and the path of the filament wound. Based on these relationships, the parameter values obtained for winding of Type IV COPV by considering a T700S-12K filaments per tows with a single spool ($N_s = 1$) of UD CF at p_b are given in Table 3.1. Using Eq. 3.4 the bandwidth of a single tow is 2.01 mm. Maximum load is carried by UD fibers in the fiber's direction. Matrix materials are isotropic, transferring loads equally in all directions. In contrast, composite materials (fiber/epoxy), are highly orthotropic, with properties that vary depending on the direction of the load. Therefore, the design of these composites using FW plays a significant role in affecting the load-bearing characteristics of the overall system. NA provides the first approximation of design parameters of the Type IV COPV without considering the stiffness discontinuities between the hoop and helical layups, dome-cylinder transition, and non-pressure loads such as bending or axial compression [13, 140].

3.2.2 Classical laminate theory based stress analysis

CLT-based FE modeling of composite winding removes such limitations of NA. The organized stack and structured arrangement of the UD composite layer is named lamina, where the stack is defined by the orientation of each layer's fibers. A schematic of layerwise

Table 3.1: Composite layup design description from netting analysis for a given load, material, and geometrical parameters.

Parameters	Units	Values
Filament diameter, d	$\mu \mathrm{m}$	7
Filament per tow, n_f	(-)	12K
Cross section area for 12K filament, A_{12K}	mm^2	0.46
Volume fraction of carbon fiber V_f	(-)	0.66
Cross section area for single tow, A_f	mm^2	0.69
Individual layer thickness, t_f	mm	0.34
Burst pressure, p_b	MPa	157.5
Total hoop layer thickness, t_{90}	mm	12.24
Total helical layer thickness, t_{α}	mm	25.16
Total thickness in cylindrical part, t_c	mm	37.4
Total number of hoop layers, n_{ho}	(-)	36
Total number of helical layers, n_{he}	(-)	76
Total number of layers, n_t	(-)	112

composite winding is shown in Fig. 3.4(a) along with a single layer that has the WA, α in Fig. 3.4(b). For stress analysis, the local stiffness matrices for all layers in the local (1, 2) coordinate system are set up in global (X, Y) coordinate systems.

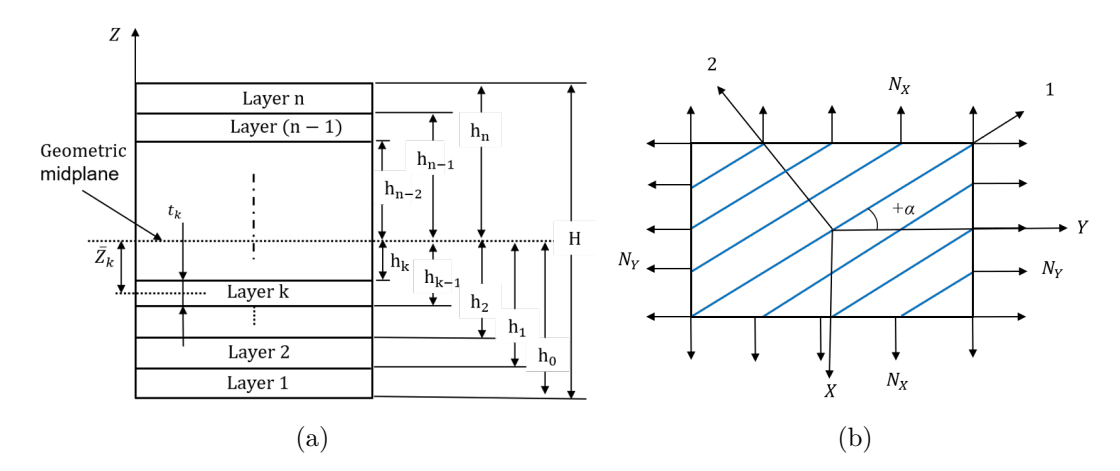


Figure 3.4: Schematic of CLT for (a) multi-layer lamina, (b) a schematic diagram with local (1,2) and global (X,Y) coordinate system.

The CLT is based on the following assumptions:

- 1. Normal lines to the midplane (see, 3.4(a)) before and after deformation remain straight and normal to the plane of deformation.
- 2. Each layer is perfectly bonded.
- 3. The thickness of the layer is constant throughout the laminate.
- 4. Each layer obeys Hooke's law.

In CLT, the resultant normal force components (see Fig.3.4(b)) take the geometry and loading effect in cylindrical or dome geometry to estimate the stress-strain behavior. CLT

enables the calculation of stresses and strains within layers of composite winding of the Type IV COPVs subjected to varying pressures of the gas. Further, the global stiffness matrix of the layer is set using the force and moment equilibrium over the layer as per Eq. 3.8. The relation of loads, ABD matrix, and strain component is written in matrix form as [141]:

$$\begin{bmatrix} \mathbf{N} \\ \mathbf{M} \end{bmatrix} = \begin{bmatrix} \mathbf{A} & \mathbf{B} \\ \mathbf{B} & \mathbf{D} \end{bmatrix} \begin{bmatrix} \boldsymbol{\epsilon}^o \\ \mathbf{k} \end{bmatrix}$$
 (3.8)

where ϵ^o is the mid-plane strain vector, k is the curvatures vector, A is the laminate extensional stiffness, B is the coupling stiffness, D is the bending stiffness, and M is the resultant couple moment. The applied normal resultant loads $(N_X \text{ and } N_Y)$ for the cylindrical and hemispherical dome parts are shown in Eq. 3.9 and Eq. 3.10 respectively [12].

$$N_X = pR_c; N_Y = pR_c/2 \tag{3.9}$$

$$N_X = N_Y = pR_c/2 \tag{3.10}$$

The resultant stress components are evaluated by the ABD matrix. The composite design using CLT in Abaqus and governing equations of composite layup are included in FEA using the UVARM subroutine (required to specify user-defined output variables at all material calculation points of elements). The CF composite layups with proper sequencing of laminate, and orientation play an important role in understanding the critical stress responsible for the strength of Type IV COPV.

3.2.3 Tsai-Wu failure index

In the present study, the Tsai-Wu failure index (F.I) is used to estimate the failure of Type IV COPV at different H₂ gas pressures. F.I determines the integrity of composite orthotropic lamina. It accounts for strength tensors and can distinguish between tensile and compressive strengths. The general form of quadratic F.I criteria is expressed as [14]:

$$F.I = F_{11}\sigma_{11}^2 + F_{22}(\sigma_{22}^2 + \sigma_{33}^2) + 2F_{22}\sigma_{22}\sigma_{33} + 2F_{12}\sigma_{11}(\sigma_{22} + \sigma_{33}) + F_{12}(\sigma_{11} + \sigma_{22}) + F_{22}\sigma_{33} + F_{66}\sigma_{12}^2 < 1$$

$$(3.11)$$

where σ_{ij} denotes the stress components and the coefficients are calculated using the following relationship:

$$F_{1} = \frac{1}{\sigma_{1t}^{*}} - \frac{1}{\sigma_{1c}^{*}}, F_{2} = \frac{1}{\sigma_{2t}^{*}} - \frac{1}{\sigma_{2c}^{*}}, F_{11} = \frac{1}{\sigma_{1t}^{*}\sigma_{1c}^{*}}, F_{22} = \frac{1}{\sigma_{2t}^{*}\sigma_{2c}^{*}}, F_{66} = \frac{1}{\tau_{12}^{*2}},$$

$$F_{12} = -\frac{0.5}{\sqrt{\sigma_{1t}^{*}\sigma_{1c}^{*}\sigma_{2t}^{*}\sigma_{2c}^{*}}}$$
(3.12)

Here, the allowable tensile and compressive strengths in two material directions are

denoted by σ_{1t}^* , σ_{2t}^* and σ_{1c}^* , σ_{2c}^* , while τ_{12}^* is the allowable shear strength.

3.2.4 Stress ratio

Stress ratio (SR) is defined as the ratio of stress in fiber at specified minimum burst pressure (σ_{p_b}) to stress in fiber at p_{nwp} (σ_p) and its value is 2.25 for CF material of 70 MPa Type IV COPVs as per ISO 19881 standards [101, 1].

$$SR = \frac{\sigma_{p_b}}{\sigma_p} \tag{3.13}$$

3.3 Design Aspects and Finite Element Method used for the Analysis of Type IV COPV

The design of COPV using the FE method consists of the following steps: CAD model development, material assignment to all parts, meshing, specifying boundary conditions, and interactions between parts. The estimation of failure is obtained based on the set failure criteria with increased pressure of H_2 gas to the p_b . Each of these steps used for the analysis of COPV is detailed in the following part of this section.

3.3.1 CAD model and material properties

CAD modeling of Type IV COPV consists of the development of the geometric model of HDPE liner, and the open-end, and closed-end metallic bosses, as shown in Fig. 3.5. The shape of the liner and bosses selected for the design of the COPV is motivated by the ongoing experimental research work on the manufacturing and failure behavior of Type IV COPV in our research group, along with the work available in the literature [142, 143]. The open-end boss hosts the gas filling valve with radius r_{iv} as marked in the zoomed view of the open-end dome section. The COPV considered in this work has an 18 L water volume capacity. The thickness of the HDPE liner is considered to be 5 mm, which is sufficient to act as a H_2 permeation barrier [1].

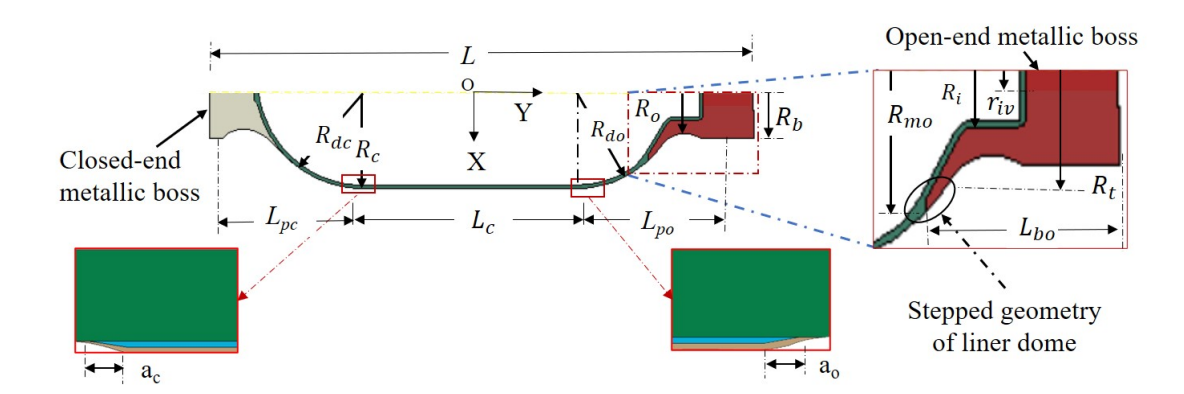


Figure 3.5: A 2-D CAD model of the liner-boss assembly of Type IV COPV used in this study.

The maximum radial and axial dimensions of the boss are named R_{mo} and L_{bo} respectively. The turnaround radius of helical layers wrapping direction is considered to be the outer surface of the open and closed-end bosses, also termed as polar boss region. Dimensions R_c , R_b , R_o , R_{do} and R_{dc} mark the radius of the cylindrical part of the liner, radius of the polar boss end region, boss minimum outer radius, open-end metallic boss dome radius, and closed-end metallic boss dome radius, respectively. The transition radius, R_t marked in the zoomed view of the open-end dome section is considered for bosses from the beginning of the fillet. The open-end boss has a geometry such that it is placed over the stepped dome of the liner. The stepped geometry of the liner dome leads to an increased wall thickness in the vicinity of the step and also provides better gripping of the boss, which will be discussed later. The considered geometry of the boss on the closed end of the COPV maintains the symmetry of the composite winding on both domes of the liner. While the total length of COPV is marked as L, the cylindrical section of COPV has length L_c , and the open-end and closed-end boss sections have lengths L_{po} and L_{pc} , respectively. The initial parameters considered for the CAD modeling of COPV are mentioned in Table 3.2. The lengths a_o and a_c marked at both ends of the cylindrical section in the insets of Fig. 3.5 describe the tapered end of the hoop layer plies. This end type of hoop layer is used for designing the composite winding of COPV with the ply drop location at the end of the cylindrical section.

Table 3.2: Design parameters of liner-boss assembly with composite specifications used for Type IV COPV design (all dimensions are in mm).

\overline{L}	L_c	L_{po}	L_{pc}	L_{bo}	R_c	R_b	R_o	R_{mo}	R_t	R_i	r_{iv}	a_c	a_o	t_c
672	274	177	179	132	121	60	53.46	87.71	75	34	12	2.0	2.0	38.08

It is to be noted that the cylindrical section of COPV hosts both hoop and helical layers of composite, while the dome section hosts only the helical layers. This leads to a difference in the thickness of winding in cylindrical (t_c) and dome sections (t_h) , as highlighted in the 3-D model of COPV in Fig. 3.6. In the FE analysis result section, it will be discussed about the removal of the sharp transition in composite winding thickness at the interface of cylindrical and dome sections [47].

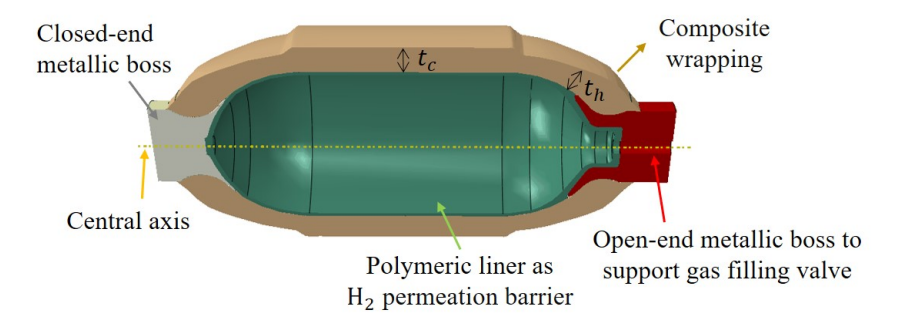


Figure 3.6: A 3-D Type IV COPV model with integrated parts.

The selected HDPE material for the polymeric liner can achieve the US, DOE targets of permeation limit $(0.05 \text{ (g/hr)/Kg of H}_2)$ at p_{nwp} as per ISO 11119-3 [82]. It is a better choice over PA6 and PA12 in terms of low-to-high temperature performance requirement of -40°C to 85°C, making it a better choice for H₂ storage in Type IV COPVs [144, 145, 146]. Aluminum alloy grade Al6061-T6, which is heat-treated, is considered the boss material. It has a lower density and higher thermal conductivity than stainless steel, resulting in higher thermal diffusivity, which allows it to release the maximum temperature (limited to 85°C) reached inside the 70 MPa Type IV COPVs during fast filling. It is best suited due to its good strength, and toughness under a high-pressure H₂ environment, showing good resistance to HE as per GB/T 35544 safety standards [88]. Toray T700S CFs with 12K tows (T700S-12K-50C) are considered as reinforcement material. In contrast, compatible epoxy LY556 and XY54 hardener combined are considered as a matrix material in the ratio 2:1 for composite wrapping with V_f of 66% [147, 148]. Matrix helps in transferring the load from one reinforcement to another. The CF and matrix should have high interfacial bonding for reliable usage. Material properties assigned for the aluminum metallic boss [149, 150], matrix [148], polymeric liner [88], CF [147], and subsequently the composite lamina are mentioned in Table 3.3 and 3.4 respectively. The failure behavior of composite wrapping is governed by its strength properties as mentioned in Table 3.5 that are used for calculating the F.I.

Table 3.3: Mechanical properties of the metallic boss (Al6061-T6), matrix (LY556-XY54) and polymeric liner (HDPE) material used for Type IV COPV.

Property (Units)	Al6061-T6 [149]	LY556-XY54	HDPE [88]
		[148]	
Elastic modulus (GPa)	74.12	3.5	0.65
Poisson's ratio (-)	0.28	0.34	0.41
Tensile strength (MPa)	281	72.2	24.1
Density (kg.m ⁻³)	2700	1200	942

Table 3.4: Mechanical properties of T700S-12K-50C carbon fiber reinforcement and composite lamina.

Properties (Units)	Carbon	fiber	Composite
	[147]		lamina
Elastic modulus in fiber direction, E_{11} (GPa)	235		156.3
Elastic modulus in transverse direction, E_{22} (GPa)	28		11.2
Elastic modulus in transverse direction, E_{33} (GPa)	28		11.2
Shear modulus, $G_{12} = G_{13}$ (GPa)	50		4.02
Shear modulus, G_{23} (GPa)	10		3.91
Poisson's ratio, $v_{12}=v_{13}$ (-)	0.23		0.27
Poisson's ratio, v_{23} (-)	0.3		0.43
Density, ρ (kg.m ⁻³)	1800		1596

For the creation of a composite layout, a node-set was created on the outer surface of the liner-boss assembly (see Fig. 3.5), over which the composite layers interact. Based

Table 3.5: Strength properties of the composite

Strength properties of composite lamina (Units)	Value
	[151]
Longitudinal tensile strength, σ_{1t}^* (MPa)	3234
Longitudinal compressive strength, σ_{1c}^* (MPa)	2400
Transverse tensile strength, σ_{2t}^* (MPa)	111
Transverse compressive strength, σ_{2c}^* (MPa)	290
Shear strength, τ_{12}^* (MPa)	50

on the design data from the NA as given in Table 3.1, the inputs are provided for all the composite layers in the WCM plugin. As an input for the composite layers, a minimum helical WA was determined using ratio R_b/R_c as per Clariuts principle and evaluated WA is 25°, considered as reference angle [13]. The hoop layers are placed at a uniform WA of 90° with constant thickness in the cylindrical part. The hoop layers cover the cylindrical part, while helical layers cover both the cylindrical as well as the hemispherical dome parts [152]. Helical layers WA along the cylindrical part remain the same, while across the dome part, it starts to decrease progressively from the cylindrical tangent line to the top end of the boss as per Eq. 3.7. The thickness of each layup is 0.34 mm. The composite layups are sequenced to achieve the same overall thickness in the cylindrical part as per NA. The N_s for the 1-41 layer and the 42-112 layer are 1 and 2, respectively. The number of layers (n), layer type (hoop/helical), composite material, WA, BW, and N_s are summarized in Appendix-I.

3.3.2 Boundary condition and meshing

To simulate the static burst test, an axisymmetric Type IV COPV model is considered for simulations. The boundary conditions applied are shown in Fig. 3.7. As shown, pressure is applied on the inner periphery of the polymeric liner. If the COPV was not structurally damaged at the minimum p_b , then the internal pressure was increased until the burst to obtain the maximum burst pressure ($p_{ult.}$). Both hoop-helical winding and the liner-boss assembly are meshed using four-noded axisymmetric reduced integration elements, CAX4R. Convergence studies were performed to select the mesh size for the simulation model.

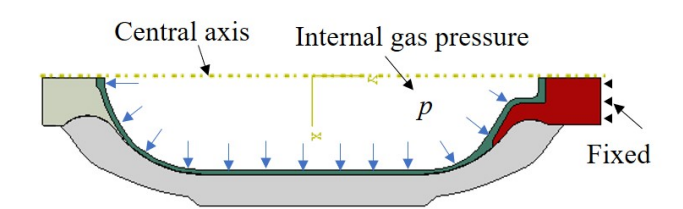


Figure 3.7: Load and boundary condition used to simulate p_b test of Type IV COPV.

3.3.3 Manufacturing defects found and need to analyze using FEA

To understand the role of manufacturing defects, several possible defects are considered in the design of the Type IV COPV. These defects include the sharp transition in the composite winding at the transition zone of the cylindrical and dome part (D1), possible gaps at the multi-material junction of the plastic liner-metallic boss-composite winding on the open-end dome (D2) and closed-end dome (D3) side, the shape of the metallic boss in contact with the composite winding at the open-end (D4) and closed-end (D5) dome sides, as shown in Fig. 3.8.

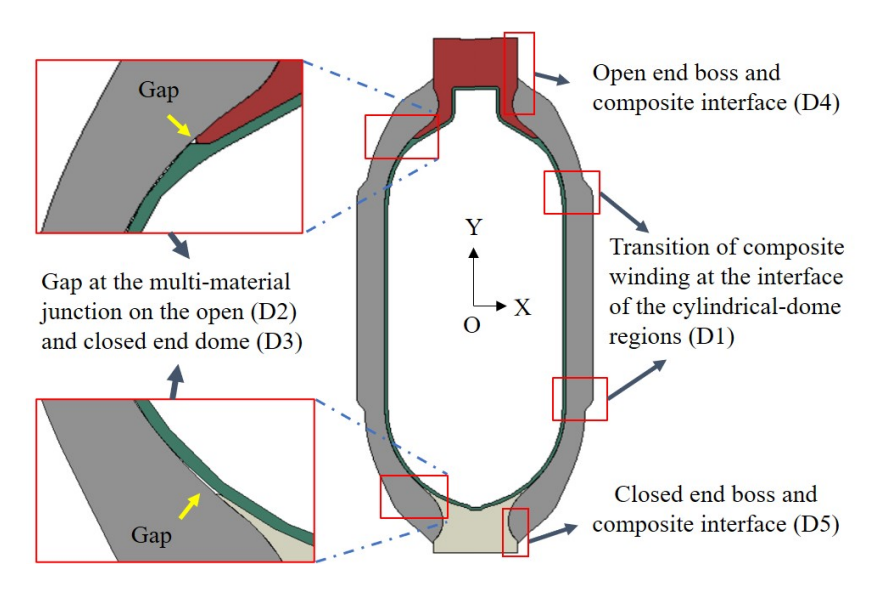


Figure 3.8: Manufacturing defects considered in the liner-boss-composite model.

For studying the role of defects D1, D2, D3, D4, and D5; all interfaces between two different materials of the Type IV COPV are considered to be permanently bonded. The effect of individual defects on failure behavior is studied through five different simulation cases. For case I: the defects D1, D2, and D3 are considered in the model. For case II: only D2 and D3 defects are considered, while the transition in the composite winding at the transition zone of the cylindrical and dome part of COPV is made smooth. For case III, defects D2 and D3 are further removed by filling the gaps with different sleeve materials to analyze the failure behavior of composite layers. In case IV, the design variation of the open (D4) and closed-end (D5) metallic bosses are studied to understand the failure at the boss-composite coupling region. The following assumptions are considered in modelling and FEA:

- 1. Boss on the closed end of the COPV maintains the symmetry of the composite winding on both domes of the liner.
- 2. 2-D axisymmetric Type IV COPV modelled due to symmetry and to reduce computational time.

- 3. Boundary conditions are applied on one open end of the boss to implement the realistic conditions.
- 4. All the interfaces (liner-boss, boss-composite, and liner-composite) are rigidly bonded thoroughly.

3.4 Results

To understand failure in Type IV COPV, the F.I of the composite winding is tracked till the p_b . For case I, Fig. 3.9(a) shows the contour plot in the composite winding, and Fig. 3.9(b) shows the variation of F.I in the first hoop (Layer Number 1: Hoop) and the first helical layer (Layer Number 5: Helical) in the composite winding.

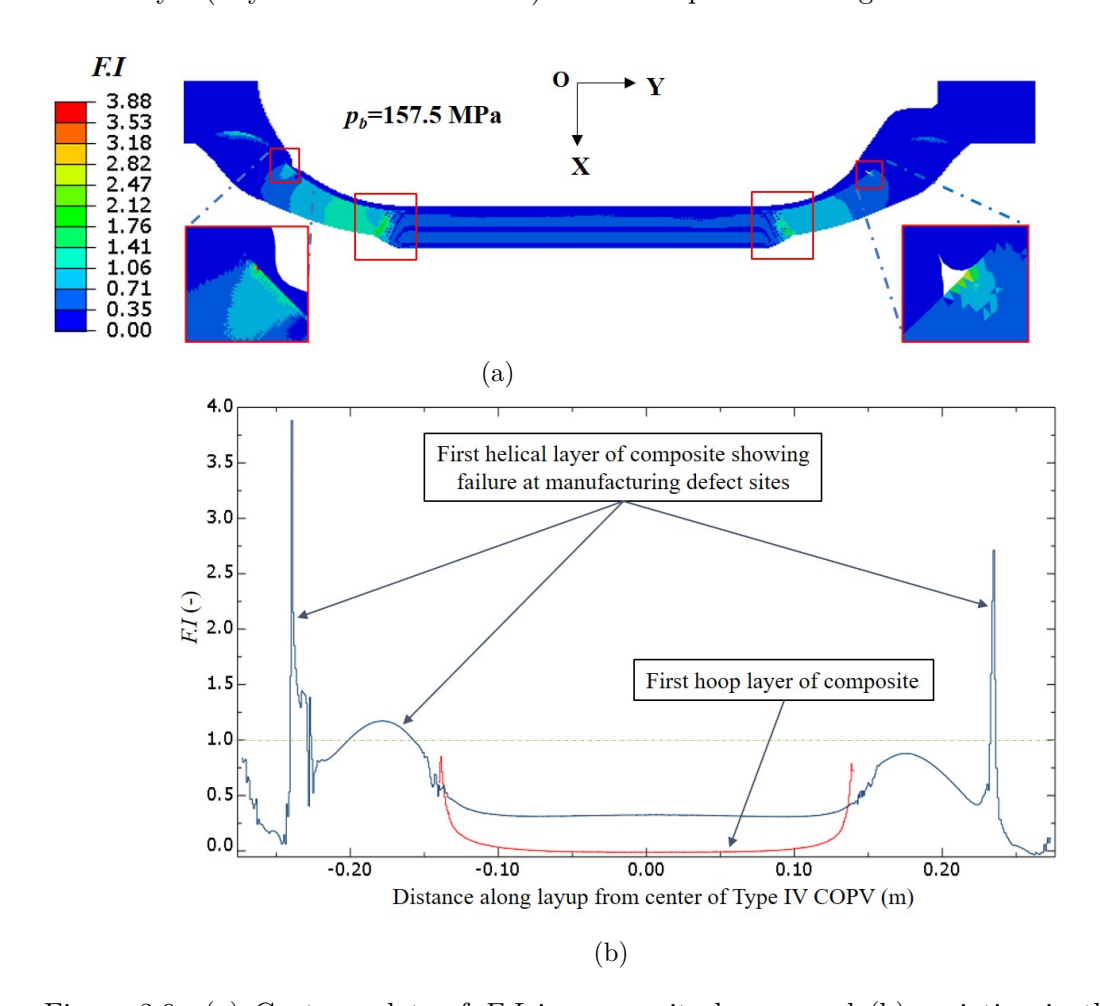


Figure 3.9: (a) Contour plots of F.I in composite layers, and (b) variation in the F.I along the first helical and first hoop layer of Type IV COPV with manufacturing defects considered as per case I.

The first helical layer is in direct contact with the junction of the plastic liner and the metallic boss where due to defects D2 and D3, a sharp jump in F.I (> 1) is observed, thus confirming the site of failure. The site of defect D1 also shows a high value of F.I (> 1), which confirms another site of failure in Type IV COPV for case I. The unsymmetrical variation of F.I in the composite layup is due to a slight variation in the shape of the open

and closed-end domes of the plastic liner. For case I, the von Mises stress contour in the composite winding is shown in Fig. 3.10(a) while the variation of von Mises stress in the first hoop and first helical layer is shown in Fig. 3.10(b). It is shown that while the hoop layers carry the maximum load in the composite winding, it is the helical layers that lead to the failure.

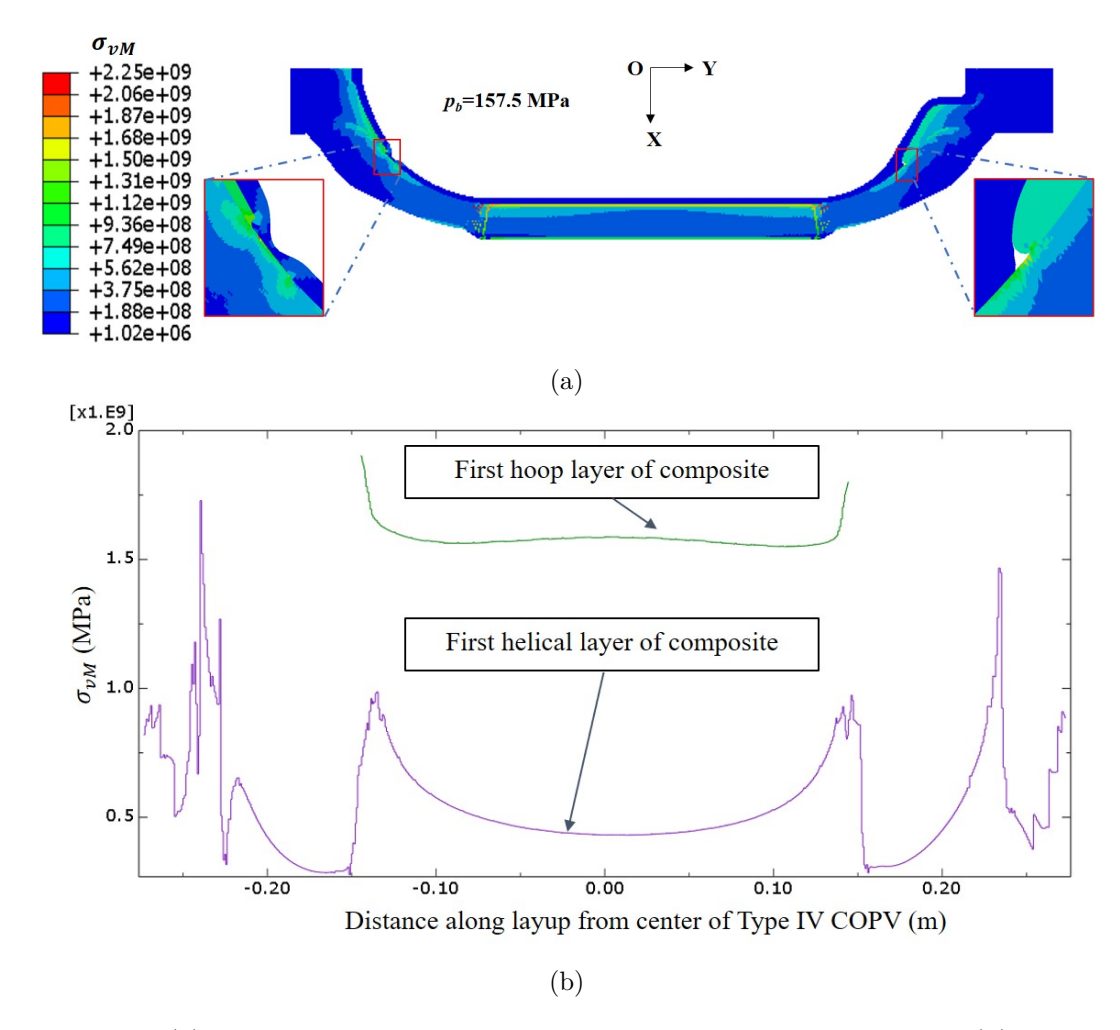


Figure 3.10: (a) Contour plots of von Mises stress in composite layers, and (b) variation in the von Mises stress along the first helical and first hoop layer of Type IV COPV with manufacturing defects considered as per case I.

In case II, our objective is to highlight the role of sharp transition (D1) of the composite winding in the transition zone of the cylindrical and dome part of COPV on failure. To achieve this, defect D1 is removed from the designed COPV while maintaining the other two defects, D2 and D3, as in case I (see Fig. 3.11). To remove the sharp transition, the hoop ply drop locations on both open- and closed-end domes are modified by the nominal retraction length. The length of nominal retraction for the $L_{\rm pc}$ region and $L_{\rm po}$ region is denoted by $a_{\rm c}$ and $a_{\rm o}$, respectively, [47].

The composite layer thickness build-up at different locations in the open and closed dome part of case II is shown in Fig. 3.11, respectively. The thickness of the composite in the cylindrical part is 38.08 mm. The ply-drop in the dome region after the dome-cylindrical

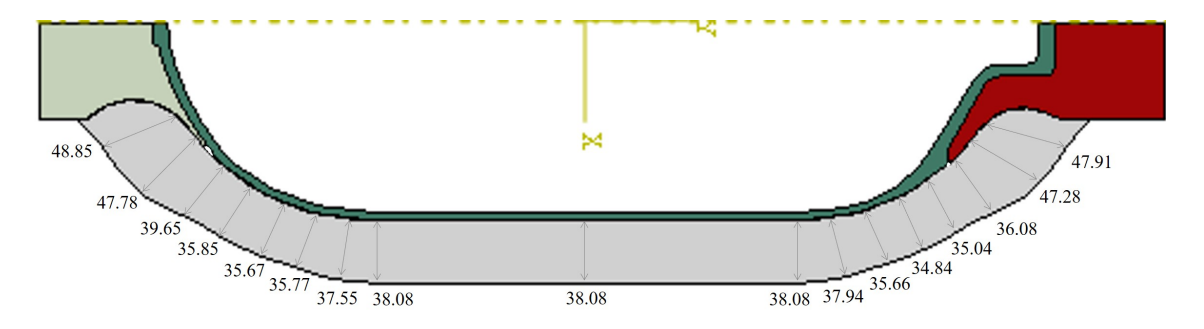


Figure 3.11: Design of Type IV COPV with the removal of manufacturing defect D1 from the cylindrical-dome part transition, with thickness buildup at different locations for safer design for open dome part and closed dome part.

interface region acts as a doily. The variation in the ply drop location of each hoop layer accounts for the smooth transition of composite layers. In addition, the maximum thickness build-up on the polar end bosses ensures that there will be no ejection of bosses from the dome ends at p_b . For case II, while the failure is prevented at the D1 defect site, the F.I of helical fiber at the liner-metallic boss junction shows a sharp rise due to the localization of stresses at the D3 defect site, as shown in Figs. 3.12 and 3.13. The D3 defect site leads to maximum damage as a sharp jump, as shown in the contour plot in F.I. (> 1) and the high F.I. in Figs. 3.12(a) and 3.12(b), respectively.

The contour and line plots for the first hoop and helical layer and von Mises stress are shown in Fig. 3.13(a) and 3.13(b), respectively. These figures also showed the role of defective geometry at the liner-metallic boss junction on the propensity of failure. While the gap at the D2 defect site is much smaller and shielded by the thickest part of the liner, the gap at the D3 defect site is much larger and flatter, with a thin layer of the liner covering it. During pressurization, the plastic liner at the D3 defect site filled the gap while sharply increasing the stress level at the edge of the D3 defect site.

To prevent the failure of Type IV COPV from these gaps as defect sites, it is proposed to fill these gaps with suitable sleeve material as in case III with defects D2 and D3 removed. An axisymmetric model of Type IV COPV, with the gaps at the liner-metallic boss junction filled by a sleeve material, is shown in Fig. 3.14. The following materials are considered sleeve material: Al6061-T6 (same as boss material), resin (Epoxy LY556 and XY54 hardener mixture, same as used for CFRP matrix material), HDPE (same as plastic liner material), and Teflon, the properties of which are mentioned in Table 3.8) [153]. The selection of the sleeve material is performed based on the reduction of F.I to be within the safe limit (F.I < 1) as shown in Fig. 3.15. The resin and Teflon as sleeve material show the lowest F.I values (within the safe limit) throughout the first helical layer of composite, with Teflon showing a slightly lower value on the open dome region compared to resin material. Based on these results, Teflon material was used to fill the gap for further analysis of the role of other defects in COPV.

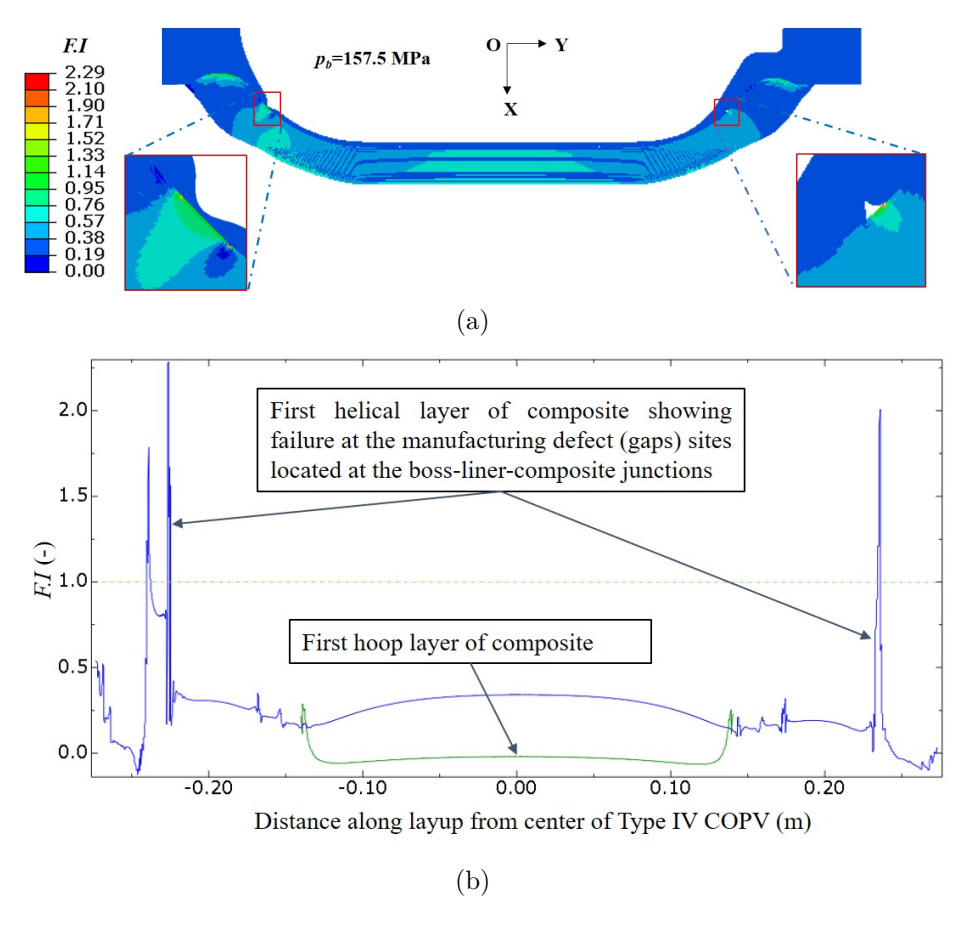


Figure 3.12: Variation of F.I of Type IV COPV with the removal of sharp transition at dome-cylinder interface manufacturing defect (a) the contour plot variation, and (b) the line plot for the first helical and hoop layer.

Table 3.6: Mechanical properties of the sleeve material.

Material	Elastic	modulus	Poisson's ratio	Tensile strength	Density
grade	(GPa)		(-)	(MPa)	$(\mathrm{kg.m}^{-3})$
Teflon [153]	3.65		0.25	2.4	760

Due to the lack of a specific standard and the absence of sufficient relevant literature for the design and manufacturing of metallic bosses, it is crucial to understand the role of the boss profile in the failure of Type IV COPV. In case IV, the role of open and closed boss geometric profile (that interacts with the composite) on the failure behavior of COPV is studied at the minimum required $p_b = 157.75$ MPa. With the removal of manufacturing defects associated with the composite winding and liner-boss junction, it is crucial to understand the role of the shape of metallic bosses in the failure of COPV. In case IV, the role of open-end and closed-end boss profiles (that interact with the composite winding) on the failure behavior of COPV is studied at the p_b . Three different profiles of open-end and closed-end bosses are studied as shown in Fig. 3.16. These include a straight profile of bosses where they connect with the composite winding along with a sharp transition into the flange region (referred to as A1A2 profile of bosses in Fig. 3.16(a)), straight profile of bosses where they connect with the composite winding along with a fillet based transition

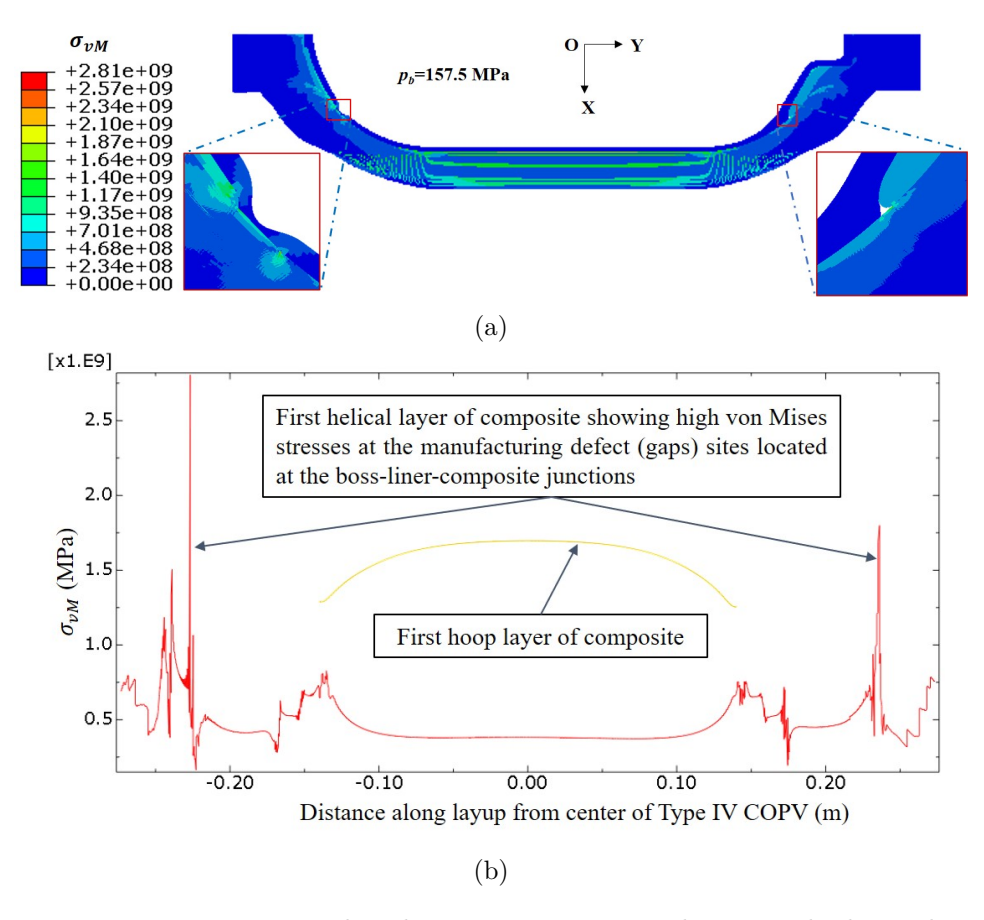


Figure 3.13: von Mises stress distribution in composite layers and plastic liner after removal of sharp transition at dome-cylinder interface manufacturing defect (a) contour plot variation and (b) line plot for the first helical and hoop layer.

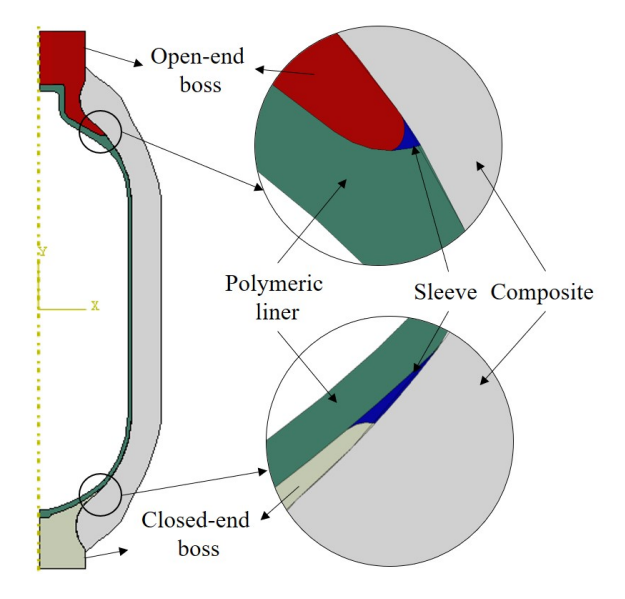


Figure 3.14: Type IV COPV axisymmetric model with sleeve material used to fill the liner-boss-composite materials gap.

into the flange region (referred as B1B2 geometry of bosses in Fig. 3.16(b)) and concave profile of bosses where they connect with the composite winding along with a fillet based transition into the flange region (referred as C1C2 geometry of bosses in Fig. 3.16(c)),

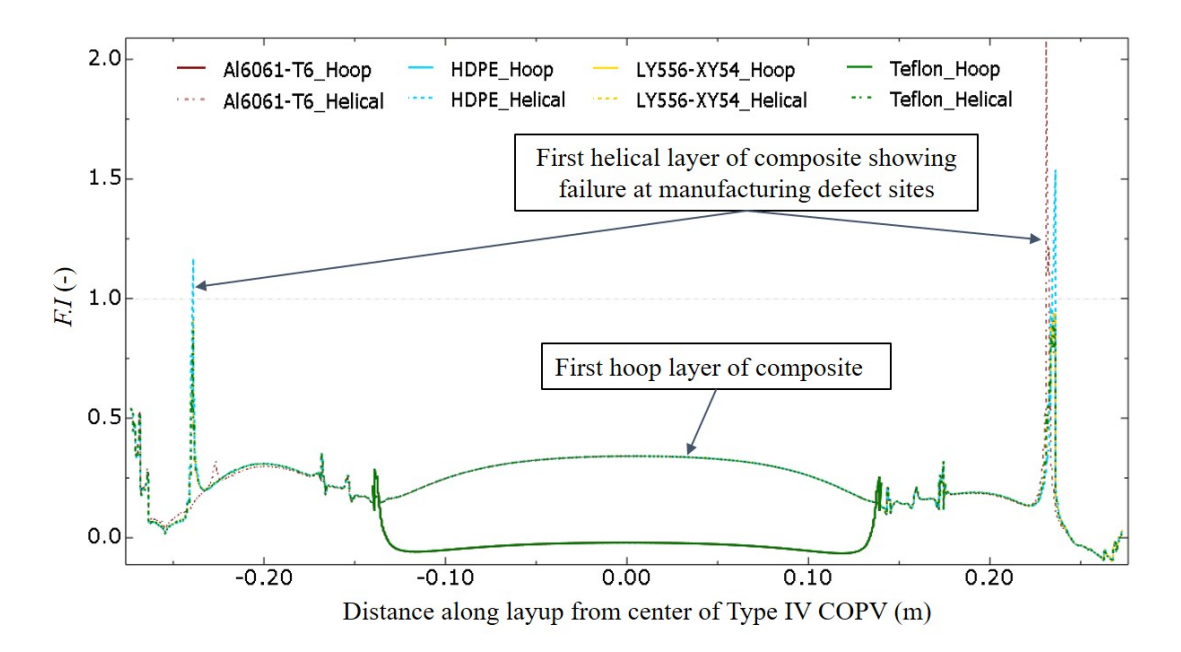


Figure 3.15: F.I at multi-material interface of both end domes.

which is also used in case I, II and III. The design parameters of three profiles of open-end and closed-end bosses studied in case IV are given in Table 3.7. Fillet radius R_f , with the corresponding coordinates of the center point (x_f, y_f) , are angle θ_f , boss inner radius R_i are shown in Table 3.7 along with the dimensions of R_o , R_{do} and R_{dc} , as defined in sub section 2.3.1.

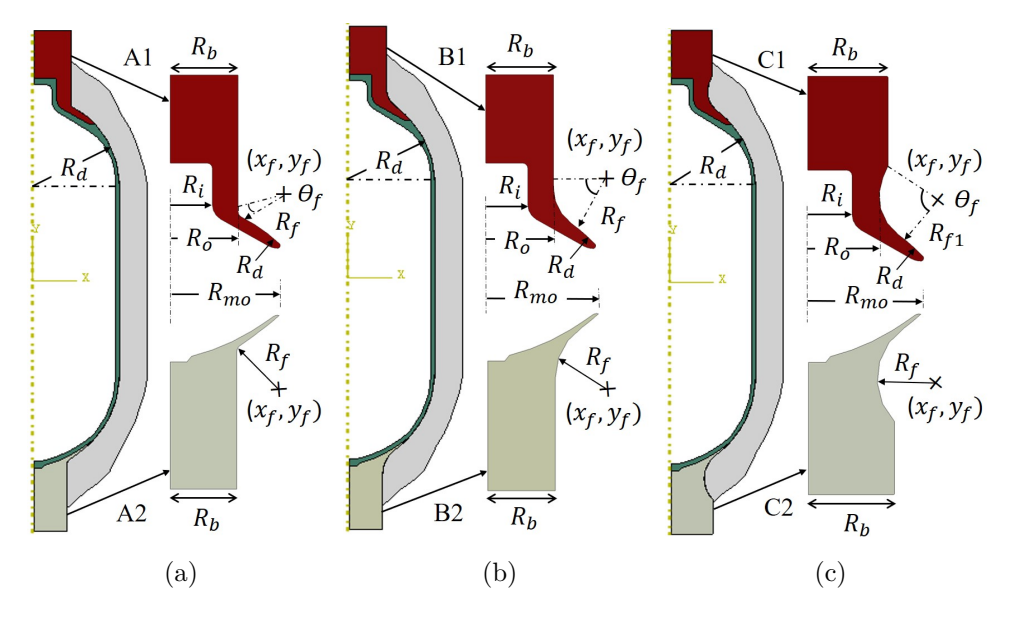


Figure 3.16: Various composite-boss interface designs for the open dome end and closed dome end, (a) pure cylindrical type, (b) cylindrical with curvature in starting of the composite, (c) curvature provided with cylindrical profile with more thickness.

The F.I contour plots for A1A2, B1B2, and C1C2 boss shapes are shown in Fig. 3.17. A rise in F.I to unsafe values for the A1A2 profile indicates that the sharp corner in the

Table 3.7: Design parameters of three profiles of open-end and closed-end bosses studied in case IV.

	A1A2		В	1B2	C1C2		
Features	A1	A2	B1	B2	C1	C2	
$R_f \text{ (mm)}$	5	5	33.74	41.21	33.74	41.21	
$x_f, y_f \text{ (mm)}$	(60, 200)	(50, -300)	(90, 220)	(90, -320)	(90, 200)	(90, -310)	
$R_b \text{ (mm)}$	53.46	53.46	53.46	53.46	60	60	
θ_f (°)	63.04	55.94	54.09	56.63	93.08	105.85	
$R_i \text{ (mm)}$	34	34	34	34	34	34	
$R_o \text{ (mm)}$	53.46	53.46	53.46	53.46	53.46	53.46	
$R_b \text{ (mm)}$	53.46	53.46	53.46	53.46	60	60	
$R_{mo} \text{ (mm)}$	87.71	87.71	87.71	87.71	87.71	87.71	
$R_d \text{ (mm)}$	124	125.5	124	125.5	124	125.5	

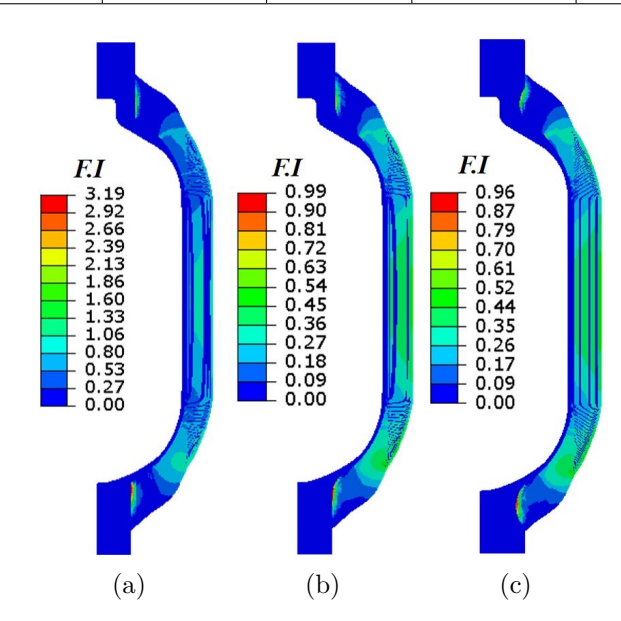


Figure 3.17: F.I variation for composite-boss interface designs for the open dome end and closed dome end, (a) pure cylindrical type, (b) cylindrical with curvature in starting of composite, (c) curvature provided with cylindrical profile with more thickness.

boss profile to connect the straight section with the flange section is not desirable. The rounded corner in the boss profile B1B2 prevents such a sharp rise in the F.I value and is further reduced by using a C-type curved profile C1C2 of the boss to satisfy the safe limits at the minimum required p_b . F.I plot along the first helical and hoop layers of composite that interacted with different boss profiles are shown in Fig. 3.18.

The manufacturing defects in the Type IV COPV in the transition zone of composite winding (D1), the gaps in the liner-boss-composite winding junction (D2 and D3), and at the boss-composite winding interface (D4 and D5) are fixed. The von Mises stress distribution in composite after removal of all defects is shown in Fig. 3.19 (a) and (b). The stresses are reduced for the first hoop and helical layer, and the maximum equivalent stress is generated in the cylindrical section only. This shows the result of a safe design per the COPV design rule. This also validates the safety criteria of the Type IV COPV design.

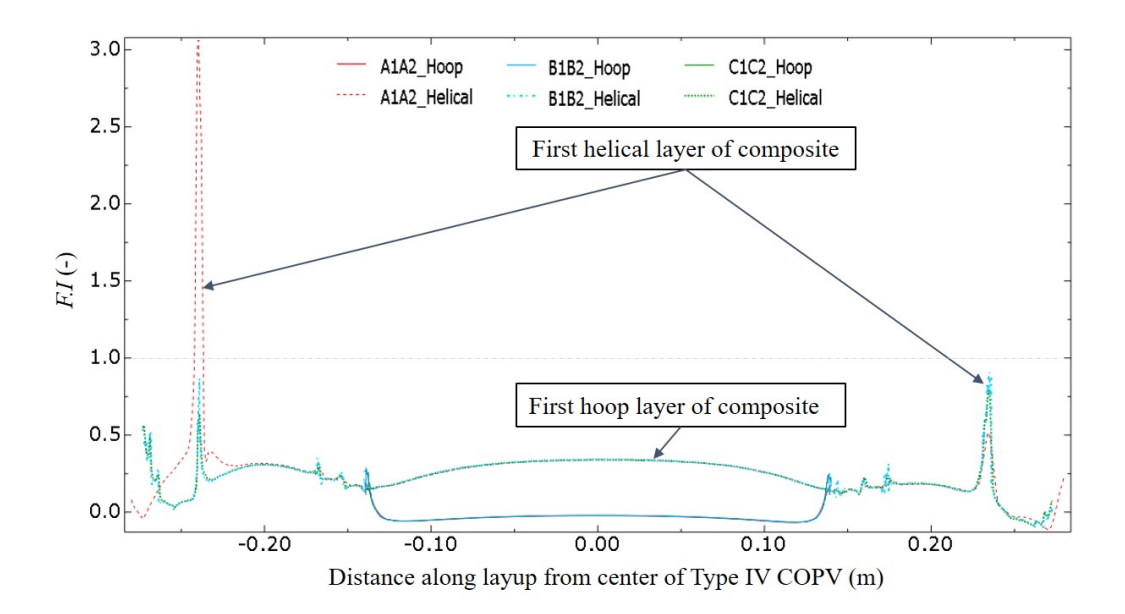


Figure 3.18: F.I for various profiles of boss shape.

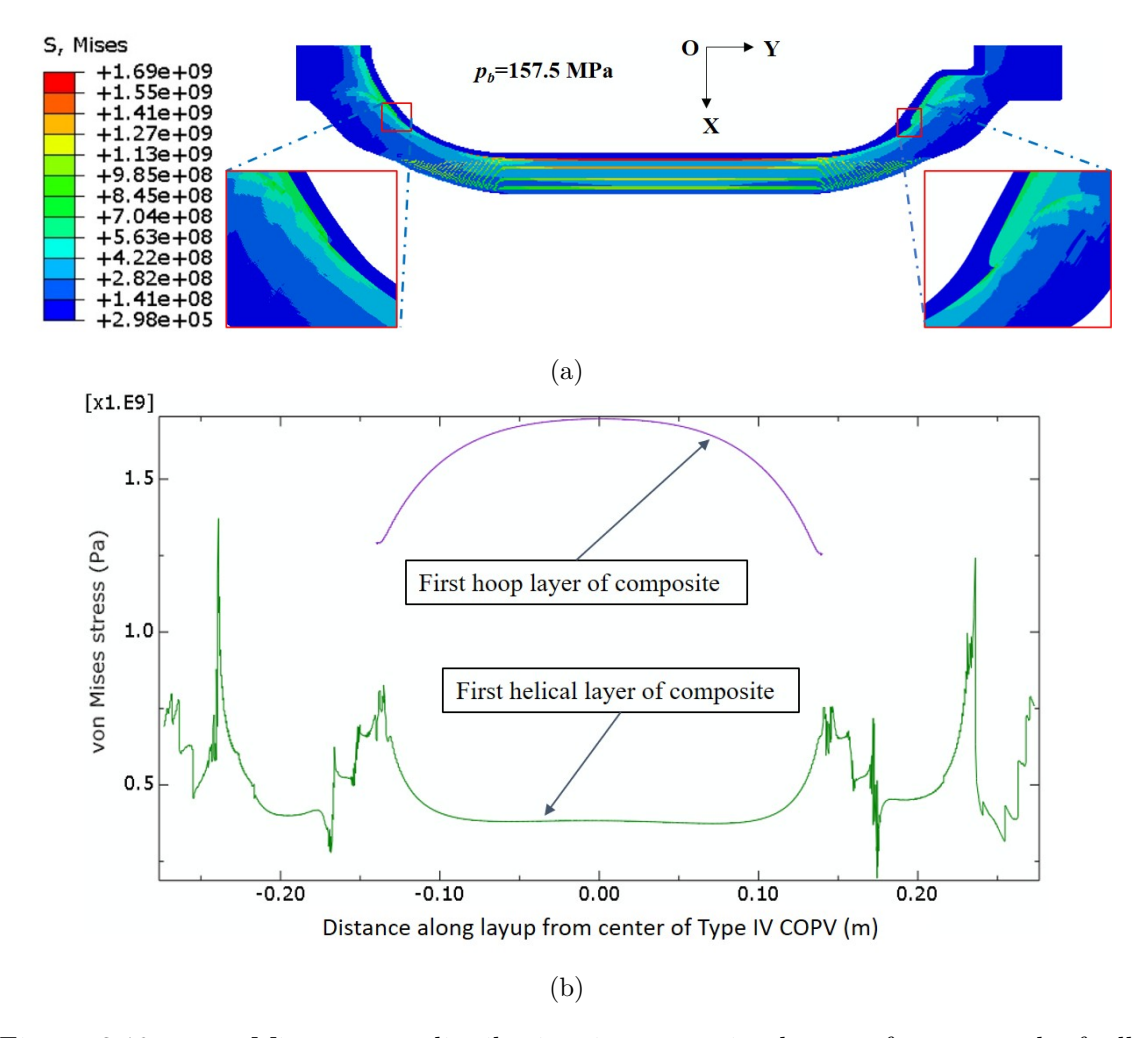


Figure 3.19: von Mises stress distribution in composite layers after removal of all manufacturing defects (a) contour plot variation and (b) line plot for the first helical and hoop layer.

After fixing all defects, Type-IV COPV was tested above the minimum required p_b to evaluate the maximum burst performance of the proposed design [15]. The F.I value and contour for the composite assembly at a design p_b load of 157.5 MPa, 159.25 MPa, 161 MPa, and 162.75 MPa are shown in Fig. 3.20 (a), 3.20 (b), 3.20 (c) and 3.20 (d), respectively. The Type IV COPV model demonstrated safe performance under pressure, sustaining a p_b of 157.5 MPa with a SR of more than the minimum required of 2.25.

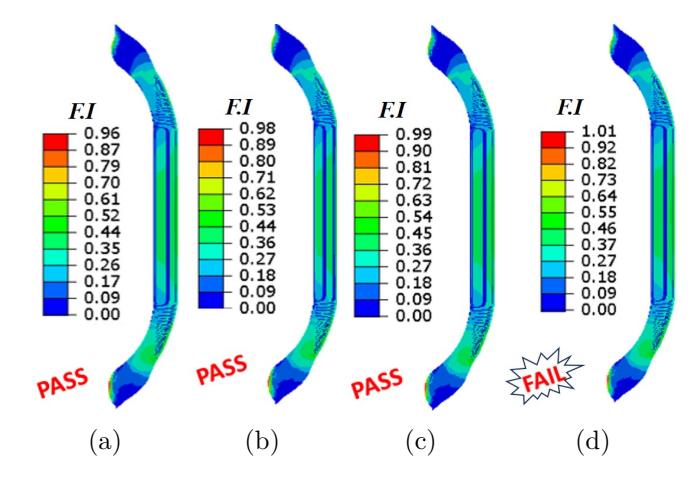


Figure 3.20: F.I at various design pressures (minimum p_b to ultimate $p_{ult.}$ value).

The baseline safety margin and the progressive load analysis for the failure threshold of the estimated p_b corresponding to p_{nwp} are as follows:

- Baseline safety margin: At p_b of 157.5 MPa, the maximum F.I reached 0.96, which is below the critical threshold (F.I < 1).
- Failure threshold for progressive applied load: Structural failure (F.I > 1) occurs at a p_b of 162.75 MPa, establishing this as the critical burst pressure limit, where the F.I reaches 1.01 and the corresponding SR is 2.32 (> 2.25).

The F.I for all the cases that are considered for the manufacturing defects are summarized in Table 3.8. In Table F.I are mentioned as 3.88, 2.29, 2.19, 1.54, 0.98, 0.96, 3.19, 0.99, and 0.96 for case I, II, III(AA), III(HDPE), III(Resin), III(Teflon), IV(A1A2), IV(B1B2), and IV(C1C2) respectively. In brackets of case III and case IV represent the different sleeve materials and the various shape of boss shapes that interacted with the composite material, respectively.

Table 3.8: F.I for different cases considered for manufacturing defect.

Case	Ι	II	III	III	III	III	IV	IV	IV
			(AA)	(HDPE)	(Resin)	(Teflon)	(A1A2)	(B1B2)	(C1C2)
F.I	3.88	2.29	2.19	1.54	0.98	0.96	3.19	0.99	0.96

3.5 Discussion

The work is motivated by the ongoing experimental work on the development of Type IV COPVs with p_{nwp} =70 MPa using a pre-fabricated liner. The pre-fabricated liner considered in the experimental work has a neck (see, Fig. 3.6) with an opening for gas input on one of the dome while the other dome is closed. The metallic boss with a threaded opening for the valve is then bonded over the liner neck using a suitable adhesive on the open-end dome side. A metallic boss having a similar geometric profile but without an opening is also attached on the other side of liner to maintain symmetry during FW. FW of liner-boss assembly is then performed using the filament winding sequence. The Type IV COPV thus obtained is then subjected to burst test as per ISO 19881 standard [101] with increasing hydraulic media (water) pressure till $2.25 \times p_{nwp}$. During burst test, it was observed that the fabricated COPV failed much earlier than the expected failure pressure. The failure in the form of leakage of hydraulic media from the open-end boss region was observed during experiment. Based on these experimental observations, the simulation framework presented in this paper is designed to elucidate the role of manufacturing and design defects on the failure behavior of a Type IV COPV at p_b using FE analysis. The analysis presented can be used as guidelines on how failure can be prevented in expensive Type IV COPV by doing suitable design modifications.

To analyze the failure of Type IV COPV during burst test, interactive failure theory was used to predict failure sites as Tsai-Wu failure index F.I (see, Eq. 3.11). By critically investigating the failure observed during testing, it was found that the site of the hydraulic media release from the COPV is the open-end metallic boss and FW coupling (D4 defect site) which is caused by the release of hydraulic media from the valve mounting zone of the liner at first and then from the adhesive joint between the liner and the open-end metallic boss (which seems to have failed during pressurization of COPV due to expansion of the COPV) followed by the final release from the open-end metallic boss and FW coupling site. Though the coupling of liner-metallic bosses was considered to be permanent in FEA, the shape of the boss considered in experiments leads to highest stresses levels at the D4 and D5 sites on the dome part of metallic boss. Due to this, during experiment, once the adhesive bond between liner and metallic boss is opened during pressurization, the media finds the way to easily escape the COPV from the coupling of open-end metallic boss and FW.

While the experimentally observed failure can be partially explained based on FEA analysis of a defect free COPV (with D1, D2, and D3 defects removed), the following findings are also relevant for developing a failure resistant COPV:

1. The hoop layers only cover the cylindrical part and helical layers cover cylindrical as well as hemispherical dome parts. This results in more thickness in the cylindrical part and less thickness in the dome part [154]. Due to this, at the interface of cylindrical and dome parts, a stress concentration region is created leading to high

F.I observed at these defect sites. Such a defect can be removed by shifting the drop location of hoop plies from the end of the cylindrical part to the dome part just after the dome-cylindrical transition region or by using dollies at the dome-cylindrical transition region, as shown in Fig. 3.1.

- 2. The gap at the multi-material interfaces of Type IV COPV can act as a failure site. The hoop layers in the cylindrical zone appear to be undamaged due to this gap, in contrast to the helical layers in the dome region. Such a gap can be filled with matrix material of FW or a similar material (Teflon) to prevent the failure.
- 3. The role of the boss shape and its interaction with the composite analyzed in case IV and with boss shape design A1A2 were found to be unsafe. The design was found to be safe for B1B2 and C1C2 boss shapes. It was observed that the boss design parameters are an important parameter for safety and considers the number of parameters in designing (shown in Table 3.7).
- 4. After a safer design, maximum p_b capability was examined, and it was observed that the design could withstand a maximum p_b of 161 MPa and was safe for p_b of 157.5 MPa. It is observed that the design failed at p_b of 162.75 MPa. The p_b can be improved with consideration of various design modifications and manufacturing defect minimization.

3.6 Conclusion

This work proposes a design solution for Type IV COPV for H_2 storage with p_b of more than 150 MPa. The precisely calculated theoretical design parameters based FE modelling considers the possible manufacturing defects to perform failure analysis. It was found that equivalent von Mises stress and F.I shows large variation along the composite winding due to shape of liner and boss, composite geometry, and their interfaces. The findings from this work are summarized as follows:

- 1. The sharp transition at the cylinder-dome interface model exhibits the worst load-bearing capability. The ply drop location when shifted from the end of the cylindrical part to the dome part near the dome-cylindrical part transition region can help to prevent the failure at the dome-cylindrical interface region.
- 2. Even a small gap at the multi-material interfaces of Type IV COPV can act as failure site, as shown in the case III of this work. This calls for a high precision winding systems required for filament winding of Type IV COPVs to prevent any such defects during the winding process and by having such a contact between liner-metallic boss-FW such that no gaps are possible.
- 3. While the simulations are performed using non-geodesic dome as per the design of liner used in experiments, the geodesic dome is essential for transitioning the failure

from dome region (as high F.I value is observed in dome region of a defect free COPV) to cylindrical part of Type IV COPV to make it a safe design.

3. Role of Manufacturing Defects on Failure Behavior of 70 MPa Type IV COPV for $\rm H_2$ Storage

Chapter 4

Modeling of H_2 Permeation through the Liner Materials of 70 MPa Type IV COPV

4.1 Introduction

The polymeric liner in Type IV COPV, serves as a structural element during the FW process. It functions as a non-load bearing member with major role to provide a strong permeation barrier for high-pressure gaseous hydrogen (H₂). It is in direct physical contact with the H₂ and has the remarkable ability to prevent leaks [155]. Besides acting as a permeation barrier, it also protects CFRP layers and metallic bosses from direct contact with H₂. The gradual loss of H₂ from Type IV COPV can decrease safety and reliability, since, it is flammable in air and explosive at NTP in the concentration range of 4-75% and 15-59%, respectively [100].

The manufactured and finished Type IV COPV (as per ISO 11119-3) are filled with H_2 up to p_{nwp} and kept in a sealed chamber (a schematic shown in Fig. 4.1) for 500 hours at NTP/vacuum and monitored for H_2 permeation/leak. It could be measured using (a) gas chromatography (GC) based on the volumetric method, (b) weight loss or pressure sensor (manometric method), (c) thermal desorption analysis (TDA), and (d) high-pressure H_2 permeation (HPHP) setup.

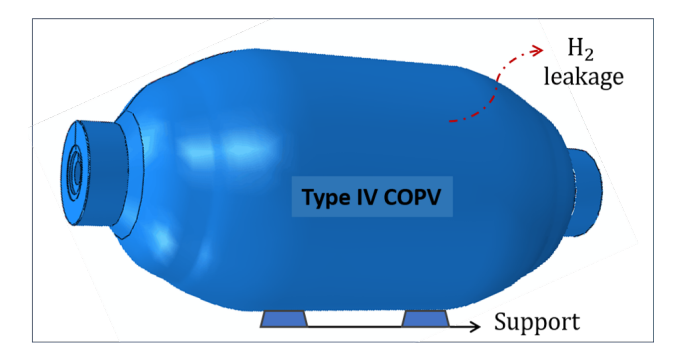


Figure 4.1: An illustration of a typical Type IV H_2 COPV kept in a sealed chamber for permeation testing.

The polymeric liner is made up of elastomers, thermoplastics, and thermosetting polymers, which can store and transport H₂ in the acceptable temperature ranges of -40°C to 85°C and pressure up to 90 MPa for several cycles in Type IV COPVs [19, 87]. These polymeric liner materials are used in various applications such as food packaging, pipes, drug delivery, beverage [125, 156], and industries exposed to chemical and cryogenic temperatures that cause failure due to leaks at critical operating conditions [157]. Polymeric liner materials such as PA6 [47, 125, 62, 158], PE [59], LLDPE [55], LDPE [55, 64], HDPE [65, 55, 60, 64, 63, 61, 57, 65, 159, 160], polyurethane (PU) [41], PET [161] etc., are combined with Type IV COPVs and performed various mechanical tests. Very few reports are available on analyzing the safety and structural integrity of polymeric liners separately [146]. Various research articles show the study of permeation on polymers such as PA6 [146, 162], PET [156, 163, 164, 165], LDPE [166, 86], HDPE [86] materials, etc., according to various low-pressure applications [167].

Most of the earlier literature worked on the non-dependence of diffusivity and solubility on the H₂ concentration in the polymer matrix. It was reported that the solubility is independent of the H₂ pressure lower than 10 MPa [168]. H₂ exposure up to 90 MPa, influences the mechanical as well as transport properties due to compression, which causes severe failures in HDPE materials [87, 169, 88]. The exposure time, depressurization rate for H₂ (10–90 MPa) affect the permeation properties of LDPE, LLDPE, MDPE, HDPE, UHMWPE (PE100 grade), and EPDM [18, 88, 83]. HDPE is a widely used common liner material for storing H₂ at pressures up to 90 MPa because of its excellent toughness, low permeability, and ease of manufacture. Thermal and mechanical cyclic loading is responsible for H₂ permeation through CFRP and polymer [170]. The effect of concentration (C), pressure (p), and temperature (T) content on sorption, diffusion, permeation, and conductivity was analyzed during the fast filling of COPV [20, 2, 81], for that aging has been studied under a H₂ environment for PA11 and PE100 [171]. The physical and mechanical properties of the polymers change at high-pressure H₂, i.e., plasticization. The pressure of gas in polymers also affects the glass transition temperature T_q of the polymer during the temperature-dependent test [87]. Operational variables (C, and p), material characteristics (crystallinity, orientation, crosslinking), thickness [168], blending variables (organic or inorganic filler, complex side chain addition) [154], transport variables (permeability coefficient: P_e , diffusion coefficient: D_{eq} , and solubility coefficient: S), manufacturing methods (roto molding, blow molding, or injection/extrusion molding [172], 3-D printing [173], ultrasonic fusion bonding), and handling and packaging procedures also influence barrier performance. Any material and design changes in these COPVs, H₂ interaction, and compatibility must be taken into account for polymer liners and CFRP wrapping, as well as changes in the static, cyclic, and fatigue strength of the material due to the presence of high-pressure H₂ [174].

Due to the small molecular size of H_2 , it gets dissolved, and its penetration is unique to the polymeric liners. H_2 penetration rates and its saturation in the liner material are

encouraged by prolonged storage and require higher barrier coefficients. A semicrystalline polymer sample has a higher diffusion of H₂ governed by the diffusion model and the sorption mode during cyclic loading [82, 84]. Henry's law dissolving in an equilibrium zone and Langmuir-type sorption in a non-equilibrium region make up the dual-mode sorption model (reflected due to excess free volume), which strongly depends on pressure [17, 175]. Gas diffusion through polymeric liner material involves complex nonlinear diffusion consisting of the governing equations such as Henry's law, Fick's 2nd law, a yield criterion, and non-linear transient diffusion based on Langmuir sorption [176]. High pressure results in an increase in H_2 concentration and a decrease in free volume (FV). It also affects the transport properties $(P_e, D_{eq}, \text{ and } S)$ of polymeric material. For high-pressure H₂ permeation testing, it takes a costly, complex assembly of the setup, significant time, prototype sample preparation, and other safety concerns [177]. However, because of the proprietary nature of the research carried out by commercial organizations, the characteristics of H₂ permeation and their behavior at high pressure are still not available in the literature. Therefore, it is important to analyze and understand the role of polymer microstructure in the H₂ multi-operational parameter-driven permeation model. To determine whether the liner specimen can maintain its H_2 barrier qualities and permeability over the COPV lifetime, H₂ permeation measurements must be taken at predetermined intervals.

In this work, the process of H_2 permeation and the barrier mechanism of polymeric liner material is analyzed by considering factors such as C, p, crystallinity, morphology, etc. that affect the transport properties of the Type IV COPV wall material. A coupled framework of H_2 transport model (HTM) has been developed for FEA using the user material's thermal (UMATHT) subroutine. A procedure for H_2 transport modeling framework is shown in Fig. 4.2.

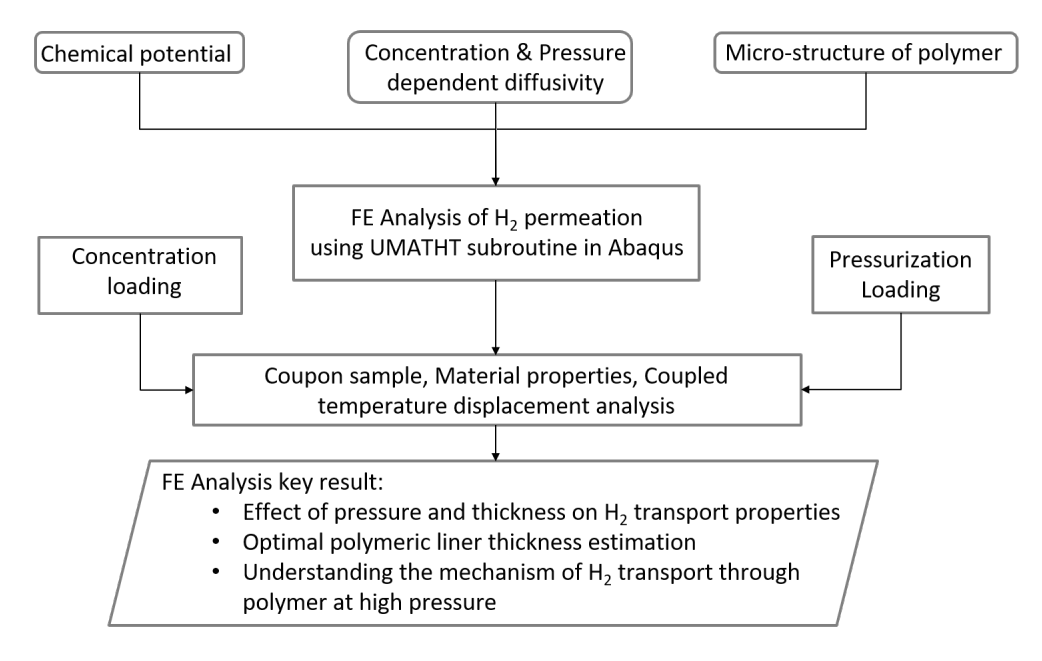


Figure 4.2: A schematic of hydrogen transport modeling framework.

The mathematical framework developed has been validated by experimental results of transport properties reported in the literature, and permeation tests are performed by pressurizing one side of the coupon with H₂ from 10 MPa to 90 MPa. The simulation framework attempts to conclude the effective H₂ transport properties through the wall of a polymeric liner to improve the structural integrity and permeation limit of 70 MPa Type IV COPVs to achieve the DoE, USA targets for the light-duty FCVs [82]. The loss can be recovered or minimized by proper maintenance of permeability and understanding the proper mechanics of permeation to achieve desired gravimetric and volumetric targets.

4.2 Mathematical Modelling to Implement in FE Analysis

To simulate the complex H_2 diffusion through a polymer at critical pressure and C, there is a need for a simplified and well-defined mathematical model to implement in commercial software like Abaqus. The UMATHT subroutine can correlate our mathematical modeling with the variables of H_2 diffusion through Abaqus. The limitations of the earlier approach ignore the effect of pressure gradient, variation in diffusivity, and crystallinity of the polymeric liner material on the permeation measurement [84].

4.2.1 Methods of permeability prediction and process of H_2 diffusion through polymeric liner material

The permeability test was performed on the disc-shaped polymeric liner coupon sample utilizing the permeation test bench (as per ISO 15105) in which the sample is placed inside the permeation cell. This high-pressure gas permeation (HPGP) cell consists of two chambers, in which H_2 is at p_{nwp} in one chamber directly exposed with the polymeric sample and the other chamber is at NTP, as shown in Fig. 4.3. The H_2 diffusing through the polymer sample was then collected in the chamber at NTP and the p or flux (J) vs time plot was used to calculate the H_2 transport properties of the polymeric liner material [178]. The TDA method is a simple non-steady state permeability measurement technique in which the H_2 permeates out from all directions after being taken out of the pressure chamber, and it is a less accurate type [18, 22]. The following processes are involved in the diffusion of H_2 through a dense polymer, according to permeation measurements that revealed a permeation coefficient:

- 1. At high penetrated C and p, the H_2 adsorbs into the polymer surface;
- 2. Penetrate molecule gets diffused through the polymer via C and p gradients;
- 3. Desorption of the penetrated molecule takes place in the atmosphere at NTP from the polymer surface.

The schematic of polymeric material, state of gaseous (H_2) (p, C), and steps involved in the diffusion through the polymer are shown in Fig. 4.3(a) and (b). In Fig. 4.3(a), the polymer material (shown in green) has thickness L, and the left side of it, named the

feed side, contains H_2 at a p, and C and right sides of polymeric material are named as permeate side exposed to atmospheric NTP. In Fig. 4.3(b) of step I, the adsorption takes place on the left side of the polymeric material (feed side: at X=0), in step II, the diffusion takes place; and in step III, that is the right side of the polymeric material (permeate side: at X=1), the desorption takes place to the permeate side.

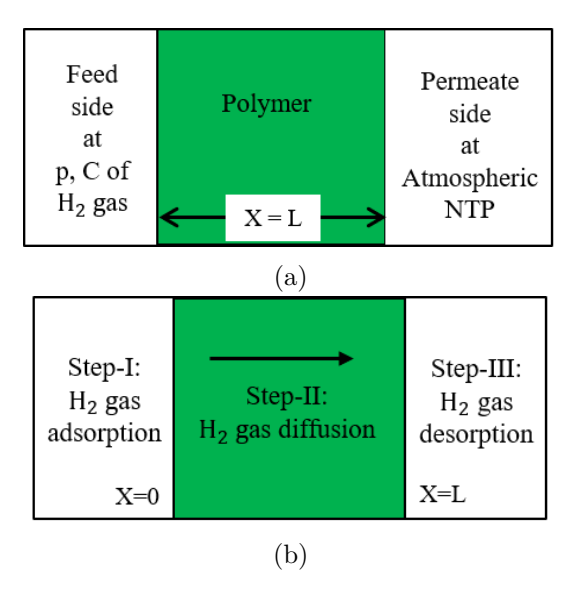


Figure 4.3: (a) H₂ interaction with the polymeric sample at a given state, (b) steps involved in the diffusion process.

4.2.2 Governing equation for H₂ diffusion in terms of chemical potential

To consider the effect of the C and p-driven diffusion model, the equivalent term used in mathematical modeling is termed "chemical potential", and it is defined as the movement of molecules from a surface area with a higher potential to a surface area with a lower potential; this process is known as diffusion. At constant temperature, the chemical potential μ (Eqn.(4.1)) and gradient of chemical potential $\nabla \mu$ (Eqn.(4.2)) are written as [179]:

$$\mu = \mu^0 + RT lnC - V_H \sigma_H \tag{4.1}$$

$$\nabla \mu = \nabla (RT \ln C) - \nabla (V_H \sigma_H) \tag{4.2}$$

where μ_0 is the standard chemical potential. Fick's first and second laws explain this diffusion process for a steady and transient state. The H₂ flux (J) vector is proportional to the rate at which the gradient of chemical potential changes, $\nabla \mu$ and the expression is written as Eqn.(4.3) [180]:

$$J = -\frac{D_{eq}C}{RT}\nabla\mu = -\frac{D_{eq}C}{RT}(\frac{\nabla C}{C}RT - V_H\nabla\sigma_H)$$
(4.3)

where D_{eq} is the diffusion coefficient for H_2 , R is the universal gas constant, J defines the number of H_2 molecules passing through a unit area per unit of time, C is the number of

moles of H_2 per unit volume, and V_H is the partial molar volume of H_2 in the polymer at room temperature T for a system for compression of the polymer by the pressure of the penetrant [161]. The extended form of Fick's second law, unsteady state, non-linear, second-order partial differential equation specifies a non-zero value for the hydrostatic stress/pressure gradient and C-induced diffusion as written in Eqn. (4.4):

$$J = -\frac{D_{eq}}{RT}(RT\nabla C - CV_H \nabla \sigma_H) = -D_{eq}\nabla C + \frac{D_{eq}CV_H}{RT}\nabla \sigma_H$$
 (4.4)

The hydrostatic stress is the average of all three normal stress components, and it causes a compression effect on the polymer. It is written as:

$$\sigma_H = \frac{1}{3} \sum_{i}^{3} \sigma_{ii} = \frac{\sigma_{11} + \sigma_{22} + \sigma_{33}}{3}$$
 (4.5)

The value of i ranges from 1 to 3 and corresponds to all three normal stress components. The analysis considered a plane stress condition $\sigma_{33}=0$ i.e., the stress generated is unaffected by out-of-plane normal and shear components. The polymer chains are compressed for the applied hydrostatic pressure, restricting their mobility. As a result, the diffusion of H_2 molecules through the polymer becomes slower. Diffusion depends on various factors, including the specific polymer, its molecular structure, crystallinity, and the nature of the gas. The unique characteristics of the polymer, such as its structure, crystallinity, and interactions with H_2 , might influence the complex relationship between V_H and compressibility. The simplified expression for V_H is written as Eqn. (4.6) [181]:

$$V_{H} = \left(\frac{\partial V}{\partial n}\right)_{T,p} = V_{s} \frac{\partial}{\partial C} \left(\frac{\Delta V}{V_{0}} + \beta_{T,p}\right) \tag{4.6}$$

where V is the volume of a polymer-gas system containing "n" moles of H_2 , V_0 is the volume of penetrant free polymer at p=0 and C=0, V_s is the volume of an ideal gas at NTP, $\Delta V=V-V_0$ is the volume of penetrant inside the polymer, $\beta_{T,p}=-\frac{\partial}{\partial p}(ln(V))_{T,n}$; compressibility of the H_2 containing polymer. Fick's second law is obtained from Fick's first law of diffusion. The mass conservation equation is written as:

$$\frac{\partial}{\partial t} \int_{V} (C)dV + \int_{S} J.ndS = 0 \tag{4.7}$$

Applying the divergence theorem, the final implementation of the H_2 transport model results:

$$\frac{\partial C}{\partial t} - \nabla \cdot (D_{eq} \nabla C) - \nabla \cdot (\frac{D_{eq} C V_H}{RT} \nabla \sigma_H) = 0$$
(4.8)

The H_2 transport governing equation model is abbreviated as Eqn. (4.8). The FE formulation for this HTM is given in Appendix I, A.1. Abaqus FE software uses mass diffusion to solve equations but doesn't currently support diffusion-stress-based coupled analysis for polymeric materials. The software explores diffusion-stress analysis based on an analogy between heat transfer and diffusion equations. For the specific form of coupled

governing equation for the H_2 in polymer, user-defined material, and variables have to be implemented using UMATHT subroutines to define coupled field variables. These field variables are calculated by the URDFIL and UVARM subroutines and shared with the UMATHT using common blocks. The auxiliary UEXTERNALDB subroutine allows for reading external files and initializing some variables used during the calculations. The internal H_2 pressure is applied to the internal polymeric surface of the COPV model.

4.2.3 Henry's law for polymer- H_2 interaction and time-lag method for transport properties estimation

There is no dissociation of H_2 molecules on the surface of the polymer during the polymer- H_2 interaction and the molecular interaction takes place at a given p, and C, as shown in Fig. 4.4.

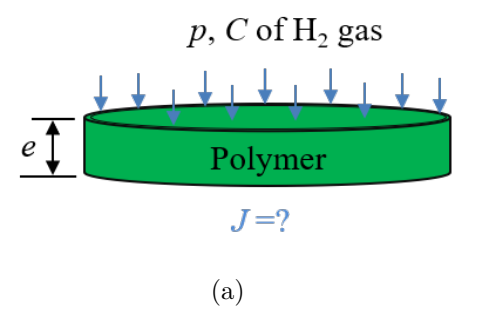


Figure 4.4: H₂ interaction with polymeric coupon sample.

The molecular interaction model takes care of the H_2 intake in the liner material using Henry's law for polymer-gas interaction, given as (Eqn. (4.9)):

$$C = S.p \tag{4.9}$$

where solubility S is the capacity of the liner material to accept solute H_2 molecules per unit volume per unit pressure. The schematic plot of J across the polymer sample with respect to time is shown in Fig. 4.5. The initial curve represents the unsaturated/transient state of the H_2 molecule inside the polymer and after the material becomes fully saturated with H_2 , it shows a steady state represented by a horizontal flat curve. The e (m) is the thickness of the sample, and t (s) is the time. The permeability P_e (mol.m.Pa⁻¹.m⁻².s⁻¹) is the rate at which gas molecules permeate through the polymer material per unit pressure per unit area for a given thickness. It is estimated using the saturation J value multiplied by sample thickness wrt pressure, as written in Eqn. (4.10):

$$P_e = \frac{J.e}{p} \tag{4.10}$$

The time lag method was used to estimate the transport properties corresponding to the saturation J reached at saturation time, t_{sat} [182]. It is the time at which the gas molecule starts reaching out of the polymer sample to permeate sideways from the feed side. It

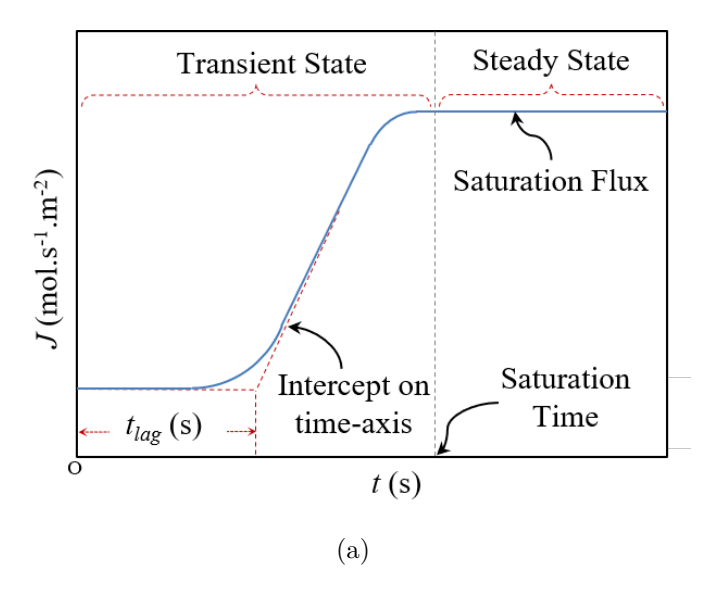


Figure 4.5: H₂ flux vs. time plot for permeation testing by the time-lag method.

includes adsorption, diffusion, and the path followed by H_2 molecules to reach out of the polymer sample or on the permeate side surface of the sample. At saturation state (t_{sat}, J) , the J value will be maximum and the change in J value is negligible (the maximum J variation is less than 1%). Most commonly, the diffusivity values are estimated using the time-lag method, corresponding to the J vs. time plot. The value of the intercept on the time axis is called time lag, t_{lag} , and estimated using Eqn. (4.11) [183]:

$$t_{lag} = \frac{e^2}{6D_{eq}} \tag{4.11}$$

The accuracy of this method has been described by analytical and FE Abaqus-based software results for J vs time [184, 185, 186]. The time lag is the characteristic time that depends on D_{eq} , e, and the inflection point [182]. There are various time lag models available for permeation analysis, as described by the Taylor series, the singular point method, the tangent method extrapolated on the time axis, and the precise equation described by the sigmoidal plot. The singular points are considered at the 0.63 times saturation J value [187]. The solubility change for H_2 molecules inside the polymer was evaluated using the relation between the P_e , D_{eq} , and S as expressed in (4.12) [177]:

$$Pe = D_{eq}.S (4.12)$$

4.2.4 Effect of concentration and pressure on diffusivity

The diffusivity is the capacity of the material to let gas flow through it. It is almost constant at NTP. But for the transition and peak loading, the diffusivity properties change from material to material [188]. The diffusivity of the H_2 gas-polymer system depends on H_2 concentration inside the material as well as p and it is expressed as Eqn. (4.13) [16, 17]:

$$D_{eg}(C, p) = D_{sc} \exp(\beta_h p + \eta C) \tag{4.13}$$

where D_{sc} is the diffusion coefficient for semi-crystalline polymeric material at atmospheric pressure and with no invasive gas content, β_h is the pressure coefficient, and η is the concentration coefficient. If these two modes are independent of one another, the constant β can be written as $\beta = \beta_h + \eta.C$. This relation follows the straight line and " β " is evaluated from the slope. The term " η " and, correspondingly, " $exp(\eta C)$ " denote an increase in the number of molecules dissolved in the polymer that results in the rise of plasticization [16, 17]. The term " $exp(\beta_h p)$ " considers the contribution of the hydrostatic pressure only on diffusion. As per the kinetic theory of penetrating gases in the solid polymer in terms of the pressure coefficient is estimated by [189] $\beta_h = \frac{V^*}{RT}$, where V^* is the activation volume, R is the universal gas constant, and T is the room temperature or the temperature of the surroundings [178, 190]. The V^* parameter related to pressure coefficient affects yield and strain rate dependency of polymeric behavior in compression [191]. As a result, we can calculate β from the extrapolated value of slope $\frac{ln(P_e)}{p}$, as shown in Fig. 4.6. The logarithmic permeability ($ln(P_e)$) is calculated from the permeability coefficients at 10 to 90 MPa, taken from the paper by Fujiwara et al. [18].

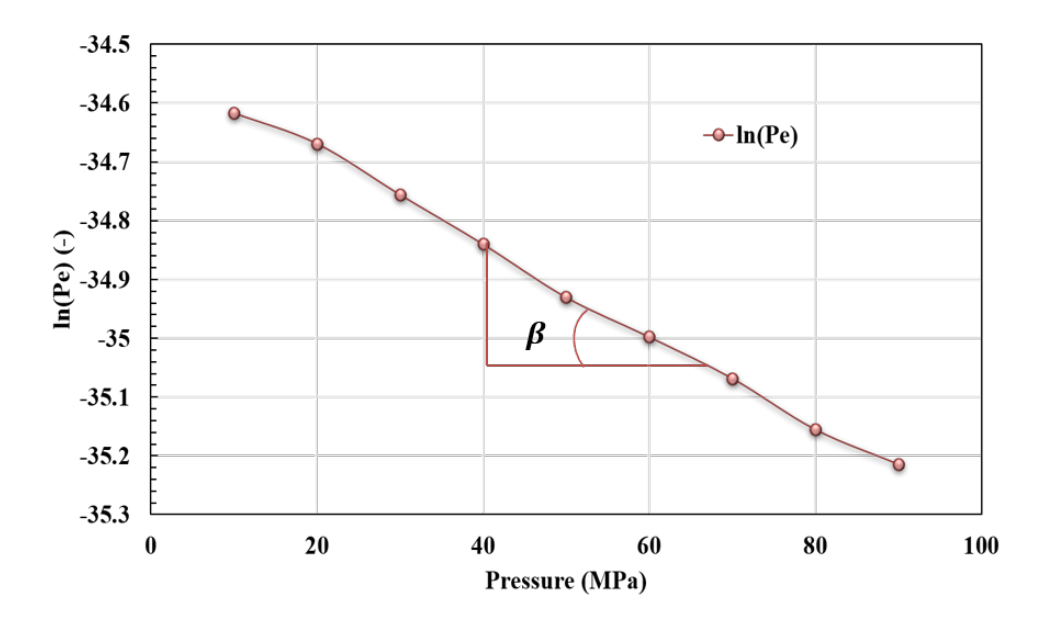


Figure 4.6: Diffusivity dependent on C and p w.r.t to its coefficient of semicrystalline polymer.

The slope of $ln(P_e)$ and hydrostatic applied pressure is almost linear from 10 to 90 MPa. This represents the behavior of the given gases for the given polymer following Henry's law. So, the variation of the slope is constant and nearly the same, with a value of $-8.0 \times 10^{-9} \text{ Pa}^{-1}$ for a given penetrating molecule in a given polymer material [17]. It was observed that an increase in applied pressure on the polymer resulted in a decrease in the permeability coefficient. Its increased compactness at high pressure results in a decrease in the FV and an increase in density [146]. The compression of the polymer

slows down the segmental motion, which in turn reduces the diffusion of H_2 through the polymer material. The morphology of semi-crystalline polymers is as shown in Fig. 4.7.

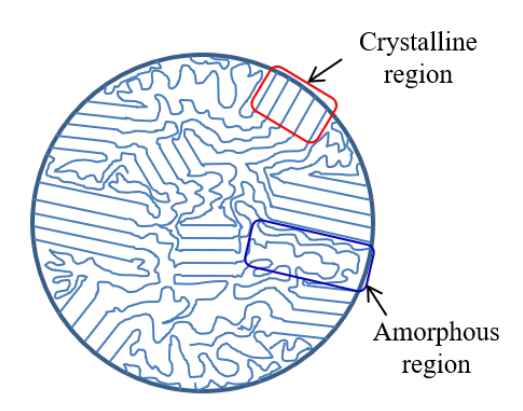


Figure 4.7: Morphology of semicrystalline polymer, consists of crystalline and amorphous region.

The p effect reverses the C effect. Segmental motion speeds up the mobility of H_2 entrance inside the polymer. Therefore, it is reasonable to assume that the molecular size of the penetrant will influence η and β_h . The few constants are estimated from the literature study of experiments (Exp.), but the literature is available for certain pressures only. The fitting of these parameters has been performed to evaluate the Exp. value due to very few published literature data available and few reports for the detailed study of high-pressure H_2 behavior inside the polymeric liner materials. Atmospheric temperature (T in K), partial molar volume $(V_H \text{ in } m^3.\text{mol}^{-1})$, hydrostatic stress coefficient $(\beta_h \text{ in } Pa^{-1})$, activation volume $(V^* \text{ in } m^3)$, universal gas constant $(R \text{ in } N.\text{m.m.mol}^{-1}.\text{K}^{-1})$, diffusivity coefficient $(D_{eq} \text{ in } m^2.\text{s}^{-1})$, and solubility $(S \text{ in } \text{mol.m}^{-3}.\text{Pa}^{-1})$ parameters for the H_2 -polymer interaction material model at the minimum reference pressure of 10 MPa is provided in Table 5.4 [16, 17, 191].

Table 4.1: H_2 transport material properties of the polymeric liner material.

Para.	T	V_H	eta_h	V^*	R	D_{eq}	S
Value	300	2.78×10^{-6}	4×10^{-8}	1.38×10^{-9}	8.314	1.35×10^{-10}	6.87×10^{-6}

4.2.5 Effect of crystallinity on diffusivity

In a polymer membrane, the Pe, D_{eq} , and S of gases often decrease with increasing crystallinity because they cannot diffuse and dissolve in the crystalline domain. As the degree of crystallinity increases, the permeability decreases [87, 161]. Due to a reduction in the volume percentage of the amorphous region, the polymer becomes more crystalline when compressed at high pressure, and it reverts to its initial condition when decompressed to low pressure [154]. Due to the shrinkage of the FV at high pressure, permeability

reduces with a drop in diffusivity [87]. The crystallinity ϕ_i of a semicrystalline polymer structure, as shown in Fig. 4.7, consists of amorphous and crystalline regions and is written as Equ. (4.14) [177]:

$$\phi_i = \frac{\rho_c(\rho_s - \rho_a)}{\rho_s(\rho_c - \rho_a)} \tag{4.14}$$

where, ρ_c is crystalline phase density, ρ_a is amorphous phase density, ρ_s is semi-crystalline density. The crystallinity parameters are shown in Table 4.2 for HDPE polymer material [16, 165, 17]. Michaels and Bixler proposed a relationship between the overall diffusivity D_{eq} and the diffusivity function of operating parameters at NTP is D_o as shown in Eqn. (4.13) and (4.15) [192].

Table 4.2: HDPE crystallinity parameters require density, crystalline, and amorphous region.

Parameters	$ ho_s$	ρ_a	$ ho_c$	ϕ_i
Units	${ m kg/m^3}$	${ m kg/m^3}$	$\rm kg/m^3$	%
Values	942	850	1000	52.62

The semi-crystalline diffusivity in terms of chain immobilization factor and tortuosity factor is expressed as (4.15) [193]:

$$D_{sc} = \frac{D_o}{\gamma \tau} = \frac{D_o}{2(1 + \tau_o \phi_i)} = \frac{D_o}{2(1 + 7.75\phi_i)}$$
(4.15)

where τ_a is a characteristic parameter and considered for the enhancement of diffusion path due to crystallinity, which is equal to 7.75, and δ is chain immobilization factor accounting for the amorphous part with $\gamma, \tau > 1$ [193, 194]. A tortuosity factor τ expresses how the penetrant molecules go around crystallites by using the amorphous component [195]. It is the measure of the maximum distance that a diffusing molecule must travel, and it is a function of the crystallinity ϕ_i [193]. For 1-D diffusion analysis, a 2-D rectangular model has been considered, in which the permeation has been allowed through the thickness direction. The crystallinity is the function of density and the density is related to volume. The volume consists of area multiplied by thickness, and the area remains the same in the analysis. Therefore, the final crystallinity of the semicrystalline polymer under high pressure directly affected by sample thickness can be expressed as Eqn. (4.16):

$$\phi_f = 100 - \left(\frac{FV_f}{FV_i}\phi_i\right) \tag{4.16}$$

where FV_i and FV_f are free volumes available in the polymer before and after pressurization, respectively.

4.3 FE Modelling Framework to Validate the Experimental Results

In this thesis work, FE simulation framework aims to study the H₂ permeation behavior of the polymeric liner material. The HDPE material was subjected to pure H₂ at a wide range of pressure and the other side was exposed to NTP, for a long duration to get saturated inside the polymer. After gas begins to diffuse from one end (feed side) to the other side (permeate side) through the sample thickness e, the rate of gas penetration reaches equilibrium, known as transmission rate or gas permeation rate. The polymer liners behavior under high pressure of H₂ inside Type IV COPVs for permeation has been analyzed. For this, HDPE material is a better choice among various liner materials studied (HDPE, LDPE, MDPE, LLDPE) in the literature [18], for the permeation behavior. The behavior of different polymer samples by Fujiwara et al. (2020) and (2021) [18, 88], under H₂ pressure up to 90 MPa with constant temperature conditions has been investigated. To validate the experimental results of available literature [18, 88], the present study aims to model the FEA framework and model validation. A transient coupled temperature displacement model is used for the analysis in Abaqus software. At first, H₂ permeation behavior through the HDPE polymer material was studied up to 90 MPa with the considerations of material properties (S, D_{eq}, ρ, ϕ) at given operational parameters (H_2) pressure and C) [82]. Secondarily, a safer value within the permeation limit for optimal thickness was evaluated for the HDPE liner of Type IV COPV for p_{nwp} 70 MPa.

A 2-D rectangular cross-section is adopted as a representative volume element (RVE) of the polymeric liner material in a Type IV COPV to streamline the FE model. This approach focuses on capturing essential through-thickness diffusion and stress behavior while avoiding curvature-related geometric complexities. The following points justify the plane strain condition for this geometry:

1. Physical representation of a long cylinder wall:

This condition matches the physical scenario of a long cylindrical vessel wall or a coupon cut from its midsection, where the middle region does not deform longitudinally but only in-plane (radial and circumferential directions). The RVE represents a small segment of the liner wall or a coupon extracted from a cylindrical vessel's midsection. In such cases, hydrostatic compression generates dominant in-plane stresses, while axial deformation remains negligible key feature replicated by the plane strain model.

2. Constrained deformation along length:

The ends in the length (z) direction are assumed to be constrained, resulting in negligible out-of-plane strain ($\epsilon_{zz}=0$, $\epsilon_{xz}=0$, $\epsilon_{yz}=0$). Aligning with the plane strain assumption. This restriction mirrors the behavior of a long cylindrical vessel, where midsection deformation occurs only in-plane, causing strains (radial ϵ_{yy} and

circumferential ϵ_{xx}).

3. Focus on in-plane stress and diffusion coupling: By eliminating out-of-plane strain effects, the model captures the dominant in-plane stresses (radial σ_{yy} and circumferential σ_{xx}) and their effect on diffusion. This is particularly important for studying hydrostatic compression and the resulting

through-thickness stress gradient in the liner material.

4. Simplified geometry with high aspect ratio:

The cross-section length (d = 16 mm) significantly exceeds the thickness (e = 1.5 mm), yielding an aspect ratio d/e > 10. This minimizes edge effects and prioritizes analysis of radial (through-thickness) diffusion and stress gradients [196].

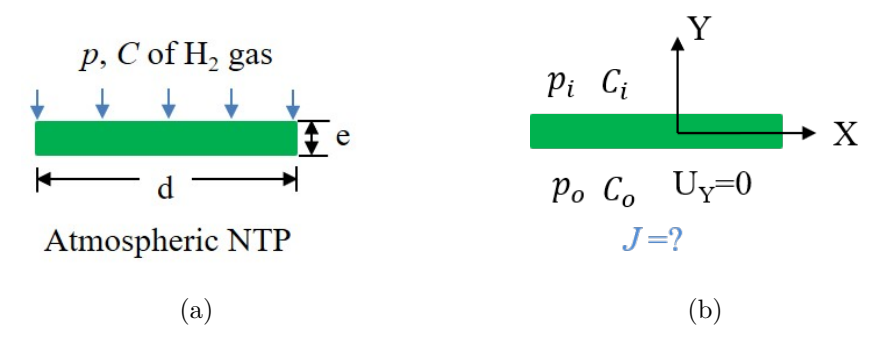


Figure 4.8: Schematic representation of rectangular coupon sample (a) geometric parameters and physical loading condition, and (b) cartesian coordinate system with boundary condition.

Load and boundary conditions applied for H_2 permeation simulations through polymeric liner samples are shown in Fig. 4.8(a) and Fig. 4.8(b). It was assumed that the diffusion through the 2-D RVE model is only in the radial direction, i.e., across the wall thickness. The diffusion through polymer is considered 1-D, i.e., unaffected by length of the sample. The applied C and p as loaded on the feed side remain constant. The assumptions considered in the FE model development are summarized:

- 1. A 3-D geometry is considered as a 2-D RVE model for 1-D diffusion;
- 2. A simple sorption model (Henry's law) is considered for H₂ interaction with polymer;
- 3. The diffusion across the edges of a 2-D sample is very low or negligible;
- 4. CFRP restricts the displacement across the radial/thickness direction;
- 5. Applied concentration on feed side remains constant.

The thickness is negligibly small compared to the length of the sample; therefore, the J at the side edges of the polymer sample is considered to be negligible. The zero displacement boundary condition (across the radial/thickness direction, i.e. $U_Y=0$) is provided on the polymer sample of the permeate side. The J variation with time to H_2 saturation is

evaluated using an extended diffusion model on the test coupon sample. The initial C inside the test sample material is zero. In the present FE analysis, H_2 captures boundary nodes at the surface of the test sample. The difference in C of H_2 , i.e., $C_O - C_t$, is caused by diffusion from one node to the next. The time increment directly affects the accuracy of results; the time starts from 0 sec to a time of 3 weeks (near 500 hours) and is chosen at a time-step Δt of 60 sec.

The selection of non-metallic polymeric liner materials is standardized by ISO 11114-5 based on H₂ compatibility. The Ogden material model is selected for the hyperelastic polymeric liner. Generalized, Ogden's strain density energy function is written as [22]:

$$W(\lambda_1, \lambda_2, \lambda_3) = \sum_{p=1}^{N} (\mu_p/\omega_p)(\lambda_1^{\omega_p} + \lambda_2^{\omega_p} + \lambda_3^{\omega_p} - 3)$$
 (4.17)

where μ_p is the constant shear moduli, ω_p is the dimensionless constant, λ_i is the principal stretches, and N is the number of terms. Material parameters $\mu_1 = 51.125$ MPa, $\omega_1 = 3.55$. The HDPE exhibits linear elastic behavior up to the yield point, and its yield strength is 24.1 MPa [88]. It shows a similar yield strength in tension and compression within the elastic range due to its thermoplastic nature.

A 4-node plane strain thermally coupled quadrilateral, temperature-displacement element CPE4T type, was chosen for the mesh for a 2-D cross-section liner material in the FE model. A linear element type was selected to minimize the computational time. In the mesh-independent study, the output does not change significantly for the 0.1 mm element size. FEA was done with the following mesh and element specifications, as shown in Table 4.3.

Table 4.3: FE mesh and element type specifications.

FE mesh model	Element type	Number of element	Number of node
2-D rectangular	CPE4T	280035	278005

4.4 Result and Discussion

The HDPE sample has been tested at various pressures for a set amount of time to reach saturation state, and the amount of H_2 that permeates through the material is then measured by saturated J. Finally, the model is used to determine whether the liner's steady-state leakage rate may reach the permeation limit by estimating the thickness. After modeling and simulating this, the H_2 transport properties are evaluated using the time-lag method.

The contour plot for H_2 concentration variation along the thickness of the test coupon sample driven by C and p at the inner surface (feed side) due to polymer-gas interaction

after a long time is shown in Fig. 4.9(a). The H_2 concentration (Conc) are 140, 284, 403, 519, 660, 787, 867, 999, and 1110 mol.m⁻³ corresponding to applied gaseous pressures of 10, 20, 30, 40, 50, 60, 70, 80, and 90 MPa as shown in Fig. 4.9 (b), (c), (d), (e), (f), (g), (h), (i) and (j) respectively. At the initial time stage, the H_2 diffusion is very slow, and after some hours H_2 starts diffusing through the barrier and goes into a saturation state. The contour for J inside the polymer is shown in Fig. 4.10. The C of H_2 corresponds to times of 6.63, 8.13, 10, 11.66, 13.03, 13.46, 14.31, 14.85, 15.5, 15.91, 16.66, 17.63, 18.26, 19.01, 20.3 minutes (min) and more than a week, as shown in Fig. 4.10 (i), (ii), (iii), (iv), (v), (vi), (vii), (viii), (ix), (x), (xi), (xii), (xiii), (xiv), (xv), and (xvi) respectively. The arrow (\rightarrow) represents the direction of movement of H_2 . The contour will look similar for all p, and the corresponding C values will differ.

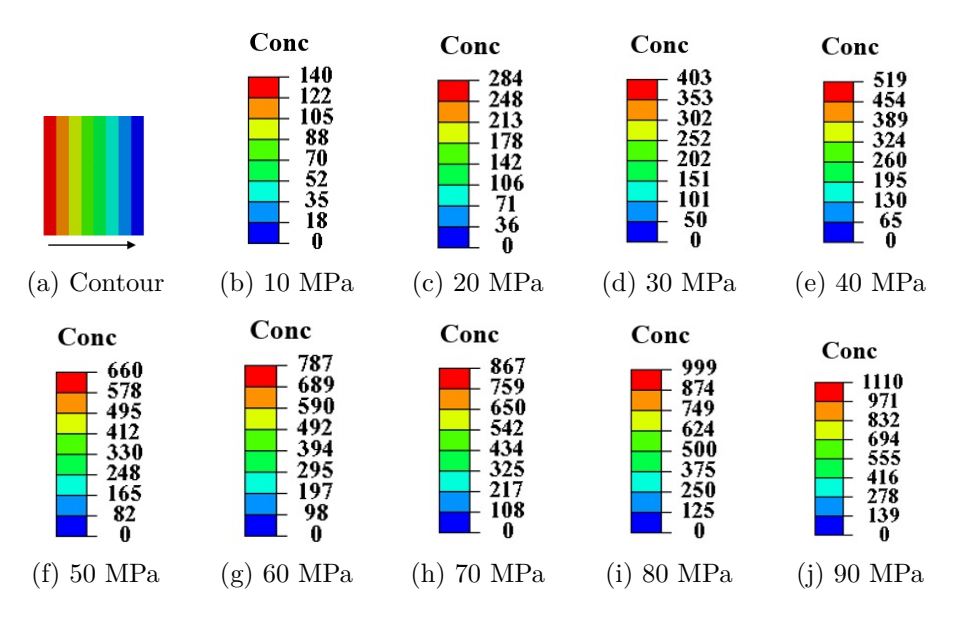


Figure 4.9: Contour for C of H_2 across the thickness of the sample, corresponding to an increase in pressure 10, 20, 30, 40, 50, 60, 70, 80, and 90 MPa.

The C of H_2 inside the polymer increases with time, and after several hours it reaches a saturation state, which means the J becomes constant with time, which is visible in Fig. 4.11 (a). This steady state J, after several hours, remains constant and is known as saturation J inside the sample. The zoomed view of an unsaturated region is shown in Fig. 4.11 (b), and the J rate increases with an increase in p and corresponding C value in the unsaturated region. An unsaturated state is also known as a transient state, in which the J changes with time. The zoomed region shows the unsaturated J, and after the 2.5×10^5 sec, the horizontal line signifies the constant J, showing the saturation of J inside the polymeric liner material. With the increase in applied pressure from 10, 20, 30, 40, 50, 60, 70, 80, and 90 MPa, the corresponding J values are 6.16×10^{-6} , 1.16×10^{-5} , 1.61×10^{-5} , 1.98×10^{-5} , 2.25×10^{-5} , 2.52×10^{-5} , 2.74×10^{-5} , 2.87×10^{-5} , and 2.96×10^{-5} mol.m⁻².s⁻¹, respectively. Using the saturation J value corresponding to the pressure applied and the thickness of the sample, the H_2 permeability was evaluated using Eqn. (4.10).

The pressure is increased from 10 MPa to 30 MPa, and the J profile and saturation time

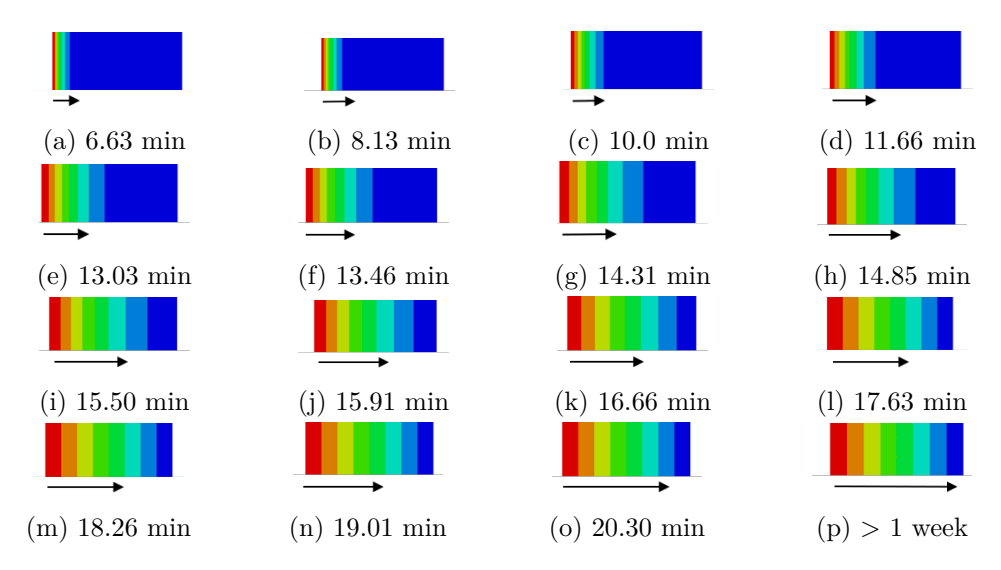


Figure 4.10: H₂ flux contour across the thickness of the sample with increases in pressure with time at 10 MPa.

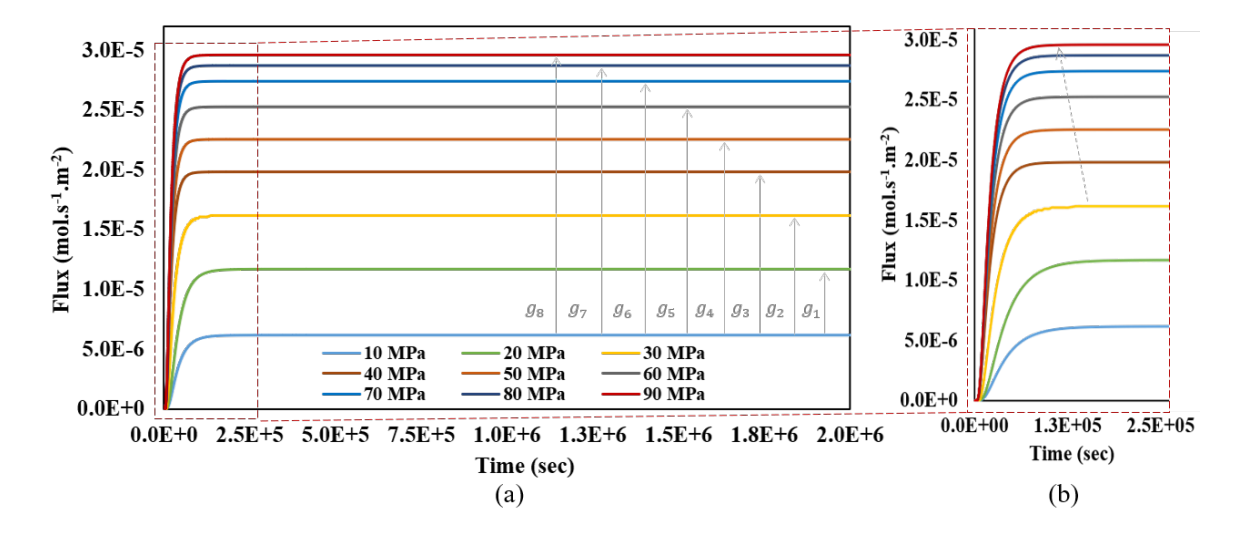


Figure 4.11: Contour for H_2 flux for various pressures (a) till saturation reached and (b) the unsteady state in zoomed view.

also increase. At 30 MPa, there is non-uniformity (shown in Fig. 4.11(b)) due to exceeding the HDPE yield strength of 24.1 MPa. It is observed that it affects the distribution of H_2 in the polymer but does not affect the saturation J value. The H_2 that occupies the amorphous region now starts to feel more compression due to an increase in applied p. This causes the fast flow of H_2 and the rate of J to increase with pressure, corresponding to the increase in pressure at and above 30 MPa. More H_2 on the feed of the polymer causes a higher rate of polymer-gas interaction, and diffusion will be faster. This shows the reduction in saturation time with an increase in J value (as shown in Fig. 4.11(b) by the left inclined arrow). The difference in saturation J value corresponding to the next-to-previous applied pressure is decreasing. The saturation J increased, corresponding to an increase in pressure (shown by an upward arrow "↑" in Fig. 4.11 (a)) as compared to an initial applied pressure of 10 MPa. The difference in the saturation J value is

 0.55×10^{-5} , 1.0×10^{-5} , 1.36×10^{-5} , 1.63×10^{-5} , 1.91×10^{-5} , 2.12×10^{-5} , 2.25×10^{-5} , and 2.34×10^{-5} mol.m⁻².s⁻¹ (for the gap $g_7 > g_6 > g_5 > g_4 > g_3 > g_2 > g_1$) corresponding to an increase in applied pressure of 20, 30, 40, 50, 60, 70, 80 and 90 MPa, respectively, to the reference J value of 6.16×10^{-5} mol.m⁻².s⁻¹ for 10 MPa. The relative changes are 0.89, 1.62, 2.47, 2.65, 3.46, 3.84, 4.08, and 4.24, corresponding to the applied pressure 20, 30, 40, 50, 60, 70, 80, and 90 MPa, respectively, to the reference pressure of 10 MPa. Fig. 4.12 shows the variation of permeability of HDPE material with the applied pressure at a constant temperature. The model was able to fit the points of the FEA and the Exp. values that are reproduced from the Fujiwara et al. 2020, and 2021 papers. The dependence of permeability with applied pressure can be easily understood using the expressions shown in Eqn. (4.10).

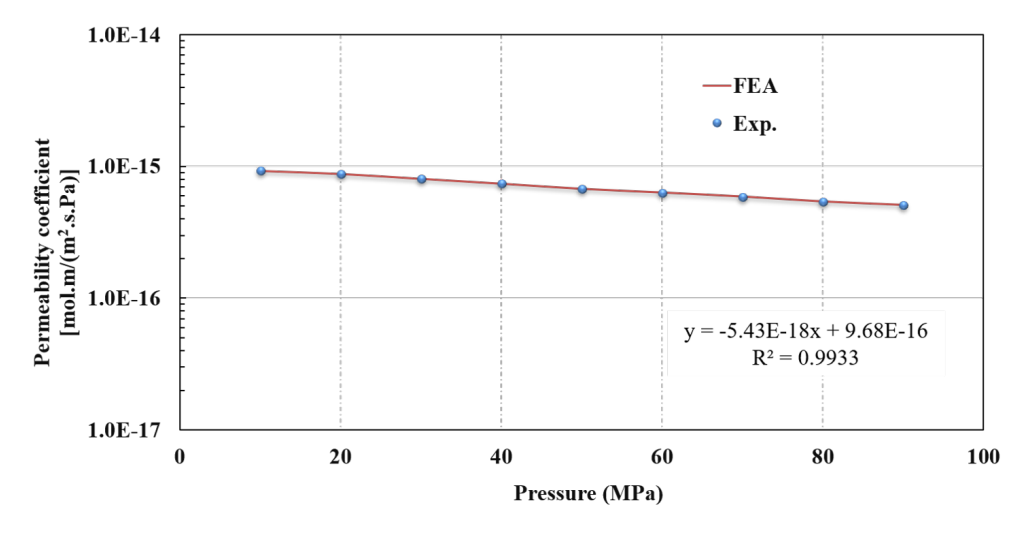


Figure 4.12: Permeability variation with an increase in H₂ pressure for HDPE.

It was observed that the permeability decreased with an increase in pressure due to an increase in the crystallinity of HDPE. The polymer chains get compact due to the increase in density due to decrease in thickness, which means there is a reduction in the FV, increasing crystallinity. The diffusivity value was evaluated using Eqn. (4.11) for a given sample thickness and time-lag value utilizing the J plot as shown in Fig. 4.11 (corresponding to an intercept on the time-axis as shown in Fig. 4.5(b)). The diffusivity variation with the applied pressure is shown in the Fig. 4.13. The solubility was evaluated using the relation between P_e , and S using the Eqn. (4.12). The variation of the solubility coefficient with an increase in pressure for HDPE is shown in Fig. 4.14.

The permeability coefficient was observed to be an important parameter for H_2 permeation study through the polymer. Since it is directly related to saturated J value, the J value can capture the C, p, e, and ϕ (Eqn. (4.10), (4.2), and (4.13)). The diffusivity coefficient is evaluated using the unsaturated J plot and time-lag method (as shown in Eqn. (4.11)), which is an approximate type of analysis and therefore the diffusivity coefficient is less important as compared to the permeability coefficient. The solubility is independent

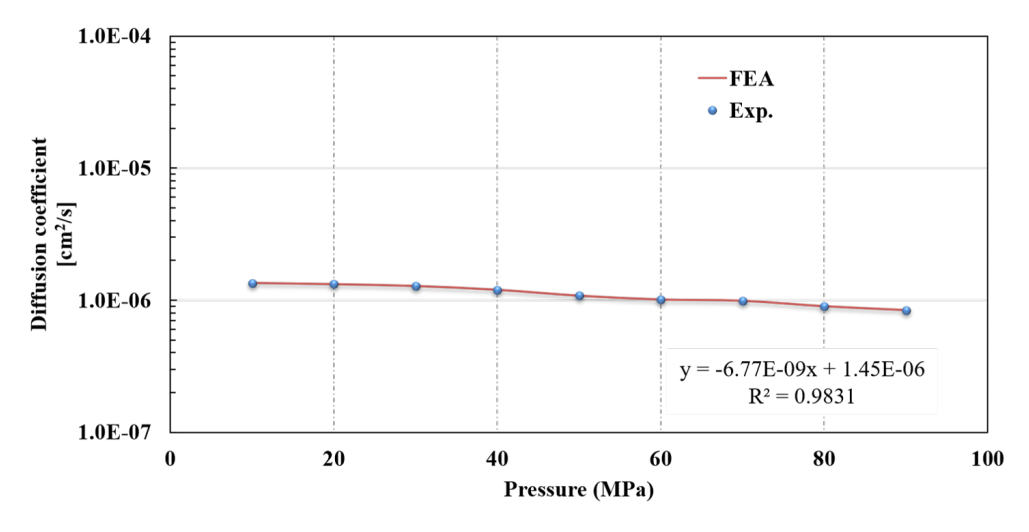


Figure 4.13: Diffusivity variation with pressure for HDPE polymer sample.

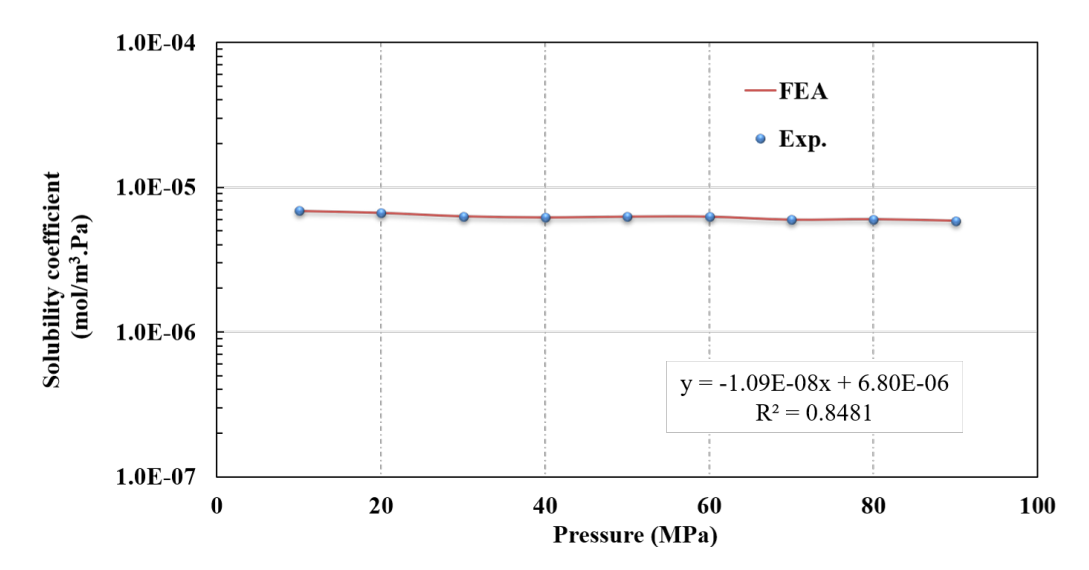


Figure 4.14: Solubility coefficient variation with pressure for HDPE polymer sample.

of J (either saturated or unsaturated), C, p, and ϕ parameters, and it is a function of permeability and diffusivity coefficients only. In general, solubility is the material property and it is nearly constant. In this case, the solubility variation is very low and almost constant, but the solubility decreases with an increase in pressure. This signifies that at extremely high pressure, a minimal alteration in the properties of HDPE material will impede the solubility of H_2 . So, solubility is the least essential parameter to consider for the H_2 permeation analysis through the polymer material (and can be easily understood by Eqn. (4.12)) and it was observed that it gives less accuracy.

Fig. 4.15 shows the variation of crystallinity with pressure. The hyperelastic nature of HDPE thermoplastic polymer shows a non-linear type of reduction of thickness with an increase in applied pressure. The reduction in free volume after pressurization, and the increase in crystallinity have been observed. This corresponding increase in pressure on the sample results in a decrease in sample thickness and an increase in crystallinity (evaluated using Eqn. (4.16)) from the initial crystallinity value of 52.62%.

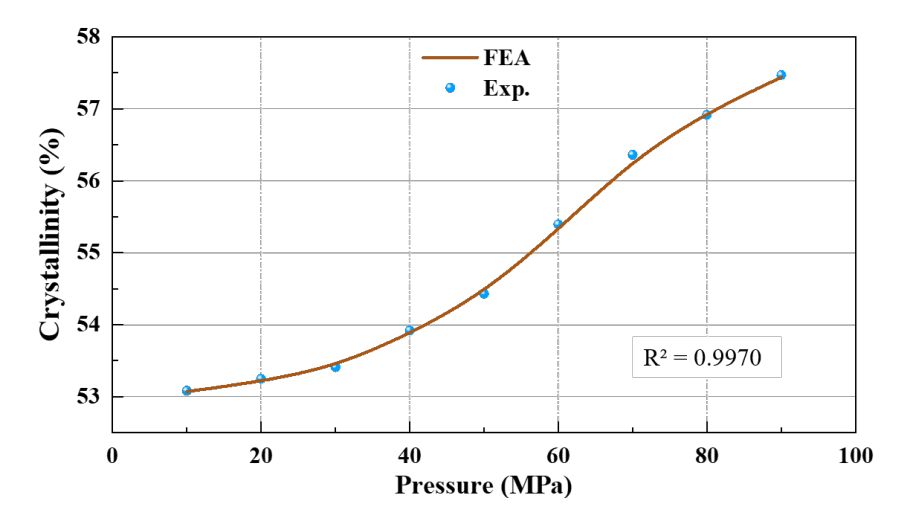


Figure 4.15: Variation of pressure affecting the crystallinity of polymer sample...

The actual thickness of the sample at atmospheric pressure is 1.5 mm, and it decreases to 1.34, 1.33, 1.32, 1.31, 1.29, 1.27, 1.24, 1.22, and 1.21 mm corresponding to an increase in pressure 10, 20, 30, 40, 50, 60, 70, 80, and 90 MPa respectively. This is due to the semi-crystalline nature and free volume available inside the polymer sample. The decrease in thickness of polymeric liner material is allowable due to H_2 gas pressure, as per ISO 11114-5. The Exp. output $(P_e, D, \text{ and } S)$ values are available for all the pressures, but crystallinity values are available with an interval of 20 MPa. Therefore, crystallinity values at the other pressure are taken by averaging the previous to the next value and only two decimal places are considered.

The FEA values are considered for two decimal places for most of the parameters that are not directly or significantly affected. The FEA analysis was performed, and the results were compared with the Exp. data reported in the published paper of Fujiwara et al. 2020, 2021. The H₂ transport parameters (Para.) at the various applied pressures for HDPE material for Exp. and FE simulation specifications are shown in Table 4.4. The unit used for pressure (p) is MPa, permeability (P_e) is mol.m.Pa⁻¹.m⁻².s⁻¹, diffusivity (D) is cm².s⁻¹, solubility (S) is mol.Pa⁻¹.m⁻³ and crystallinity (ϕ) is %. The difference between the Exp. and FEA for permeability, diffusivity, solubility, and degree of crystallinity is nearly 0.01 for each pressure and the error is less than 1 %. In the r-square (r^2) regression fit value lies between 0 and 1 [186]. Using the linear fit, the r^2 values for permeability, diffusivity, and solubility, are 0.9933, 0.9831, and 0.8481 respectively. For the crystallinity variation, the r^2 value is 0.9970 using the nonlinear regression fit with a logistic function. This shows that the regression value is closer to 1, which shows linear variation. The developed permeation FEA model matches the results of Exp. with accuracy.

The current thickness of the HDPE sample is 1.5 mm and has been analyzed for H_2 transport behavior up to 90 MPa, but this thickness is not sufficient to satisfy the criteria of a permeation barrier for 70 MPa p_{nwp} Type IV COPVs. So, to satisfy the safety criteria

Table 4.4:	Experimental	data	and	FEA	${\rm simulation}$	study	parameters	for	the	various
pressures.										

Para.	P_e (×	10^{-16})	D (×	10^{-6})	S (×	10^{-6})	ϕ ((%)
р	Exp.	FEA	Exp.	FEA	Exp.	FEA	Exp.	FEA
10	9.25	9.24	1.35	1.34	6.87	6.89	53.08	53.07
20	8.78	8.76	1.31	1.33	6.65	6.58	53.24	53.21
30	8.05	8.08	1.28	1.27	6.28	6.36	53.41	53.42
40	7.40	7.43	1.20	1.19	6.17	6.24	53.92	53.87
50	6.76	6.76	1.08	1.09	6.25	6.20	54.43	54.44
60	6.32	6.31	1.01	1.02	6.25	6.18	55.39	55.32
70	5.88	5.87	0.99	0.95	5.96	6.17	56.36	56.30
80	5.40	5.38	0.90	0.91	6.0	5.91	56.91	56.95
90	5.08	4.98	0.84	0.83	5.57	5.53	57.47	57.44

of H_2 permeation barrier limit as per DoE USA targets, there is a need for more thickness of the sample. Therefore, by keeping all parameters, thickness of the polymeric liner material is increased. The increase in thickness variation as 1.5 mm, 3 mm, and 5 mm results in a reduction of permeability values as 5.87×10^{-16} , 4.60×10^{-16} , and 1.97×10^{-16} mol.m.Pa⁻¹.m⁻².s⁻¹ respectively as shown in Fig. 4.16.

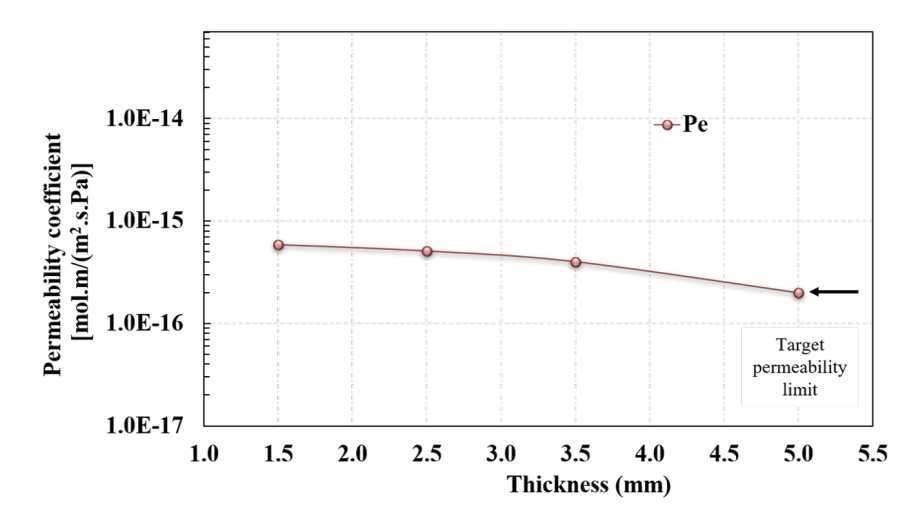


Figure 4.16: Permeability coefficient variation with thickness at p_{nwp} of 70 MPa.

The permeability values decreased with the increase in thickness due to more time taken by the H₂ molecule to reach to permeate side of the polymer sample. The compression effect at 70 MPa of applied pressure, the density increases due to the compactness of the polymer. The effective diffusivity coefficient with a variation of sample thickness is shown in Fig. 4.17. It is observed that the increase in the thickness of the polymer sample resulted in a sufficient, significant reduction in permeability and diffusion coefficient. The 5 mm thickness of HDPE finds a suitable material for the liner to build a 70 MPa Type IV COPV material. The maximum value of thickness is recommended up to 6 mm and the permeation test coupon sample should be of the same thickness of liner as per ISO 11114-5 to resist the H₂ permeation through the polymeric liner material.

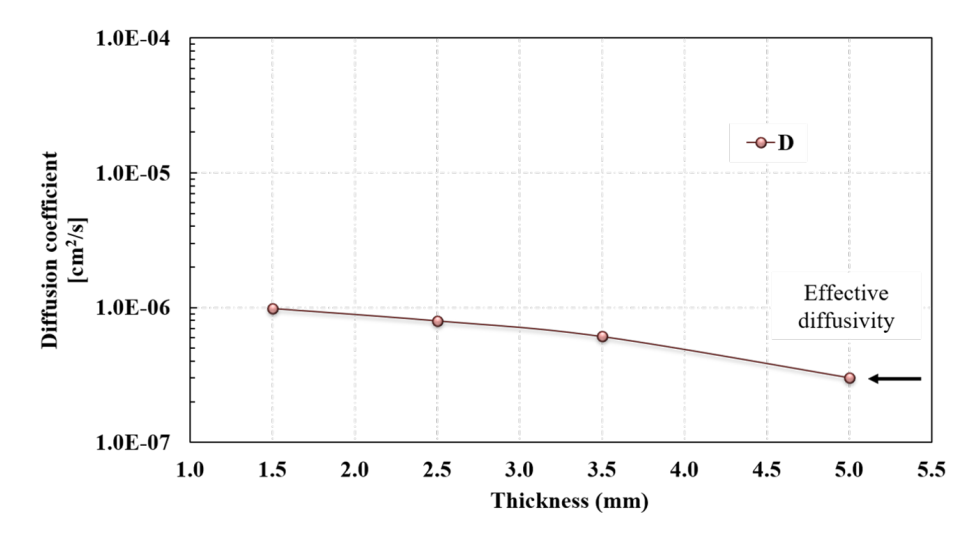


Figure 4.17: Diffusivity coefficient variation with thickness of the sample, at p_{nwp} of 70 MPa.

4.5 Conclusion

The developed HTM is utilized in the FE simulation framework with the consideration of gradient of C and p-driven H_2 diffusion at a constant temperature. The variation in diffusion coefficient was implemented in the model based on the operating conditions and the morphology of the polymer material for H_2 storage at 70 MPa p_{nwp} in Type IV COPV. The material properties and structural characteristics were implemented from the experimental data of Fujiwara et al. 2020, 2021, which showed a good H₂ permeation barrier performance for HDPE. It was observed that permeability decreases with an increase in pressure from 10 to 90 MPa for a given thickness of 1.5 mm for the polymeric liner material. The permeability shows a linear variation for an increase in pressure, with an accuracy of 99.33% for linear fitting. The model also captured the variation of crystallinity with an increase in pressure due to the reduction in the free volume present in the HDPE material due to compression at high pressure. The results of Exp. data validated by the developed FE analysis model and the percentage error was less than 1%. The permeability for 1.5 mm thickness is 5.87×10^{-16} mol.m.Pa⁻¹.m⁻².s⁻¹ at 70 MPa of applied pressure and the required permeability value as per the DoE target for the 70 p_{nwp} for Type IV COPV material is 3.32×10^{-16} mol.m.Pa⁻¹.m⁻².s⁻¹ (0.05 (g/hr)/kg). Therefore, the thickness variation was performed for 70 MPa p_{nwp} by keeping all the parameters that show the permeability limit within a safer limit, which is 1.97×10^{-16} mol.m.Pa⁻¹.m⁻².s⁻¹ for the optimal thickness of 5 mm for polymeric liner material. The H₂ takes a longer time to diffuse and to cross the higher thickness, which achieves the desired limit. So, the developed model gives a FE framework to simulate H₂ transport behavior to understand the H₂-polymer interaction mechanism for the selection of suitable liner material from the commercially available or newly developed material grade for Type IV COPV storage material.

Chapter 5

Role of Micro-Defects on Blistering Behavior in 70 MPa Type IV COPV due to H_2 Permeation

5.1 Introduction

H₂ storage poses a challenge due to its very small molecular size, allowing it to permeate through most materials easily and degrade their properties at critical operations [2, 92, 197]. Polymeric liner material provides exceptional H₂ leak prevention potential for 70 MPa Type IV COPVs [155]. During the manufacturing of polymeric liners using rotational molding, approximately 40% of the processing time is dedicated to removing macro- and micro-defects (air bubbles, voids, cavity, pore, and inclusions). There are air particles trapped in the melted polymer when the powdered polymer melts. To eliminate such defects, the mold is rotated biaxially, densification is performed, and curing is achieved by maintaining the mold at an elevated temperature [118, 198]. Large defects require more time to remove, limiting the range of plastic materials used in rotational molding [199, 200]. Still, the micro-defects remain in the polymeric liner material. The other manufacturing processes (blow molding, extrusion, injection) also consist of micro-defects that influence barrier performance and concern for safety at high pressure in Type IV COPVs [201]. In addition, studies have demonstrated that H_2 diffusion primarily occurs within the FV by hopping mechanism [202], which can be likened to the small holes between the polymer molecular chains [203, 177]. Due to manufacturing defects and a high cyclic loading rate, the polymeric liners experience stress, which may cumulatively reduce their durability and increase their susceptibility to micro-cracking.

Therefore, after p_b qualification and ensuring that the H_2 permeability is within the limit at p_{nwp} for the optimal thickness of liner material, the defilling test needs to be performed to check the effect of decompression to ensure the safety of Type IV COPV. High-pressure H_2 molecules can accumulate through the diffusion process, generating internal stresses in polymer liners and causing microscopic cavitation and macroscopic buckling. Pre-existing cavities contribute to liner-composite interface failures, such as debonding. Parametric analysis was performed for depressurization-induced blistering for liner materials (HDPE and PA) having thicknesses of 1, 2, 3, and 4 mm for the defilling rates of 1, 3, 5, and 13 hrs. 1 mm thickness showed an optimum value for all defilling rates to avoid blistering, but the

liner thickness requirement is more [20, 81]. The depressurization was performed at 0.004 to 5 MPa/min after 1 week saturation period from a pressure of 35 MPa to 17.5 MPa to analyze the blister formation at the liner-composite interface [2]. Depressurization rates ranging from 0.007 MPa/min to 0.7 MPa/min were investigated for a Type IV COPV with a polymeric liner thickness-to-external diameter ratio of 0.019 [2]. The volumetric capacity could be increased by reducing the empty p from 2 MPa to 0.3 MPa [169]. Depressurizing from p_{max} to ambient p_{min} can cause failures, which can result in crack initiation, growth, component failure, and full breakage. Controlling transport properties is crucial for preventing blister fractures and other types of H₂-induced damage, such as aging due to swelling, liner collapse, and more (as shown in Fig. 1.3) [19, 87]. Polymeric liners can be post-processed directly or indirectly to enhance their H₂ leak prevention capabilities, like fluorination (by surface mechanism) due to non-polar behavior of H₂ relative to HDPE material and others [204]. However, no specific standard is currently available for defect detection present inside the liner material and its role during H₂ permeation [155]. Therefore, it is essential to investigate the effect of H₂ permeation on the micro-defects, inclusion size, and location for the dynamic loading.

The regulations and codes that are currently in place for the design and testing of Type IV COPVs for H₂ storage do not specifically address the impact of micro-defects on H₂ permeation following polymeric lining manufacturing (ISO 11119-3). In the reported research work, the limitations of the earlier approach ignored the effect of the C and p gradient simultaneously that influence the H₂ transport properties during operations [84]. Therefore, in this thesis work, the improvement in liner technology utilized a developed HTM material model to investigate H₂ accumulation and the stress generated inside the defect. Utilizing the FE Abaqus tool, H₂ diffusion through Type IV COPV's RVE has been examined in this regard, taking into account complex nonlinear diffusion made up of the governing equations of Henry's law, Fick's second law, transient diffusion, and a hyperelastic behavior of liner material [176, 205].

5.2 Mathematical Model Used for the Analysis

Given the importance of polymeric liners towards the operational requirements of Type IV COPV, the role of pre-existing micro-defects present inside the polymeric liner and at the interface of polymer-composite on the failure behavior of Type IV COPV for a given H₂ filling cycle is simulated using FE simulation in this part of the thesis.

To simulate H_2 diffusion through a polymer at critical C and p, a well-defined mathematical model was developed in Chapter 4 and utilized in Chapter 5. The subroutine UMATHT can correlate our mathematical modeling with the variables of H_2 diffusion through the Abaqus interface.

5.2.1 Effect of hydrogen concentration on pressure buildup inside the defect

The H₂ accumulated inside the defect increases the p, generating stress. The stress (σ_c) and strain (ϵ_c) as a function of C of H₂ are expressed as [83]:

$$\sigma_c = E\epsilon_c \tag{5.1}$$

$$\epsilon_c = \zeta \Delta C \tag{5.2}$$

where ζ is the coefficient of C expansion and ΔC is the change in C inside the material.

5.2.2 Effect of pore pressure inside the defect

The safety and reliability of Type IV COPVs are crucial due to the occurrence of decompression damage and are influenced by the operating parameters. The p of H_2 in pre-existing defects may lead to the initiation and propagation of cracks. The effect of the decompression rate on preexisting defects that cause the development of p inside the defect is expressed as [20]:

$$p_{d,D} = \frac{C_i}{S} - p_i \tag{5.3}$$

where $p_{d,D}$ is p inside the defect, S is solubility of the liner material, and C_i is applied concentration. When the $p_{d,Y}$ exceeds $\frac{2}{3}\sigma_y$, blistering happens, and the relation is expressed as [85]:

$$p_{d,Y} = \frac{2}{3}\sigma_y \tag{5.4}$$

where σ_y is the yield strength of the polymeric liner material.

5.3 FE Modeling Framework

The presence of defects in polymeric liner material and liner-composite interface causes early failures due to the phenomenon of pressurization-depressurization. In this thesis work, a FE simulation framework aims to study the role of defects in the failure behavior of 70 MPa Type IV COPVs. A computational model for H_2 transport in COPV materials is implemented in Abaqus using UMATHT to model their failure behavior. The polymeric liner was subjected to direct contact with H_2 and the other side of RVE of Type IV COPV has been exposed to NTP, for a long duration to get H_2 saturation inside the polymer. After H_2 begins to diffuse through the sample from one end to the other, its penetration rate reaches equilibrium, known as the transmission rate or permeation rate, which is measured over the saturation time. The appropriate material properties, loads, and boundary conditions are defined to analyze the coupled transient temperature displacement analysis. The effect of material specifics at given operational parameters (C and p of H_2) on permeation behavior is studied up to 70 MPa [82]. The subsurface defect

lies inside and the near-surface defect lies on the surface of the liner material, respectively, as per ISO 11114-5:2022. Here, the sub-surface defect inside the polymeric liner material and a defect at the interface of liner-composite material are considered as case I, and case II, respectively. A damage-predictive model has been considered to estimate the blistering. This can reduce the number of physical tests and minimize the cost and time for Type IV design and testing. The assumptions considered in the model development are described:

- 1. A 3-D geometry is considered as 2-D RVE model for diffusion across the thickness;
- 2. A fixed type interaction between liner and CFRP considered;
- 3. The diffusion across the edges of 2-D model are very less or negligible;
- 4. The individual layer orientation effect is neglected.

5.3.1 Pressurization-depressurization cycle of hydrogen for Type IV COPVs

Filling is carried out up to maximum pressure (p_{max}) of 70 MPa in 5 minutes and maintained for several hours, then fast defilling is carried out to a p_{min} of 2 MPa at a constant temperature of 23 °C in Type IV COPVs [206]. To test the permeation rate of Type IV COPVs for more than 1 week, it remains at the same p_{nwp} to get H₂ saturation inside the wall [2, 81]. The linear depressurization rate is followed and evaluated from p_{max} , p_{min} , and the time of desorption (t_{deso}) [207]. The sample could be depressurized after saturation or a steady state is reached, as per ISO 1114-2:2022. Then defilling was performed at a maximum rate of 0.7 MPa/min from p_{nwp} to p_{min} within 1.63 hr [20, 2]. The p_{min} inside the Type IV COPVs remains at 2 MPa to avoid failure at the liner-composite interface [2]. In this thesis work, our purpose is to estimate the H₂ accumulation behavior inside the defect for the first cycle. The time instance of analysis is shown (in Fig. 5.1) by star mark "*" for the start of filling as A, just before reaching 70 MPa as B, start-between-end of saturation as C, D, E, F respectively, just during the start of depressurization as G, and at the end of depressurization-dwelling as H.

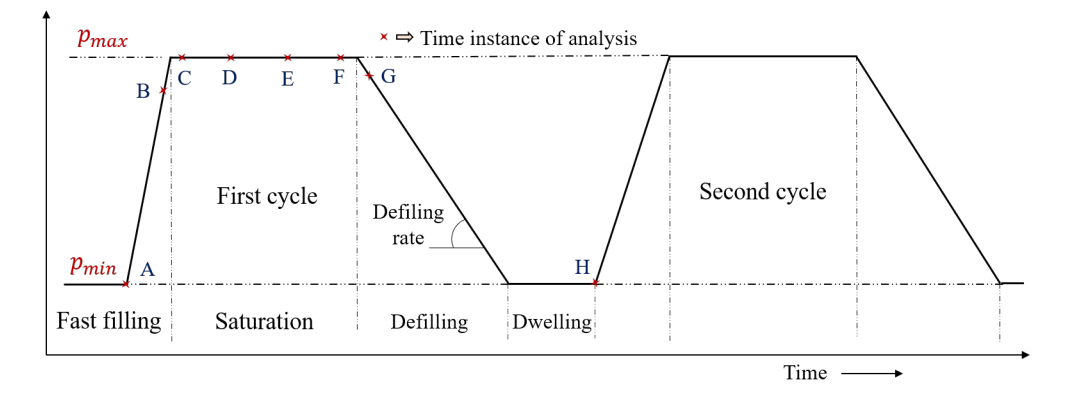


Figure 5.1: Typical pressurization-depressurization cycle of H₂ for Type IV COPVs.

The time instants are 1 s, 2.80 minutes, 9.16 minutes, 1.85 hr, 36 hr, 144 hr, 145 hr, 145 hr, and 217 hr respectively, corresponding to the filling-defiling process marked as A, B, C, D, E, F, G, and H respectively.

5.3.2 Geometrical coupon sample with loading and boundary conditions

To explore the mechanism of H₂ permeation, two micro-defects in the polymeric liner material are considered. Case I considers a circular defect at the middle of the polymeric liner, as shown in Fig. 5.2, and case II considers a semicircular defect at the liner-composite interface, as shown in Fig. 5.3. A quarter model of the cross-section of the cylindrical part of the Type IV COPV with both the defects incorporated is then subjected to an operational filling and defilling cycle.

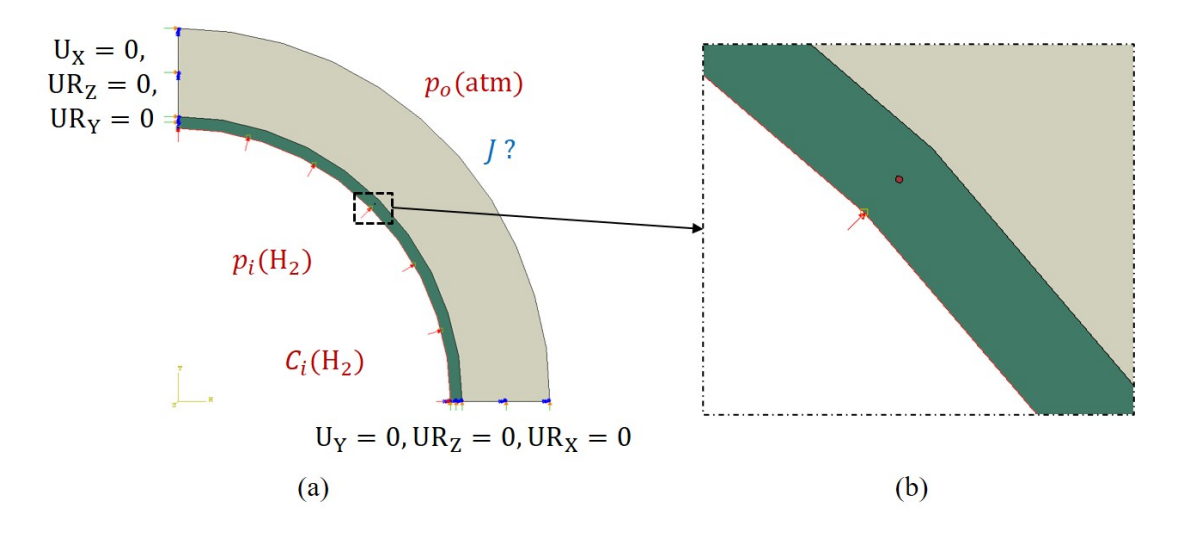


Figure 5.2: Schematic representation of (a) geometry, loading and boundary conditions, and (b) location of defect in polymeric liner material.

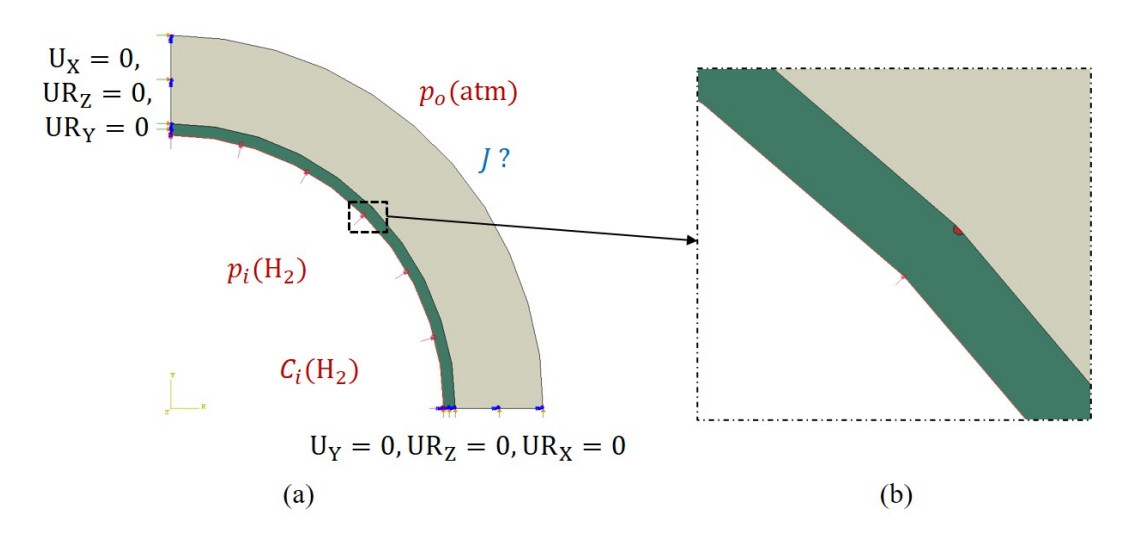


Figure 5.3: Schematic representation of (a) geometry, loading and boundary conditions, and (b) location of defect at liner-composite interface.

This model assumes that diffusion occurs in the radial direction across the wall thickness according to the loading and boundary conditions applied to the 2-D RVE model. On the innermost surface of the polymeric liner material, the loading conditions C_i and p_i were applied. The bottom and top surfaces are fixed in Y-direction ($U_Y = 0$, $UR_Z = 0$, $UR_X = 0$) and X-direction ($U_X = 0$, $UR_Z = 0$, $UR_Y = 0$), respectively. The initial concentration (C_O) within the RVE sample material is zero. In FE analysis, H_2 captures boundary nodes at the surface of the RVE sample. The difference in C of H_2 is $C_O - C_t$, caused by diffusion from one node to the next.

The circular defect size is 0.2 mm in diameter for case I and 0.1 mm for case II (less than 1 mm to be considered a micro defect) [208]. The other geometric parameters used in the FE model, are shown in Table 5.1

Parameters	Symbol	Liner	Defect	Composite	Units
Thickness	e	5	0.2 (diameter)	38.08	mm
Inner and outer radius	R_i, R_o	116, 121	-	121, 159	mm

Table 5.1: Geometrical parameters used in the FE model.

5.3.3 Mesh and element type used for modeling COPV material and defect

For H_2 diffusion, a 4-node plane strain thermally coupled quadrilateral, bilinear temperature-displacement element type, CPE4T, has been chosen for the meshing of CFRP material. A linear element type was chosen to minimize the computational time. A 4-node and 8-node plane strain thermally coupled quadrilateral, bilinear displacement, and temperature, hybrid, constant pressure element types CPE4HT and CPEH8T have been chosen for the meshing of liner material with defect at the center and defect at the liner-composite interface, respectively. This element type is useful for simulating phenomena like C-driven expansion or contraction of fluids in porous media, which can affect pore p. The type of element, number of elements, and number of nodes used for the polymeric liner, CFRP, and defect material are shown in Table 5.2.

Parameters	Liner (case I)	Liner (case II)	CFRP (case I)	CFRP (case II)
Element type	CPE4HT	CPEH8T	CPE4T	CPE4T
Number of element	5292	2000	100	216
Number of node	5521	2331	130	259

Table 5.2: FE model parameters used in mesh model.

The mesh-independent study plays a vital role in estimating the closer value in FE analysis. Here, we conducted the test for various mesh sizes in the range of 0.5-0.1 mm with an interval of 0.1 mm for the FE model. The model showed the mesh insensitiveness for the mesh size of 0.1 mm.

5.3.4 Material model used for polymeric liner, composite material, and defect

The polymeric liner material and the defect material are modeled as hyperelastic material, and the properties are shown in Table 5.3 [16, 17, 191]. The third-order Ogden model incorporates multiple strain energy terms to capture extreme deformations (expansion-contraction) and compressibility of pores or defects (behaves like soft materials). It enables better fitting of the nonlinear stress-strain behavior and softening/stiffening effects in hyperelastic materials [209], [210].

Ogden model	Symbol	Liner	Defect	Units
Order	N	1	3	-
Material constant	μ_i	51.125	-0.165, 0.289, 0.346	MPa
Material constant	ω_i	3.25	6.135, 20.13, 5.27	-

Table 5.3: Material model parameters used for polymeric liner, and defect.

The mechanical properties of the composite material are taken from Table 3.4. All composite layups are considered to have a single orientation, and the orientation effect on H_2 permeation is not incorporated. The H_2 transport properties of HDPE polymer are taken from the experimental study performed by Fujiwara et al. (2020) and (2021) [18] and [88] under p up to 70 MPa with constant temperature conditions. The atmospheric temperature (T) is 300 K, initial concentration (C_O) is zero, and universal gas constant (R) is 8.134 J.mol⁻¹.K⁻¹ for all materials. The initial diffusivity (D_O) , solubility (S), and partial molar volume (V_H) specifications used for polymeric liner, defect, and composite material used in FE modeling are shown in Table 5.4 [16, 17, 191].

Parameters	Liner	Defect	Composite	Units
D_o	9.9×10^{-11}	9.9×10^{-9}	9.9×10^{-9}	$\mathrm{m}^2.\mathrm{s}^{-1}$
S	5.96×10^{-6}	5.96×10^{-4}	-	$\mathrm{mol.m^{-3}.Pa^{-1}}$
V_H	2.78×10^{-5}	2.78×10^{-4}	2.78×10^{-7}	$\mathrm{m}^3.\mathrm{mol}^{-1}$

Table 5.4: Modeling parameters used for polymeric liner, defect, and composite material.

5.4 Results and Discussion

After modeling and simulating the H_2 permeation through the RVE sample of 70 MPa Type IV COPV with pre-existing defects, H_2 flux (J) is investigated with time. The contour of J variation is driven by C and p, and the H_2 -polymer interaction at the inner surface follows Henry's law. The contour for J across the thickness of the sample for a defect inside the polymer (case I), and for the defect at the interface of liner-composite (case II) are as shown in Fig. 5.4 and 5.5, respectively.

At the initial stage, J is very slow, and after some hours, H_2 starts diffusing in polymer and goes into a saturation state by maintaining a constant internal p of 70 MPa after filling.

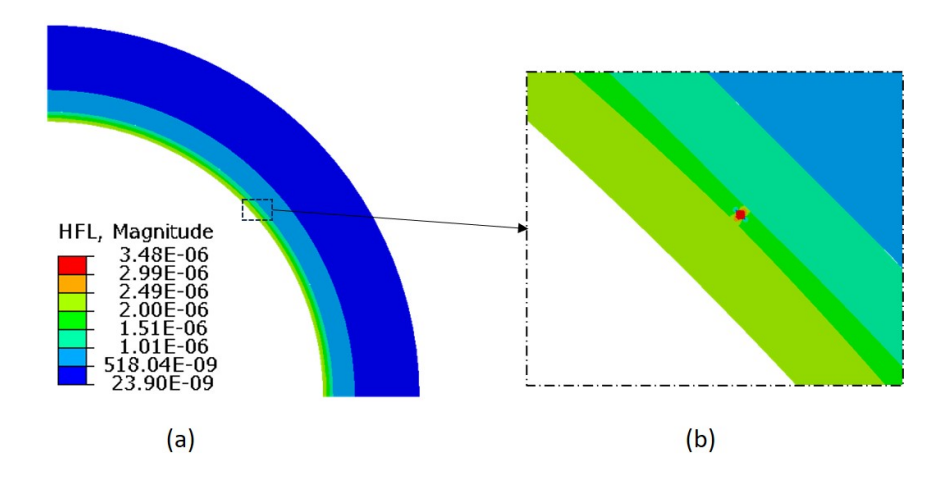


Figure 5.4: Contour for J (a) across the thickness of the sample, and (b) with defect at the center of polymeric liner material.

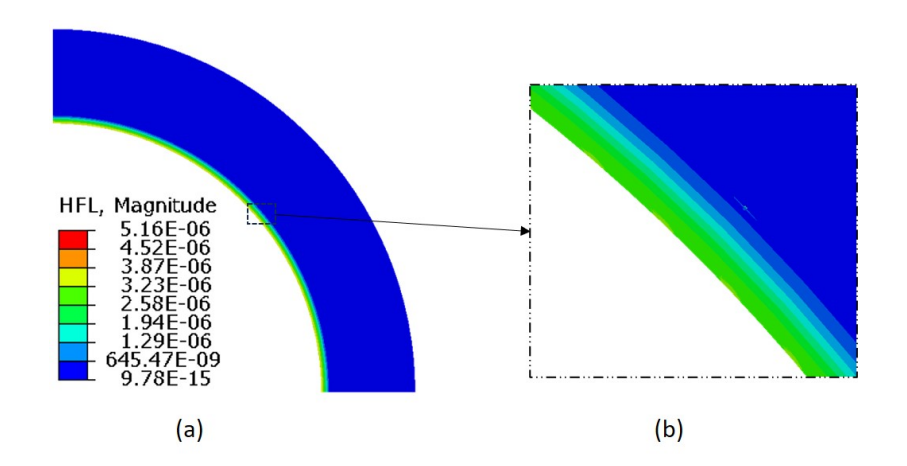


Figure 5.5: Contour for J (b) across the thickness of the sample, and (b) with defect at the interface of liner-composite material.

The J rate increases with time and after several hours, it reaches a saturation state inside the defect, which means the J is constant with time throughout the thickness of the RVE sample (as per Fig. 5.1). The J due to defect inside polymeric liner material and for the defect at the interface of polymeric liner-composite are 3.48×10^{-6} and 5.16×10^{-6} mol.s⁻¹.m⁻². The J of case II defect is higher since after the accumulation of H_2 , the p generated at the interface allows the passage of H_2 through the composite due to higher diffusivity. In case of a defect inside the polymer, the polymeric liner material does not allow H_2 to pass easily, and J is lower as compared to a semicircular defect at the liner-composite interface. This means J is not uniform due to defects present in the RVE. Also, the CFRP properties are assumed values that are not available in the literature for Type IV COPVs due to their porous behavior. So, the permeability prediction is not effective in these cases. Therefore, it is important to check the p generated by these defects and their effect on the yield behavior of the material to estimate the chance of blister formation due to pre-existing manufacturing defects.

The p variation in both defects is monitored during the operational cycle, as shown in Fig. 5.6. The p_{max} generated inside the defect for case I is 126 MPa, and for case II is 113 MPa. The p variation for case I starts from a 65 MPa value due to fast filling or sudden pressurization up to 70 MPa, and it increases during the saturation period at a faster rate due to the accumulation of H_2 inside the pre-existing circular defect of the polymeric liner material. Due to sudden decompression, a decrease in p value was found during the defilling period. The p_{min} of 20 MPa was applied on the boundary during dwelling period. Due to the accumulation of H_2 within the defect, the pressure value decreases linearly.

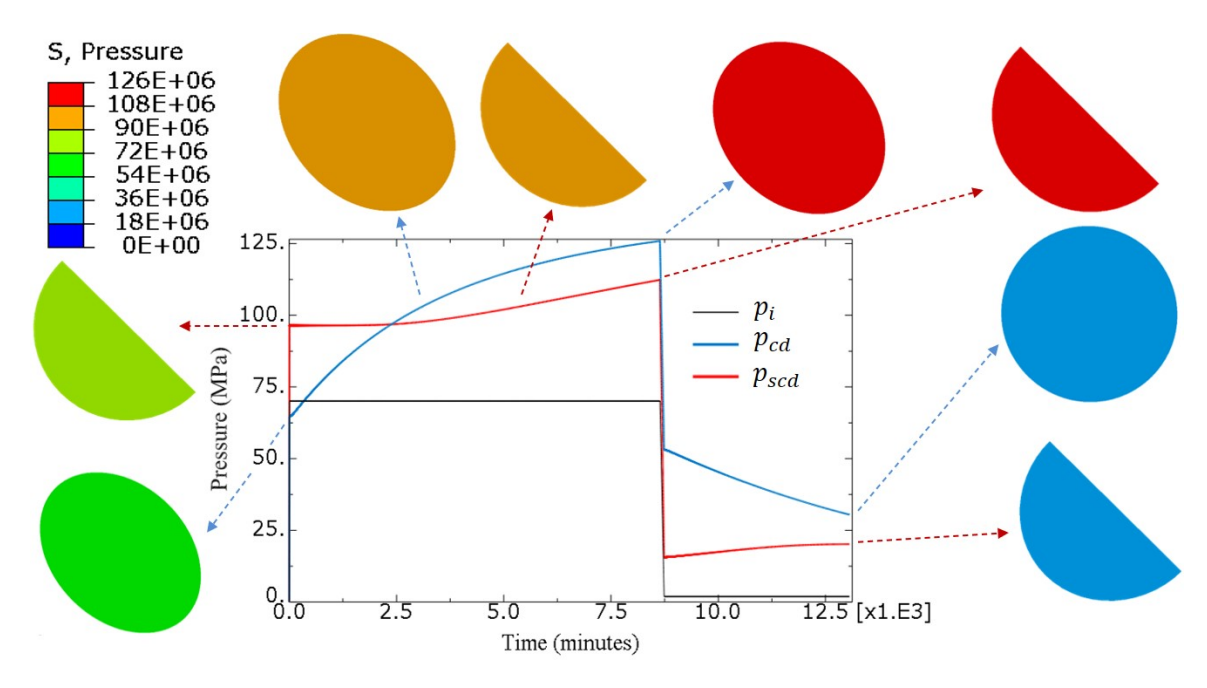


Figure 5.6: Pressure variation with time for the defect inside the polymer (p_{cd}) and defect at the liner-composite interface (p_{psd}) concerning the similar applied p_i for first cycle.

For a similar loading condition, the p variation with time for case II is shown in Fig. 5.6. The p value starts from 90 MPa due to sudden pressurization, and its value is much higher than that in case I. Because the defect position in case II is at the interface of the liner-composite and there is an increase in resistance, the stress value is exceeded. During the saturation period, the rate of increase of stress is low because the composite has a higher diffusivity, due to which H_2 accumulation is much lower at the interface. During decompression, the sudden drop in p value increased slightly in a linear fashion during the dwelling period because of the accumulation of H_2 in the interfacial semicircular defect.

The p generated is compared with the material yield limit, the theoretical decompression damage limit, and the permeation damage limit to identify the failure conditions [211, 205, 18]. The diffusive properties are based on theoretically calculated $p_{d,D}$ using Eqn. (5.3) for p_i 70 MPa, C_i 867 mol.m⁻³, S 1.8 × 10⁻⁶ mol.m⁻³.Pa⁻¹ obtained as 411.6 MPa. Material yield-based $p_{d,Y}$ using Eqn. (5.4) for the yield value of 24.1 MPa is 16.1 MPa. If p developed inside the defect exceeds $p_{d,Y}$ the yielding will begin. The p inside the

defect arises due to the diffusive properties of the polymeric liner material for H_2 gas. So, the failure is shown only if $p_{d,D}$ is greater than the theoretically calculated value of 411.6 MPa. The p_{max} generated inside the defect for cases I and II are 126 MPa and 113 MPa respectively.

The p generated at the defect site inside the liner material, at the end of the first cycle is nearly 126 MPa. In the next cycle, the pressure inside the defect has increased to 131 MPa as shown in Fig. 5.7. So, we can say that the pressure inside the defect increased by 416 MPa in 58th cycle, which is exceeding the $p_{d,D}$ of 411.6 MPa. This could be responsible for blister formation.

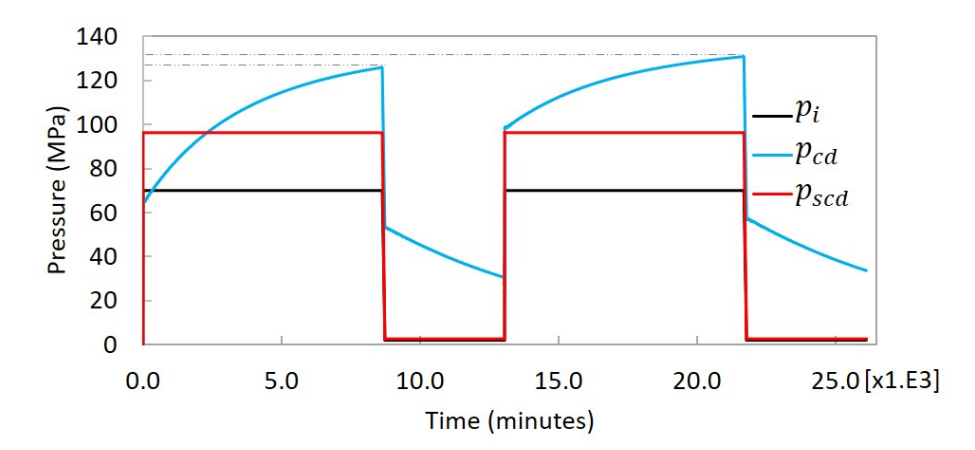


Figure 5.7: Pressure variation with time for the defect inside the polymer (p_{cd}) and defect at the liner-composite interface (p_{psd}) concerning the similar applied p_i for two cycle.

The applied H_2 concentration C_i , concentration due to defect inside polymer C_{cd} and concentration due to defect at the liner-composite C_{scd} are shown in Fig. 5.8. The H_2 concentration for fast depressurization rate (dp_1) of 0.7 MPa/min and slow depressurization rate (dp_2) of 0.07 MPa/min has not shown a significant change. For slower dp_2 the time taken is longer as compared to faster dp_1 , which results in slower drop of H_2 concentration with time. The defect present inside the polymeric liner material showed accumulation of more H_2 concentration, which results in pressure buildup inside the defect as per Henry's law.

Therefore, simulation results provide an understanding of p build-up inside defects during the filling and defilling cycle. These results provided insight into the effect of the location of micro-defects on predicting the chance of blister formation (and damage initiation) under the operational conditions of Type IV COPVs. The discussion of this chapter is as follows:

1. After p_b qualification and ensuring that the H_2 permeability is within the limit at p_{nwp} for the optimal thickness of liner material, the defilling test needs to be performed to check the effect of decompression and ensure the safety of Type IV COPV. Since defects are introduced during the manufacturing and processing of

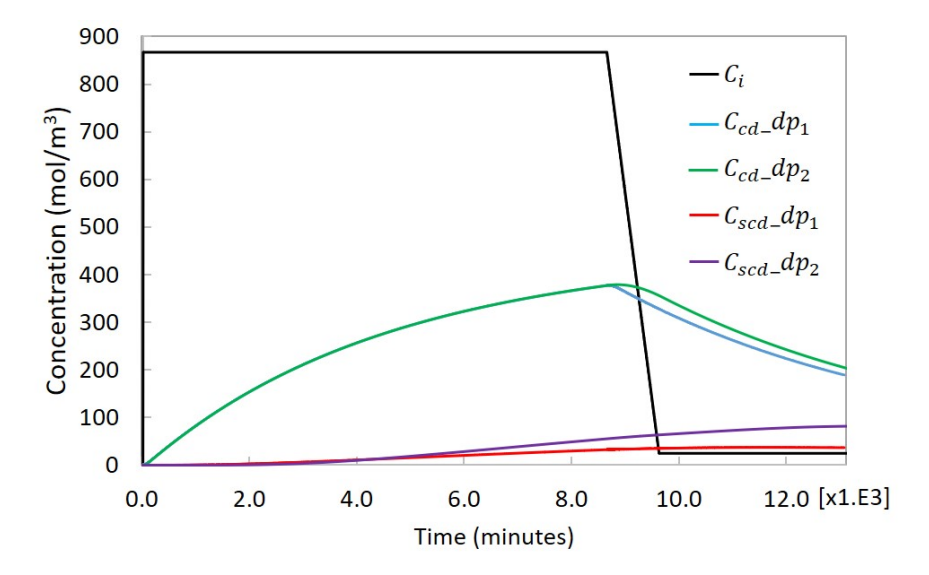


Figure 5.8: Concentration variation with time for the defect inside the polymer (C_{cd}) and defect at the liner-composite interface (C_{scd}) for single cycle.

the polymeric liner, this can cause 70 MPa Type IV COPVs to fail due to sudden decompression.

- 2. The H_2 permeation mechanism within a FE framework presents an HTM material model for polymers that can capture pressure and concentration-driven permeation.
- 3. The aspects of pre-existing micro-defects found in the liner material and at the liner-composite interface for a representative volume element (RVE) of a 70 MPa Type IV COPV have been investigated. The liner thickness is 5 mm, and the H₂ transport properties are based on the chapter 4 work.
- 4. The effects of pressurization and depressurization on H_2 permeation within these micro-defects lead to molecular H_2 saturation inside the material, and H_2 accumulation within the defects has been analyzed.
- 5. The role of the micro-defects location for a given H₂ filling cycle and the observation that H₂ saturation and accumulation result in pressure buildup within the defects have been examined. The defect at the interface shows very little accumulation of H₂ due to the porous nature of the composite. The composite has a higher diffusivity as compared to the polymeric liner material.
- 6. The results obtained from our study provide valuable insights into understanding the location of micro-defects, which can help to determine their potential to cause failure or remain acceptable during the operational cycle of Type IV COPVs in on-board applications.
- 7. In addition, the number of cycles estimated could cause blister formation for a given defect size, location, material properties, liner thickness, and loading conditions. For an increase in the number of cycles, the defect inside the polymeric liner material is

critical due to an increase in pressure buildup during each cycle, and for the defect at the liner-composite interface, the pressure decreased with an increase in the loading cycle.

8. Also, the effect of minimum and maximum decompression rates provided valuable insight into the defects present inside the liner and at the liner-composite interface. The defect present inside the liner material does not show a significant effect due to the rate of decompression. However, the interface shows a significant reduction in concentration variation within the defect present at the liner-composite interface. The slower rate of decompression shows a higher concentration value due to the increased saturation time inside the material.

5.5 Conclusion

The present chapter explores the simulation-assisted framework to understand the mechanism of H_2 transport through pre-existing micro defects in polymeric liner material and liner-composite interface, considering operational cycle requirements and safety concerns related to p_{nwp} of 70 MPa Type IV COPV. A multi-variable H_2 transport permeation analysis has been conducted using the extended governing equations of Fick's law for RVE of Type IV COPV material and the defilling-induced blistering model.

The analysis estimated the H_2 saturation inside the material and its accumulation within the defects. Such H_2 saturation and accumulation result in p build-up due to increased C within the defects. Although there is a minimal accumulation of H_2 in both cases, as it is released by the composite, it contributes to increased p and generates maximum stress within the defect. By analyzing this data, p_{max} is predicted that may develop within a defect. Even though the chosen defect size is small, it can initiate and contribute to failure. This information is valuable in understanding the location of micro defects that may lead to failure or be acceptable during the operational cycle for 70 MPa Type IV COPVs in onboard applications to avoid failure due to H_2 permeation.

Chapter 6

Conclusion and Future Scope

6.1 Conclusion

This thesis addresses critical challenges in the design and development of a Type IV COPV with p_{nwp} of 70 MPa, focusing on manufacturing defects. It is shown that design parameters are crucial for defect-free manufacturing of Type IV COPVs and can significantly impact their performance. Besides mechanical failure at burst pressure, polymeric liner material failure due to H_2 permeation during operational cycles is modeled using a novel hydrogen transport material model (HTM) developed in this work. The elimination of manufacturing defects has been found to improve the high-pressure H_2 storage Type IV COPV performance and safety.

The first objective (Chapter 3) of this thesis work has proposed a design solution for prototype development of Type IV COPV having 18 L capacity to store 0.75 kg of H₂. The design and manufacturing aspects responsible for the failure at burst pressure of more than 150 MPa have been investigated through the utilization of numerical modeling. The NA was utilized to estimate the initial thickness required to sustain the burst pressure load in the circumferential and axial directions. The CLT has been utilized inside the Abaqus software to simulate the composite material with Tsai-Wu failure criteria. Upon analyzing the mechanism of failure, several design and manufacturing flaws associated with the Type IV COPV have been eliminated. Furthermore, the maximum possible burst pressure has been investigated after making the safer 70 MPa Type IV COPV.

In the second objective (Chapter 4) of this thesis work, a HTM modeling framework has been developed by implementing concentration as well as pressure-driven diffusion at a constant temperature. The developed modeling framework is implemented using UMATHT subroutines in the commercial FE solver Abaqus. This study uses the chemical potential method to simulate the effects of both concentration and pressure on the H₂ transport properties. The experimental work of Fujiwara et al. 2020, 2021 (Exp.) has been validated to verify the HTM for H₂ transport properties evaluated for the applied pressure of 90 MPa. This simulation results demonstrated the model's accuracy with the comparison with Exp. data. In addition, the role of the H₂ transport mechanism through the polymer is highlighted in this chapter. The simulation results revealed the effect of compression due to H₂ pressure on polymer transport properties. Further, using this HTM method, the minimum thickness required for the Type IV COPV polymeric liner material

to restrict the H_2 permeation limit at 70 MPa of p_{nwp} was determined.

The third objective (Chapter 5) has used HTM to examine the effects of pressurization and depressurization of H₂ on pre-existing micro-defects inside Type IV COPV. In this study, a representative sample of the cylindrical section of Type IV COPV has been subjected to cyclic loading (pressure and concentration) of H₂ and analyzed using the FE modeling framework. Such H₂ saturation and accumulation resulted in p build-up within the defect site. In contrast, the central defect of the polymeric liner material is more likely to accumulate H₂. More specifically, due to the higher diffusivity of the CFRP material, defects at the liner-composite interface result in less H₂ accumulation and consequently less pressure buildup. Therefore, the defect location within the polymeric liner material is responsible for the chance of blister formation. Moreover, the results highlighted that the dynamic H₂ redistribution (driven by pressure and concentration) caused the pressure buildup inside the material due to the presence of pre-existing micro-defects, which could be responsible for the blistering and the failure of the 70 MPa Type IV COPVs.

6.2 Scope for future studies

The possible immediate extensions of the current work for the future include the following:

- The liner-boss and liner-CFRP interfaces will be examined to identify the root causes of interfacial failure. Interfacial strength will be enhanced by analyzing the mechanical effects of polymeric liner surface treatments under cyclic loading conditions. Additionally, the role of galvanic corrosion at the aluminium alloy-CFRP interface and its implications for structural integrity will be evaluated. Design refinements will focus on optimizing manufacturing quality to ensure the Type IV COPVs withstand the minimum required p_b with an optimum strength-to-weight ratio.
- The filament winding manufacturing parameters (e.g., tension, winding angle, cure cycle) associated with towpreg winding methods will be optimized to minimize defects (e.g., fiber misalignment, resin-rich zones) in CFRP composites. A systematic analysis of defect propagation mechanisms (e.g., void formation, interlaminar delamination) will be conducted to mitigate design- and manufacturing-related failures, ensuring structural integrity under critical operational loads.
- The generalized chemical potential method utilized in this thesis for the developed HTM will be extended to blended polymeric liner materials by incorporating specific theories and relations, such as the Nielsen model, to better understand the mechanism of H₂ permeation and enhance gas barrier performance for real-world industrial applications. To capture the local and nonlinear behavior of different blended polymers interacting with high-pressure gaseous H₂, with glassy and rubbery phase behavior will be integrated using the dual-mode sorption model. In future

research, we plan to expand our analysis to include a larger dataset encompassing various industrial-grade polymers (such as PA6, EVOH, and PET) and their blends.

• The novel HTM model presented in this thesis will be extended into a coupled temperature-stress-diffusion model. The dynamics of the filling-defueling cycle and the associated failure scenarios of high-pressure Type IV COPVs, resulting from manufacturing defects within the polymer and at the polymer-composite interface, will be examined. This analysis will take into account the realistic bonding phenomena between the polymeric liner and the composite material.

These extensions aim to enhance performance parameters, reduce manufacturing and operational uncertainties for Type IV COPVs with $p_{\rm nwp}$ of 70 MPa for efficient H_2 storage solutions.

References

- [1] S McWhorter and G Ordaz. Onboard Type IV compressed hydrogen storage systems-current performance and cost. *DOE Fuel Cell Technologies Office Record*, 13013, 2013.
- [2] Julie Pepin, Eric Lainé, Jean-Claude Grandidier, Sylvie Castagnet, Pierre Blanc-Vannet, Philippe Papin, and Mathilde Weber. Determination of key parameters responsible for polymeric liner collapse in hyperbaric Type IV hydrogen storage vessels. *International Journal of Hydrogen Energy*, 43(33):16386–16399, 2018.
- [3] Kaveh Mazloomi and Chandima Gomes. Hydrogen as an energy carrier: Prospects and challenges. Renewable and Sustainable Energy Reviews, 16(5):3024–3033, 2012.
- [4] Alessandro Campari, Federico Ustolin, Antonio Alvaro, and Nicola Paltrinieri. A review on hydrogen embrittlement and risk-based inspection of hydrogen technologies. *International Journal of Hydrogen Energy*, 48(90):35316–35346, 2023.
- [5] Sunita Satyapal, John Petrovic, Carole Read, George Thomas, and Grace Ordaz. The US department of energy's national hydrogen storage project: Progress towards meeting hydrogen-powered vehicle requirements. *Catalysis today*, 120(3-4):246–256, 2007.
- [6] Francisco Rubio, Carlos Llopis-Albert, and Antonio José Besa. Optimal allocation of energy sources in hydrogen production for sustainable deployment of electric vehicles. *Technological Forecasting and Social Change*, 188:122290, 2023.
- [7] Ramin Moradi and Katrina M Groth. Hydrogen storage and delivery: Review of the state of the art technologies and risk and reliability analysis. *International Journal of Hydrogen Energy*, 44(23):12254–12269, 2019.
- [8] Paul C Okonkwo, Ikram Ben Belgacem, Ibrahim B Mansir, Mansur Aliyu, Wilfred Emori, Paul C Uzoma, Wesam H Beitelmal, Ersin Akyüz, Ahmed Bahgat Radwan, RA Shakoor, et al. A focused review of the hydrogen storage tank embrittlement mechanism process. *International Journal of Hydrogen Energy*, 48(35):12935–12948, 2023.
- [9] Jin-Ho Hong, Min-Gu Han, and Seung-Hwan Chang. Safety evaluation of 70 MPa-capacity Type III hydrogen pressure vessel considering material degradation of composites due to temperature rise. Composite Structures, 113:127–133, 2014.
- [10] William H Johnson. On some remarkable changes produced in iron and steel by the action of hydrogen and acids. *Nature*, 11(281):393–393, 1875.

- [11] May L Martin and Petros Sofronis. Hydrogen-induced cracking and blistering in steels: A review. Journal of Natural Gas Science and Engineering, 101:104547, 2022.
- [12] Gunyoung Park and Chul Kim. Composite layer design using classical laminate theory for high pressure hydrogen vessel (Type 4). *International Journal of Precision Engineering and Manufacturing*, 24(4):571–583, 2023.
- [13] Valery V. Vasiliev. Composite Pressure Vessels: Design, Analysis, and Manufacturing. Bull Ridge Corporation, Blacksburg, VA, 2009.
- [14] Shuguang Li, Elena Sitnikova, Yuning Liang, and Abdul-Salam Kaddour. The Tsai-Wu failure criterion rationalised in the context of UD composites. *Composites Part A: Applied Science and Manufacturing*, 102:207–217, 2017.
- [15] Juan Pedro Berro Ramirez, Damien Halm, Jean-Claude Grandidier, Stephane Villalonga, and Fabien Nony. 700 bar Type IV high pressure hydrogen storage vessel burst-Simulation and experimental validation. *International Journal of Hydrogen* Energy, 40(38):13183–13192, 2015.
- [16] Yasutoshi Naito, Keishin Mizoguchi, Katsuhiko Terada, and Yoshinori Kamiya. The effect of pressure on gas permeation through semicrystalline polymers above the glass transition temperature. *Journal of Polymer Science Part B: Polymer Physics*, 29 (4):457–462, 1991.
- [17] Yasutoshi Naito, Yoshinori Kamiya, Katsuhiko Terada, Keishin Mizoguchi, and Jin-Sheng Wang. Pressure dependence of gas permeability in a rubbery polymer. Journal of Applied Polymer Science, 61(6):945–950, 1996.
- [18] Hirotada Fujiwara, Hiroaki Ono, Keiko Ohyama, Masahiro Kasai, Fumitoshi Kaneko, and Shin Nishimura. Hydrogen permeation under high pressure conditions and the destruction of exposed polyethylene-property of polymeric materials for high-pressure hydrogen devices (2)-. International Journal of Hydrogen Energy, 46 (21):11832–11848, 2021.
- [19] Maximiliano Melnichuk, Quentin Gardavaud, Frédéric Thiébaud, and Dominique Perreux. Temperature effect in cavitation risk assessments of polymers for hydrogen systems. *International Journal of Hydrogen Energy*, 45(43):23020–23026, 2020.
- [20] Thomas A Yersak, Daniel R Baker, Yuka Yanagisawa, Stefan Slavik, Rainer Immel, André Mack-Gardner, Michael Herrmann, and Mei Cai. Predictive model for depressurization-induced blistering of Type IV tank liners for hydrogen storage. International Journal of Hydrogen Energy, 42(48):28910–28917, 2017.
- [21] Maximiliano Melnichuk, Frédéric Thiébaud, and Dominique Perreux. Non-dimensional assessments to estimate decompression failure in polymers

- for hydrogen systems. International Journal of Hydrogen Energy, 45(11):6738–6744, 2020.
- [22] Shank S Kulkarni, Yongsoon Shin, Kyoo Sil Choi, and Kevin Simmons. Investigation of desorption of hydrogen gas from polymer matrix using thermal desorption analysis and finite element modeling. *Polymer*, 282:126182, 2023.
- [23] Changchen Liu, Zhihui Ouyang, Jiexiang Yu, and Li Ma. Investigation of crack initiation during the burst test of hydrogen storage COPVs. Clean Energy, page zkae123, 2025.
- [24] Hong Li, Kenneth I Johnson, and Norman L Newhouse. Achieving hydrogen storage goals through high-strength fiber glass-final technical report. Technical report, PPG Industries, Inc., Cheswick, PA (United States), 2017.
- [25] SNA Safri, MTH Sultan, and F Cardona. Impact damage evaluation of glass-fiber reinforced polymer (GFRP) using the drop test rig—an experimental based approach. ARPN J Eng Appl Sci, 10(20):9916–9928, 2015.
- [26] Alfredo Rondinella, Giovanni Capurso, Matteo Zanocco, Federico Basso, Chiara Calligaro, Davide Menotti, Alberto Agnoletti, and Lorenzo Fedrizzi. Study of the failure mechanism of a high-density polyethylene liner in a Type IV high-pressure storage tank. *Polymers*, 16(6):779, 2024.
- [27] Weidong Shao, Jing Wang, Donghai Hu, Dagang Lu, and Yinjie Xu. Lightweight Type-IV hydrogen storage vessel boss based on optimal sealing structure. World Electric Vehicle Journal, 15(6):261, 2024.
- [28] Zhiwen Meng, Suke Jin, Meng Yu, Abel Mehari, and Long Jiang. Analysis of the boss structure of Type IV composite vessel for a high-pressure hydrogen tube trailer. Sustainability, 16(12):5098, 2024.
- [29] Junyi Liu, Xiaohu Huang, Yi Ren, Lai Mun Wong, Hongfei Liu, and Shijie Wang. Galvanic corrosion protection of Al-alloy in contact with carbon fibre reinforced polymer through plasma electrolytic oxidation treatment. Scientific Reports, 12(1), 2022.
- [30] Xuguang Liu, Zhenlian An, Fang Liu, Yong Yang, and Hanbo Zheng. Surface modification of aluminum alloy electrodes via direct fluorination to enhance flashover voltage of epoxy insulators and related mechanisms. Surfaces and Interfaces, page 106004, 2025.
- [31] Eva Hakansson. Galvanic corrosion of aluminum/carbon composite systems. PhD thesis, University of Denver, 2016.
- [32] Eva Håkansson, Joseph Hoffman, Paul Predecki, and Maciej Kumosa. The role of corrosion product deposition in galvanic corrosion of aluminum/carbon systems. Corrosion Science, 114:78–87, 2017.

- [33] J. M. Jáquez-Muñoz, A. N. Castrejon, M. A. Lira-Martínez, E. Maldonado-Bandala, J. Cabral-Miramontes, M. Lara-Banda, F. Estupiñán-López, D. Nieves-Mendoza, C. Gaona-Tiburcio, and F. Almeraya-Calderón. Corrosion behavior of aluminum-carbon fiber/epoxy sandwich composite exposed on NaCl solution. Frontiers in Metals and Alloys, 2:1258941, 2023.
- [34] Pietro Moretto and Spencer Quong. Legal requirements, technical regulations, codes, and standards for hydrogen safety. In *Hydrogen safety for energy applications*, pages 345–396. Elsevier, 2022.
- [35] Emma Davies, Andrea Ehrmann, and Eva Schwenzfeier-Hellkamp. Safety of hydrogen storage technologies. *Processes*, 12(10):2182, 2024.
- [36] Jiqi Zhu, Yan Li, Wenhong Cao, Yuebing Li, and Zengliang Gao. Failure analysis of novel boss structures for Type IV hydrogen storage vessels. *Energies*, 16(10):4005, 2023.
- [37] J Jerold John Britto, R Venkatesh, K Amudhan, A Vasanthanathan, N Gokulakrishnan, and M Manikandan. Micromechanics study on FRP composite cylinder under finite element simulation comsol multiphysics. *Materials Today:* Proceedings, 45:804–810, 2021.
- [38] Donghai Hu, Weidong Shao, Dagang Lu, Yinjie Xu, and Jing Wang. Design and material optimization of carbon fiber composite winding reinforcement layer for vehicle Type-IV hydrogen storage vessels. *Journal of Energy Storage*, 100:113459, 2024.
- [39] Anka Trajkovska Petkoska, Blagoja Samakoski, Bisera Samardjioska Azmanoska, and Viktorija Velkovska. Towpreg—an advanced composite material with a potential for pressurized hydrogen storage vessels. *Journal of Composites Science*, 8(9):374, 2024.
- [40] Kumar C Jois, Tim Mölling, Jakob Schuster, Niels Grigat, and Thomas Gries. Towpreg manufacturing and characterization for filament winding application. *Polymer Composites*, 45(9):7893–7905, 2024.
- [41] B Gentilleau, F Touchard, and JC Grandidier. Numerical study of influence of temperature and matrix cracking on Type IV hydrogen high pressure storage vessel behavior. *Composite Structures*, 111:98–110, 2014.
- [42] Samid Khan and Ajay Kumar. Failure analysis in advance cylindrical composite pressure vessel under pressure & temperature for hydrogen storage: A comprehensive review. *Polymer Composites*.
- [43] Yaohua Gong, Tao Huang, Xun'an Zhang, Purong Jia, Yongyong Suo, and Shuyi Zhao. A reliable fracture angle determination algorithm for extended Puck's 3d

- inter-fiber failure criterion for unidirectional composites. Materials, 14(21):6325, 2021.
- [44] Alfred Puck and H Matthias Deuschle. Progress in the Puck failure theory for fibre reinforced composites: Analytical solutions for 3d-stress. Compos. Sci. Technol, 62: 371–378, 2002.
- [45] Song Lin, Liuqing Yang, Hui Xu, Xiaolong Jia, Xiaoping Yang, and Lei Zu. Progressive damage analysis for multiscale modelling of composite pressure vessels based on Puck failure criterion. *Composite structures*, 255:113046, 2021.
- [46] Mohsen Ahmadi Jebeli and Mohammad Heidari-Rarani. Development of Abaqus WCM plugin for progressive failure analysis of Type IV composite pressure vessels based on Puck failure criterion. *Engineering Failure Analysis*, 131:105851, 2022.
- [47] M Nebe, A Johnan, C Braun, and JMJF Van Campen. The effect of stacking sequence and circumferential ply drop locations on the mechanical response of Type IV composite pressure vessels subjected to internal pressure: A numerical and experimental study. *Composite Structures*, 294:115585, 2022.
- [48] Reham Reda, Mennatullah Khamis, Adham E Ragab, Ahmed Elsayed, and AM Negm. Numerical analysis of the impact of winding angles on the mechanical performance of filament wound Type 4 composite pressure vessels for compressed hydrogen gas storage. *Heliyon*, 10(13), 2024.
- [49] Marie Hondekyn, Nazim Ali, and Wim Van Paepegem. Closed-form analytical model for the cylinder region of thick-walled composite pressure vessels for hydrogen storage. *International Journal of Hydrogen Energy*, 87:457–468, 2024.
- [50] Jagath Narayana Kamineni and Ramesh Gupta Burela. Modeling, fabrication, and burst testing of Type-IV 3D printed plastic liner composite overwrapped pressure vessels. *International Journal on Interactive Design and Manufacturing (IJIDeM)*, pages 1–10, 2024.
- [51] Lucas L Agne, José Humberto S Almeida Jr, Sandro C Amico, and Maikson LP Tonatto. Impact of stacking sequence on burst pressure in glass/epoxy Type IV composite overwrapped pressure vessels for CNG storage. *International Journal of Pressure Vessels and Piping*, 212:105315, 2024.
- [52] Qian Zhang, Wenchun Jiang, Jiupeng Yan, Jiangkun Bai, Hui Fan, and Bingying Wang. Influence of composite material laying parameters on the load-carrying capacity of Type IV hydrogen storage vessel. Science and Engineering of Composite Materials, 31(1):20240046, 2024.
- [53] HS Roh, TQ Hua, and RK Ahluwalia. Optimization of carbon fiber usage in Type 4 hydrogen storage tanks for fuel cell automobiles. *International Journal of Hydrogen Energy*, 38(29):12795–12802, 2013.

- [54] Zhen Liu, Feiyu Zhou, Chao Zou, and Jianping Zhao. Fracture performance study of carbon-fiber-reinforced resin matrix composite winding layers under UV aging effect. *Materials*, 17(4):846, 2024.
- [55] ES Barboza Neto, M Chludzinski, PB Roese, JSO Fonseca, SC Amico, and CA Ferreira. Experimental and numerical analysis of a LLDPE/HDPE liner for a composite pressure vessel. *Polymer Testing*, 30(6):693–700, 2011.
- [56] David Leh, Philippe Saffré, Pascal Francescato, Robert Arrieux, and Stéphane Villalonga. A progressive failure analysis of a 700-bar Type IV hydrogen composite pressure vessel. *International Journal of Hydrogen Energy*, 40(38):13206–13214, 2015.
- [57] Thanh Q Hua, Hee-Seok Roh, and Rajesh K Ahluwalia. Performance assessment of 700-bar compressed hydrogen storage for light duty fuel cell vehicles. *International Journal of Hydrogen Energy*, 42(40):25121–25129, 2017.
- [58] Martin Nebe, TJ Asijee, Christian Braun, JMJF Van Campen, and F Walther. Experimental and analytical analysis on the stacking sequence of composite pressure vessels. *Composite structures*, 247:112429, 2020.
- [59] Qian Zhang, Hui Xu, Xiaolong Jia, Lei Zu, Shuo Cheng, and Huabi Wang. Design of a 70 MPa Type IV hydrogen storage vessel using accurate modeling techniques for dome thickness prediction. *Composite Structures*, 236:111915, 2020.
- [60] Kumar C Jois, Marcus Welsh, Thomas Gries, and Johannes Sackmann. Numerical analysis of filament wound cylindrical composite pressure vessels accounting for variable dome contour. *Journal of Composites Science*, 5(2):56, 2021.
- [61] V Alcántar, SM Aceves, E Ledesma, S Ledesma, and E Aguilera. Optimization of Type 4 composite pressure vessels using genetic algorithms and simulated annealing. International Journal of Hydrogen Energy, 42(24):15770–15781, 2017.
- [62] M Nebe, A Soriano, C Braun, P Middendorf, and F Walther. Analysis on the mechanical response of composite pressure vessels during internal pressure loading: FE modeling and experimental correlation. Composites Part B: Engineering, 212: 108550, 2021.
- [63] Daniele Landi, Alessio Vita, Samir Borriello, Martina Scafà, Michele Germani, et al. A methodological approach for the design of composite tanks produced by filament winding. Comput. Des. Appl, 17:1229–1240, 2020.
- [64] A Hocine, A Ghouaoula, F Kara Achira, S M Medjdoub, F Kara Achira, and S M Medjdoub. Analysis of failure pressures of composite cylinders with a polymer liner of Type IV CNG vessels. *International Journal of Mechanical, Industrial Science and Engineering*, 7(1):148–152, 2013.

- [65] Shah Alam, Gregory R Yandek, Richard C Lee, and Joseph M Mabry. Design and development of a filament wound composite overwrapped pressure vessel. *Composites* Part C, 2:100045, 2020.
- [66] Meng-Kao Yeh and Tai-Hung Liu. Finite element analysis of graphite/epoxy composite pressure vessel. Journal of Materials Science and Chemical Engineering, 5(7):19–28, 2017.
- [67] Maria Mikroni, Grigorios Koutsoukis, Dimitrios Vlachos, Vassilis Kostopoulos, Antonios Vavouliotis, George Trakakis, Dimitrios Athinaios, Chrysavgi Nikolakea, and Dimitrios Zacharakis. Design, analysis, and testing of a Type V composite pressure vessel for hydrogen storage. *Polymers*, 16(24):3576, 2024.
- [68] Zohir Benrabah, Florin Ilinca, F Giraldeau, Sylvain Bournival, and Anna Bardetti. Contribution to modeling hydrogen permeation and thickness optimization in blow molded plastic liners for on-board compressed hydrogen tanks. *International Journal* of Hydrogen Energy, 51:688–694, 2024.
- [69] P Adams, A Bengaouer, B Cariteau, Vladimir Molkov, and AG Venetsanos. Allowable hydrogen permeation rate from road vehicles. *International Journal of Hydrogen Energy*, 36(3):2742–2749, 2011.
- [70] Y Khalil, N Newhouse, K Simmons, and D Dedrick. Potential diffusion-based failure modes of hydrogen storage vessels for on-board vehicular use. In *Chemical Institute of Chemical Engineers (AIChE): 2010 Annual Meeting*. Chemical Institute of Chemical Engineers (AIChE), 2010.
- [71] Chih-Chiang Pai, Ru-Jong Jeng, Steven J Grossman, and Jan-Chan Huang. Effects of moisture on thermal and mechanical properties of nylon-6, 6. Advances in Polymer Technology: Journal of the Polymer Processing Institute, 9(2):157–163, 1989.
- [72] Anna Katharina Sambale, Michael Stanko, Jessica Emde, and Markus Stommel. Characterisation and FE modelling of the sorption and swelling behaviour of polyamide 6 in water. *Polymers*, 13(9):1480, 2021.
- [73] Alain Tressaud, Etienne Durand, Christine Labrugère, Alexander P Kharitonov, and Larisa N Kharitonova. Modification of surface properties of carbon-based and polymeric materials through fluorination routes: From fundamental research to industrial applications. *Journal of Fluorine Chemistry*, 128(4):378–391, 2007.
- [74] Alain Tressaud, Etienne Durand, Christine Labrugère, Alexander P Kharitonov, Galina V Simbirtseva, Larisa N Kharitonova, and Marc Dubois. Surface modification of polymers treated by various fluorinating media. Acta Chimica Slovenica, 60(3): 495–504, 2013.

- [75] Alexander P Kharitonov and Larisa N Kharitonova. Surface modification of polymers by direct fluorination: A convenient approach to improve commercial properties of polymeric articles. Pure and Applied Chemistry, 81(3):451–471, 2009.
- [76] Nikolay A Belov, Alexander Y Alentiev, Yulia G Bogdanova, Artem Y Vdovichenko, and Dmitrii S Pashkevich. Direct fluorination as method of improvement of operational properties of polymeric materials. *Polymers*, 12(12):2836, 2020.
- [77] Alexander P Kharitonov, Galina V Simbirtseva, Alain Tressaud, Etienne Durand, Christine Labrugère, and Marc Dubois. Comparison of the surface modifications of polymers induced by direct fluorination and rf-plasma using fluorinated gases. *Journal of Fluorine Chemistry*, 165:49–60, 2014.
- [78] Dávid István Kis, Attila Bata, János Takács, and Eszter Kókai. Mechanical properties of clay-reinforced polyamide 6 nanocomposite liner materials of Type IV hydrogen storage vessels. *Nanomaterials*, 14(17):1385, 2024.
- [79] Xiang Li, Qianghua Huang, Yitao Liu, Baodi Zhao, and Jiepu Li. Review of the hydrogen permeation test of the polymer liner material of Type IV on-board hydrogen storage cylinders. *Materials*, 16(15):5366, 2023.
- [80] Xiang Li, Chufeng Dong, Yitao Liu, Jiepu Li, Guangfu Bin, Chilou Zhou, and Wulin Han. Study on the effect of hydrogen cycle pressure relief time on the hydrogen permeability and mechanical properties of polyamide liner materials for Type IV hydrogen storage cylinders of HFCVs. *International Journal of Hydrogen Energy*, 95:993–1003, 2024.
- [81] Pierre Blanc-Vannet, Philippe Papin, Mathilde Weber, Philippe Renault, Julie Pepin, Eric Lainé, G Tantchou, Sylvie Castagnet, and J-C Grandidier. Sample scale testing method to prevent collapse of plastic liners in composite pressure vessels. *International Journal of Hydrogen Energy*, 44(17):8682–8691, 2019.
- [82] Barton Smith. Lifecycle verification of tank liner polymers. Technical report, Oak Ridge National Lab, United States, 2014.
- [83] Shank S Kulkarni, Kyoo Sil Choi, Wenbin Kuang, Nalini Menon, Bernice Mills, Ayoub Soulami, and Kevin Simmons. Damage evolution in polymer due to exposure to high-pressure hydrogen gas. *International Journal of Hydrogen Energy*, 46(36): 19001–19022, 2021.
- [84] Sompong Prachumchon. A study of HDPE in high pressure of hydrogen gas Measurement of permeation parameters and fracture criteria. Phd, Mechanical Materials Engineering, Department, University of Nebraska-Lincoln, 2012.
- [85] Julien Jaravel, Sylvie Castagnet, Jean-Claude Grandidier, and Guillaume Benoît. On key parameters influencing cavitation damage upon fast decompression in a hydrogen saturated elastomer. *Polymer Testing*, 30(8):811–818, 2011.

- [86] MC Kane. Permeability, solubility, and interaction of hydrogen in polymers-An assessment of materials for hydrogen transport. Savannah River Site: Aiken, SC, USA, 2008.
- [87] Nalini C Menon, Alan M Kruizenga, Kyle J Alvine, Chris San Marchi, April Nissen, and Kriston Brooks. Behaviour of polymers in high pressure environments as applicable to the hydrogen infrastructure. In *Pressure vessels and piping conference*. American Society of Mechanical Engineers, 2016.
- [88] Hirotada Fujiwara, Hiroaki Ono, Kiyoaki Onoue, and Shin Nishimura. High-pressure gaseous hydrogen permeation test method-property of polymeric materials for high-pressure hydrogen devices (1)-. *International Journal of Hydrogen Energy*, 45(53):29082–29094, 2020.
- [89] J Yamabe and Shin Nishimura. Estimation of critical pressure of decompression failure of EPDM composites for sealing under high-pressure hydrogen gas. In 18th European Conference on Fracture: Fracture of Materials and Structures from Micro to Macro Scale, ECF 2010, 2010.
- [90] Ray Grenoble and Thomas Gates. Hydrogen permeability of polymer matrix composites at cryogenic temperatures. In 46th AIAA/ASME/ASCE/AHS/ASC structures, structural dynamics and materials conference, page 2086, 2005.
- [91] Jae Kap Jung, Kyu Tae Kim, Un Bong Baek, and Seung Hoon Nahm. Volume dependence of hydrogen diffusion for sorption and desorption processes in cylindrical-shaped polymers. *Polymers*, 14(4):756, 2022.
- [92] Marie-Hélène Klopffer, Philippe Berne, and Éliane Espuche. Development of innovating materials for distributing mixtures of hydrogen and natural gas: Study of the barrier properties and durability of polymer pipes. Oil & Gas Science and Technology, 70(2):305–315, 2015.
- [93] Nicolas Gay, Takoua Lamouchi, Franck Agostini, Catherine A Davy, and Frédéric Skoczylas. Hydrogen diffusion through polymer membranes. In MATEC Web of Conferences, volume 322. EDP Sciences, 2020.
- [94] Aman Arora, Harpreet Singh, and Dhiraj K Mahajan. Towards the prediction of intergranular fatigue crack initiation in metals due to hydrogen. *Materials Science and Engineering: A*, 787:139488, 2020.
- [95] Rajwinder Singh, Amanjot Singh, Pawan K Singh, and Dhiraj K Mahajan. Role of prior austenite grain boundaries in short fatigue crack growth in hydrogen charged RPV steel. *International Journal of Pressure Vessels and Piping*, 171:242–252, 2019.
- [96] Vishal Singh, Rajwinder Singh, Kanwer Singh Arora, and Dhiraj K Mahajan. Hydrogen induced blister cracking and mechanical failure in X65 pipeline steels. *International Journal of Hydrogen Energy*, 44(39):22039–22049, 2019.

- [97] Ian M Robertson, P Sofronis, A Nagao, ML Martin, S Wang, DW Gross, and KE Nygren. Hydrogen embrittlement understood. Metallurgical and Materials Transactions A, 46(6):2323–2341, 2015.
- [98] Stan Lynch. Discussion of some recent literature on hydrogen-embrittlement mechanisms: Addressing common misunderstandings. *Corrosion Reviews*, 37(5): 377–395, 2019.
- [99] Joakim Andersson and Stefan Grönkvist. Large-scale storage of hydrogen. International Journal of Hydrogen Energy, 44(23):11901–11919, 2019.
- [100] Oo Abdul Rosyid. System-analytic safety evaluation of the hydrogen cycle for energetic utilization. PhD thesis, Otto-von-Guericke-Universität Magdeburg, Universitätsbibliothek, 2006.
- [101] International Organization for Standardization, ISO 19881. Gaseous hydrogen—land vehicle fuel containers, 2018.
- [102] Hiroyuki Yumiya, Mikio Kizaki, and Hisao Asai. Toyota fuel cell system (TFCS). World Electric Vehicle Journal, 7(1):85–92, 2015.
- [103] Kenneth Johnson, Michael J Veenstra, David Gotthold, Kevin Simmons, Kyle Alvine, Bert Hobein, Daniel Houston, Norman Newhouse, Brian Yeggy, Alex Vaipan, et al. Advancements and opportunities for on-board 700 bar compressed hydrogen tanks in the progression towards the commercialization of fuel cell vehicles. SAE International Journal of Alternative Powertrains, 6(2), 2017.
- [104] T-L Teng, C-M Yu, and YY Wu. Optimal design of filament-wound composite pressure vessels. *Mechanics of Composite Materials*, 41(4):333–340, 2005.
- [105] J C Velosa, J P Nunes, PJ Antunes, JF Silva, and AT Marques. Development of a new generation of filament wound composite pressure cylinders. *Composites Science* and *Technology*, 69(9):1348–1353, 2009.
- [106] Mathilde Bouvier, Vincent Guiheneuf, and Alan Jean-Marie. Modeling and simulation of a composite high-pressure vessel made of sustainable and renewable alternative fibers. *International Journal of Hydrogen Energy*, 44(23):11970–11978, 2019.
- [107] M Madhavi, KVJ Rao, and K Narayana Rao. Design and analysis of filament wound composite pressure vessel with integrated-end domes. *Defence Science Journal*, 59 (1), 2009.
- [108] B Gentilleau, F Touchard, J-C Grandidier, and D Mellier. Numerical determination and experimental validation of a technological specimen representative of high-pressure hydrogen storage vessels. *Mechanics of Composite Materials*, 51: 465–478, 2015.

- [109] Christian Hopmann, Nadine Magura, Robert Müller, Daniel Schneider, and Kai Fischer. Impact of winding parameters on the fiber bandwidth in the cylindrical area of a hydrogen pressure vessel for generating a digital twin. *Polymer Composites*, 43 (3):1577–1589, 2022.
- [110] D Cohen. Influence of filament winding parameters on composite vessel quality and strength. Composites Part A: Applied Science and Manufacturing, 28(12):1035–1047, 1997.
- [111] Aleksander Błachut, Tino Wollmann, Maciej Panek, Max Vater, Jerzy Kaleta, Jerzy Detyna, Stefan Hoschützky, and Maik Gude. Influence of fiber tension during filament winding on the mechanical properties of composite pressure vessels. Composite Structures, 304:116337, 2023.
- [112] Pranjali Sharma and Swati Neogi. Performance-based design and manufacturing of filament wound Type-4 cylinders for compressed gas storage. *Composite Structures*, 309:116710, 2023.
- [113] David Cohen, Susan C Mantell, and Liyang Zhao. The effect of fiber volume fraction on filament wound composite pressure vessel strength. *Composites Part B: Engineering*, 32(5):413–429, 2001.
- [114] E Özaslan, K Yurdakul, and C Talebi. Investigation of effects of manufacturing defects on bursting behavior of composite pressure vessels with various stress ratios. *International Journal of Pressure Vessels and Piping*, 199:104689, 2022.
- [115] E Özaslan, BB Incecik, A Yetgin, Bülent Acar, S Güngör, E Sapancı, and Mehmet Ali Güler. Experimental and numerical investigation of the cylinder-dome transition region of a pressure vessel. *Composites Part C*, 4:100119, 2021.
- [116] Dominik Vondráček, Zdeněk Padovec, Tomáš Mareš, and Nirupam Chakraborti. Analysis and optimization of junction between cylindrical part and end dome of filament wound pressure vessels using data driven evolutionary algorithms. Proceedings of the Institution of Mechanical Engineers, Part C: Journal of Mechanical Engineering Science, 238(6):2348–2361, 2024.
- [117] Dorit Munzke, Eric Duffner, René Eisermann, Marcus Schukar, André Schoppa, Mariusz Szczepaniak, Jörg Strohhäcker, and Georg Mair. Monitoring of Type IV composite pressure vessels with multilayer fully integrated optical fiber based distributed strain sensing. *Materials Today: Proceedings*, 34:217–223, 2021.
- [118] Brendan R Murray. Characterisation of rotationally moulded polymer liners for low permeability cryogenic applications in composite overwrapped pressure vessels. National University of Ireland Galway, Galway, Ireland, 2016.
- [119] Serkan Kangal, A Harun Sayı, Ozan Ayakdaş, Osman Kartav, Levent Aydın, H Seçil Artem, Engin Aktaş, Kutay Yücetürk, Metin Tanoğlu, Sinan Kandemir,

- et al. A comprehensive study on burst pressure performance of aluminum liner for hydrogen storage vessels. *Journal of Pressure Vessel Technology*, 143(4):041503, 2021.
- [120] Serkan Kangal. Modeling, simulation and analysis of Type-III composite overwrapped pressure vessels for high-pressure gas storage. PhD thesis, Izmir Institute of Technology (Turkey), 2019.
- [121] Min-Gu Han, Seung-Hwan Chang, et al. Prediction of composite layer thickness for Type III hydrogen pressure vessel at the dome part. *Composite Structures*, 271: 114177, 2021.
- [122] Alexander Air, Md Shamsuddoha, and B Gangadhara Prusty. A review of Type V composite pressure vessels and automated fibre placement based manufacturing. Composites Part B: Engineering, 253:110573, 2023.
- [123] MD Musthak, P Madar Valli, and S Narayana Rao. Prediction of transverse directional strains and stresses of filament wound composite pressure vessel by using higher order shear deformation theories. *International Journal of Composite Materials*, 6(3):79–87, 2016.
- [124] Roham Rafiee and Mohammad Ali Torabi. Stochastic prediction of burst pressure in composite pressure vessels. *Composite Structures*, 185:573–583, 2018.
- [125] Sung-min Cho, Da-eun Kim, Hye-jin Seong, Young-kyu Ko, Hong-chul Kim, Kang-ok Lee, Min-sik Jo, and Sung-ki Lyu. Development of a Type 4 composite cylinder for self-contained breathing apparatus. *Journal of the Korean Society of Manufacturing* Process Engineers, 18(12):1–6, 2019.
- [126] Andrea Haight, Jacob Barker, and Michael Tupper. Optimizing the cost and performance of composite cylinders for H2 storage using a graded construction. Technical report, Composite Technology Development, Inc., Lafayette, USA, 2013.
- [127] M Bertin, S Villalonga, M Vernède, C Magnier, P Tissier, and F Nony. Mechanical behaviour of 700 bar Type IV high pressure vessel: Comparison between simulations and experiments through OSIRHYS IV project. In 15th European Conference on Composite Materials, 2012.
- [128] Sergii Kashkarov, Dmitriy Makarov, and Vladimir Molkov. Performance of hydrogen storage tanks of Type IV in a fire: Effect of the state of charge. *Hydrogen*, 2(4): 386–398, 2021.
- [129] Liang Wang, Chuanxiang Zheng, Hongying Luo, Shuang Wei, and Zongxin Wei. Continuum damage modeling and progressive failure analysis of carbon fiber/epoxy composite pressure vessel. *Composite Structures*, 134:475–482, 2015.

- [130] Liangliang Qi, Wei Min, Ruize Gao, Zhiqi Li, Muhuo Yu, and Zeyu Sun. Optimization of interfacial bonding properties between thermoplastic liners and carbon fiber-reinforced composites by atmospheric-pressure plasma and failure mechanism study. *Polymer Composites*, 44(4):2361–2378, 2023.
- [131] Andres Arciniegas, Hossep Achdjian, Julien Bustillo, François Vander Meulen, and Jerome Fortineau. Experimental simultaneous measurement of ultrasonic properties and thickness for defect detection in curved polymer samples. *Journal* of Nondestructive Evaluation, 36:1–8, 2017.
- [132] Ardeshir Savari, Gholamreza Rashed, and Hadi Eskandari. Failure pressure analysis of pipe repaired by composite sleeve subjected to thermal and mechanical loadings. SN Applied Sciences, 4(7):200, 2022.
- [133] Md Shamsuddoha, Allan Manalo, Thiru Aravinthan, Md Mainul Islam, and Luke Djukic. Failure analysis and design of grouted fibre-composite repair system for corroded steel pipes. *Engineering Failure Analysis*, 119:104979, 2021.
- [134] Xiaodong Zhao, Jianguo Liang, Jianglin Liu, Jun Feng, Zelin Qin, Haifeng Gao, Zhangxin Guo, and Zhaotun Jia. A novel multi-filament winding technique for Type III composite pressure vessel: From CFRP cross-undulation concept to structural performance validation. *International Journal of Hydrogen Energy*, 48 (45):17237–17250, 2023.
- [135] Simulia Inc. Wound composite modeler for Abaqus user's manual. 2007.
- [136] Sotiris Koussios and Otto K Bergsma. Friction experiments for filament winding applications. *Journal of Thermoplastic Composite Materials*, 19(1):5–34, 2006.
- [137] Tasdeeq Sofi, Stefan Neunkirchen, and Ralf Schledjewski. Path calculation, technology and opportunities in dry fiber winding: A review. Advanced Manufacturing: Polymer & Composites Science, 4(3):57–72, 2018.
- [138] Ji Zhou, Jianqiao Chen, Yaochen Zheng, Zhu Wang, and Qunli An. Dome shape optimization of filament-wound composite pressure vessels based on hyperelliptic functions considering both geodesic and non-geodesic winding patterns. *Journal of Composite Materials*, 51(14):1961–1969, 2017.
- [139] Brief filament wound composite pressure vessel analysis with Abaqus. *Abaqus Technology*, 2007.
- [140] Woo Rim Park, Nurul Fajriyah Fatoni, and Oh Heon Kwon. Evaluation of stress and crack behavior using the extended finite element method in the composite layer of a Type III hydrogen storage vessel. *Journal of Mechanical Science and Technology*, 32:1995–2002, 2018.

- [141] Uttam S Koruche and Subhas F Patil. Application of classical lamination theory and analytical modeling of laminates. *International Research Journal of Engineering and Technology*, 2(02):958, 2015.
- [142] Shan Jin, Peng Cheng, Yong Bai, Jeom Kee Paik, and Jun Li. Progressive failure analysis and burst mode study of Type IV composite vessels. *Ships and Offshore Structures*, 19(2):223–232, 2024.
- [143] Cheol Won Kong, Jong Hoon Yoon, Young Soon Jang, and Yeong Moo Yi. Design of composite pressure vessels with metallic and plastic liners. *Key Engineering Materials*, 261:1505–1510, 2004.
- [144] Dennis Menge and Hans-Joachim Schmid. Low temperature laser sintering with PA12 and PA6 on a standard system. 404(1):2100397, 2022.
- [145] Chufeng Dong, Yitao Liu, Jiepu Li, Guangfu Bin, Chilou Zhou, Wulin Han, and Xiang Li. Hydrogen permeability of polyamide 6 used as liner material for Type IV on-board hydrogen storage cylinders. *Polymers*, 15(18):3715, 2023.
- [146] Yu Sun, Hong Lv, Wei Zhou, and Cunman Zhang. Research on hydrogen permeability of polyamide 6 as the liner material for Type IV hydrogen storage tank. *International Journal of Hydrogen Energy*, 45(46):24980–24990, 2020.
- [147] Toray. Carbon fiber T700S. 2018.
- [148] Autar K Kaw and Francis Group. *Composite*. Taylor & Francis, second edition, 2006.
- [149] Lei Zu, Hui Xu, Xiaolong Jia, Qian Zhang, Huabi Wang, and Bingzhan Zhang. Winding path design based on mandrel profile updates of composite pressure vessels. Composite Structures, 235:111766, 2020.
- [150] Wenbo Li, Leiqi Zhang, Hong Lv, Lijun Zhang, Min Liu, Cunman Zhang, and Pengfei He. Reliability analysis of hydrogen storage composite pressure vessel with two types of random-interval uncertainties. *International Journal of Hydrogen Energy*, 48(81): 31685–31699, 2023.
- [151] Yehia Abdel-Nasser, Ahmed MH Elhewy, and Islam Al-Mallah. Impact analysis of composite laminate using finite element method. Ships and Offshore Structures, 12 (2):219–226, 2017.
- [152] Weili Jiang, Fengmin Du, Klaus Drechsler, and Jinyang Zheng. Combined composites layup architecture and mechanical evaluation of Type IV pressure vessels: A novel analytical approach. *International Journal of Hydrogen Energy*, 48(46): 17565–17576, 2023.

- [153] A Tasdemirci and G Tunusoglu. Experimental and numerical investigation of the effect of interlayer on the damage formation in a ceramic/composite armor at a low projectile velocity. *Journal of Thermoplastic Composite Materials*, 30(1):88–106, 2017.
- [154] Xiulei Wang, Mingming Tian, Xuedong Chen, Pengcheng Xie, Jianing Yang, Junxiang Chen, and Weimin Yang. Advances on materials design and manufacture technology of plastic liner of Type IV hydrogen storage vessel. *International Journal of Hydrogen Energy*, 47(13):8382–8408, 2022.
- [155] Guanjun Liu, Fan Yang, Wenbo Liu, Yujiao Bai, Chuang Han, Weicheng Jiao, Peipei Wang, and Rongguo Wang. Ultra-high gas barrier composites with aligned graphene flakes and polyethylene molecules for high-pressure gas storage tanks. *Journal of Energy Storage*, 40:102692, 2021.
- [156] Christoph Habel, Evgeny S Tsurko, Renee L Timmins, Julia Hutschreuther, Raphael Kunz, Dominik D Schuchardt, Sabine Rosenfeldt, Volker Altstädt, and Josef Breu. Lightweight ultra-high-barrier liners for helium and hydrogen. Acs Nano, 14(6): 7018–7024, 2020.
- [157] Hafiz Usman Khalid, Mokhtar Che Ismail, and Norlin Nosbi. Permeation damage of polymer liner in oil and gas pipelines: A review. *Polymers*, 12(10):2307, 2020.
- [158] Zhengyun Hu, MingHe Chen, Lei Zu, Xiaolong Jia, Anlei Shen, Qiang Yang, and Ke Xu. Investigation on failure behaviors of 70 MPa Type IV carbon fiber overwound hydrogen storage vessels. *Composite Structures*, 259:113387, 2021.
- [159] PJ Antunes, Gustavo R Dias, JP Nunes, FWJ Van Hattum, and T Oliveira. Finite element modelling of thermoplastic matrix composite gas cylinders. *Journal of Thermoplastic Composite Materials*, 21(5):411–441, 2008.
- [160] Shitanshu Sapre, Kapil Pareek, and Mayank Vyas. Investigation of structural stability of Type IV compressed hydrogen storage tank during refueling of fuel cell vehicle. *Energy Storage*, 2(4):150, 2020.
- [161] Mauro Profaizer. Passive barrier assessment of PET bottles through an FEM simulation of gas permeability. Excerpt from the proceedings of the COMSOL multiphysics user's conference, 2005.
- [162] S Villalonga, C Thomas, C Nony, F Thiebaud, M Geli, A Lucas, K Knobloch, and C Maugy. Applications of full thermoplastic composite for Type IV 70 MPa high pressure vessels. *International Conference on Composite Materials*, 2011.
- [163] Sung Min Cho, Kwang Seok Kim, Wanjin Kim, and Sung Joon Choi. Application of PET as a non-metallic liner for the 6.8 L Type-4 cylinder based on the hydrogen cycling test. *International Journal of Hydrogen Energy*, 47(10):6965–6973, 2022.

- [164] Sung Min Cho, Changjong Kim, Kwang Seok Kim, and Dong Kyu Kim. Lightweight hydrogen storage cylinder for fuel cell propulsion systems to be applied in drones. *International Journal of Pressure Vessels and Piping*, 194:104428, 2021.
- [165] Roger E Eckert and Tito T Serafini. Effect of film processing on cryogenic properties of poly (ethylene terephthalate). *Journal of Macromolecular Science*, *Part B*, 1(4): 695–708, 1967.
- [166] Béla Sebők, Gábor Kiss, Gábor Dobos, Ferenc Réti, Tamás Majoros, and Olga H Krafcsik. Novel instrument and method for the investigation of small permeation fluxes of gases through different membranes. Measurement, 46(9):3516–3524, 2013.
- [167] Julien Bayle, Dominique Perreux, David Chapelle, Frédéric Thiébaud, Mahytec Dole France, Philippe Nardin, Université De Franche, and Comté France. A model to predict the permeation of Type IV hydrogen tanks. *Energy*, 78:1–7, 2010.
- [168] Bruno Flaconnèche, Joseph Martin, and M-Helene Klopffer. Permeability, diffusion and solubility of gases in polyethylene, polyamide 11 and poly (vinylidene fluoride). Oil & Gas Science and Technology, 56(3):261–278, 2001.
- [169] TQ Hua, RK Ahluwalia, J-K Peng, Matt Kromer, Stephen Lasher, Kurtis McKenney, Karen Law, and Jayanti Sinha. Technical assessment of compressed hydrogen storage tank systems for automotive applications. *International Journal* of Hydrogen Energy, 36(4):3037–3049, 2011.
- [170] Jens Humpenöder. Gas permeation of fibre reinforced plastics. *Cryogenics*, 38(1): 143–147, 1998.
- [171] Philippe Berne Cea, Mathilde Weber, Air Liquide, Gilles Hochstetter Arkema, Eliane Espuche, and Insa Lyon. Polymer pipes for distributing mixtures of hydrogen and natural gas: Evolution of their transport and mechanical properties after an ageing under an hydrogen environment. *Energy*, 78:1–7, 2010.
- [172] Suyeon Lee, Hye Seong Han, Jae Hyo Lee, Jaehoon Jeong, and Dong Gi Seong. EPDM rubber-reinforced PA6/EVOH composite with enhanced gas barrier properties and injection moldability for hydrogen tank liner. Fibers and Polymers, 1-9, 2024.
- [173] Jagath Narayana Kamineni and Ramesh Gupta Burela. Modeling, fabrication, and burst testing of Type-IV 3D printed plastic liner composite overwrapped pressure vessels. *International Journal on Interactive Design and Manufacturing*, 1-10, 2024.
- [174] Somen K Bhudolia, Goram Gohel, Kah Fai Leong, and Aminul Islam. Advances in ultrasonic welding of thermoplastic composites: A review. *Materials*, 13(6):1284, 2020.

- [175] Shinji Kanehashi and Kazukiyo Nagai. Analysis of dual-mode model parameters for gas sorption in glassy polymers. *Journal of Membrane Science*, 253(1-2):117–138, 2005.
- [176] Liangbiao Chen, Jiang Zhou, Hsing-wei Chu, Guoqi Zhang, and Xuejun Fan. Modeling nonlinear moisture diffusion in inhomogeneous media. *Microelectronics Reliability*, 75:162–170, 2017.
- [177] Hiroyuki Kanesugi, Keiko Ohyama, Hirotada Fujiwara, and Shin Nishimura. High-pressure hydrogen permeability model for crystalline polymers. *International Journal of Hydrogen Energy*, 48(2):723–739, 2023.
- [178] Abtin Ebadi Amooghin, Pardis Moradi Shehni, Ali Ghadimi, Mohtada Sadrzadeh, and Toraj Mohammadi. Mathematical modeling of mass transfer in multicomponent gas mixture across the synthesized composite polymeric membrane. *Journal of Industrial and Engineering Chemistry*, 19(3):870–885, 2013.
- [179] Mathias Bouquerel, Thierry Duforestel, Dominique Baillis, and Gilles Rusaouen. Mass transfer modeling in gas barrier envelopes for vacuum insulation panels: A review. Energy and Buildings, 55:903–920, 2012.
- [180] AS Maxwell and SJ Roberts. Review of data on gas migration through polymer encapsulants. Serco Ltd.: Osfordshire, UK, 2008.
- [181] Yoshinori Kamiya, Yasutoshi Naito, Keishin Mizoguchi, Katsuhiko Terada, and Johann Moreau. Thermodynamic interactions in rubbery polymer/gas systems. *Journal of Polymer Science Part B: Polymer Physics*, 35(7):1049–1053, 1997.
- [182] Jaymin C Shah. Analysis of permeation data: Evaluation of the lag time method. *International Journal of pharmaceutics*, 90(2):161–169, 1993.
- [183] Jean-Claude Grandidier, Cédric Baudet, Séverine AE Boyer, Marie-Hélène Klopffer, and Laurent Cangémi. Diffuso-kinetics and diffuso-mechanics of carbon dioxide/polyvinylidene fluoride system under explosive gas decompression: Identification of key diffuso-elastic couplings by numerical and experimental confrontation. Oil & Gas Science and Technology, 70(2):251–266, 2015.
- [184] RI Hickson, SI Barry, and GN Mercer. Critical times in multilayer diffusion, Part 2: Approximate solutions. *International Journal of Heat and Mass Transfer*, 52(25-26): 5784–5791, 2009.
- [185] Johannes Macher, Andreas Hausberger, Astrid E Macher, Matthias Morak, and Bernd Schrittesser. Critical review of models for H2-permeation through polymers with focus on the differential pressure method. *International Journal of Hydrogen Energy*, 46(43):22574–22590, 2021.

- [186] SC Fraga, M Monteleone, M Lanč, E Esposito, A Fuoco, L Giorno, K Pilnáček, K Friess, M Carta, NB McKeown, et al. A novel time lag method for the analysis of mixed gas diffusion in polymeric membranes by on-line mass spectrometry: Method development and validation. *Journal of Membrane Science*, 561:39–58, 2018.
- [187] Marcello Monteleone, Elisa Esposito, Alessio Fuoco, Marek Lanč, Kryštof Pilnáček, Karel Friess, Caterina Grazia Bezzu, Mariolino Carta, Neil Bruce McKeown, and Johannes Carolus Jansen. A novel time lag method for the analysis of mixed gas diffusion in polymeric membranes by on-line mass spectrometry: Pressure dependence of transport parameters. *Membranes*, 8(3):73, 2018.
- [188] Jason K Lee, Selina X Yao, Guangming Li, Martin BG Jun, and Patrick C Lee. Measurement methods for solubility and diffusivity of gases and supercritical fluids in polymers and its applications. *Polymer Reviews*, 57(4):695–747, 2017.
- [189] Jiro Seta and Taisuke Ito. Activation volume for the diffusion of dye molecule in poly (ethylene terephthalate). Sen'i Gakkaishi, 38(5):T214–T223, 1982.
- [190] Yasutoshi Naito, Dominique Bourbon, Katsuhiko Terada, and Yoshinori Kamiya. Permeation of high-pressure gases in poly (ethylene-co-vinyl acetate). *Journal of Polymer Science Part B: Polymer Physics*, 31(6):693–697, 1993.
- [191] Viacheslav Balobanov, Tuukka Verho, Vuokko Heino, Helena Ronkainen, and Jani Pelto. Micromechanical performance of high-density polyethylene: Experimental and modeling approaches for HDPE and its alumina-nanocomposites. *Polymer Testing*, 93:106936, 2021.
- [192] Z Mogri and DR Paul. Gas sorption and transport in side-chain crystalline and molten poly (octadecyl acrylate). *Polymer*, 42(6):2531–2542, 2001.
- [193] Peyman Memari, Véronique Lachet, and Bernard Rousseau. Gas permeation in semicrystalline polyethylene as studied by molecular simulation and elastic model. Oil & Gas Science and Technology, 70(2):227–235, 2015.
- [194] M Hedenqvist and UW Gedde. Diffusion of small-molecule penetrants in semicrystalline polymers. *Progress in Polymer Science*, 21(2):299–333, 1996.
- [195] Elham Rezvanpanah and S Reza Ghaffarian Anbaran. The effect of crystallinity on cell growth in semi-crystalline microcellular foams by solid-state process: Modeling and numerical simulation. *Materials Research Express*, 4(11):115305, 2017.
- [196] Salman Shafqat, Olaf Van der Sluis, Marc Geers, and Johan Hoefnagels. A bulge test based methodology for characterizing ultra-thin buckled membranes. Thin Solid Films, 660:88–100, 2018.
- [197] Winoj Balasooriya, Clara Clute, Bernd Schrittesser, and Gerald Pinter. A review on applicability, limitations, and improvements of polymeric materials in high-pressure hydrogen gas atmospheres. *Polymer Reviews*, 62(1):175–209, 2022.

- [198] Muhuo Yu, Liangliang Qi, Lele Cheng, Wei Min, Zhonghao Mei, Ruize Gao, and Zeyu Sun. The effect of cooling rates on thermal, crystallization, mechanical and barrier properties of rotational molding polyamide 11 as the liner material for high-capacity high-pressure vessels. *Molecules*, 28(6):2425, 2023.
- [199] A Hamidi, Sedigheh Farzaneh, Fabien Nony, Zaida Ortega, Sofiane Khelladi, M Monzon, Farid Bakir, and Abbas Tcharkhtchi. Modelling of sintering during rotational moulding of the thermoplastic polymers. *International Journal of Material Forming*, 9:519–530, 2016.
- [200] RS Gaisin, V Yu Tyukanko, and AV Demyanenko. Developing a method for ultrasonic quality control of plastic products obtained by rotary moulding method. Russian Journal of Nondestructive Testing, 57(11):962–967, 2021.
- [201] Brendan R Murray, Sean B Leen, and CM Ó Brádaigh. Void distributions and permeability prediction for rotationally moulded polymers. Proceedings of the Institution of Mechanical Engineers, Part L, Journal of Materials: Design and Applications, 229(5):403-418, 2015.
- [202] Ying Su, Hong Lv, Cong Feng, and Cunman Zhang. Hydrogen permeability of polyamide 6 as the liner material of Type IV hydrogen storage tanks: A molecular dynamics investigation. *International Journal of Hydrogen Energy*, 50:1598–1606, 2024.
- [203] Qing Fang and Dongmei Ji. Molecular simulation of hydrogen permeation behavior in liner polymer materials of Type IV hydrogen storage vessels. *Mater Today Commun*, 35:106302, 2023.
- [204] Melanie Gregoire. The gas phase fluorination of high density polyethylene. PhD thesis, United Kingdom, 1997.
- [205] Zeping Jin, Ying Su, Hong Lv, Min Liu, Wenbo Li, and Cunman Zhang. Review of decompression damage of the polymer liner of the Type IV hydrogen storage tank. *Polymers*, 15(10):2258, 2023.
- [206] Ivan Blagojević and Saša Mitić. Hydrogen as a vehicle fuel. Mobility and Vehicle Mechanics, 44(2):37–49, 2018.
- [207] Maximiliano Melnichuk, Quentin Gardavaud, Frédéric Thiébaud, and Dominique Perreux. Numerical assestments of maximum depressurisation rate for polymer materials under high-pressure hydrogen. *International Journal of Hydrogen Energy*, 46(53):27088–27095, 2021.
- [208] Paweł Gąsior, Karol Wachtarczyk, Aleksander Błachut, Jerzy Kaleta, Neha Yadav, Marcin Ozga, and Amelie Baron. Validation of selected optical methods for assessing polyethylene (PE) liners used in high pressure vessels for hydrogen storage. Applied Sciences, 11(12):5667, 2021.

- [209] Matthew J Lohr, Gabriella P Sugerman, Sotirios Kakaletsis, Emma Lejeune, and Manuel K Rausch. An introduction to the Ogden model in biomechanics: Benefits, implementation tools and limitations. *Philosophical Transactions of the Royal* Society A, 380(2234):20210365, 2022.
- [210] Luli Li and Marc Masen. A new method for determining the Ogden parameters of soft materials using indentation experiments. *Journal of the mechanical behavior of biomedical materials*, 155:106574, 2024.
- [211] Atsushi Koga, Tadahisa Yamabe, Hiroyuki Sato, Kenichi Uchida, Junichi Nakayama, Junichiro Yamabe, and Shin Nishimura. A visualizing study of blister initiation behavior by gas decompression. *Tribology*, 8(1):68–75, 2013.

Chapter A

Appendix

A.1 CFRP Winding Sequence Used for FW on Liner-boss Assembly of Type IV COPV

Sr.	n	Layer Type	Material	WA (\circ)	BW (mm)	N_s (-)
1	1-4	Hoop	CFRP	89.85	2.01	1
2	5, 6	Helical	CFRP	25.00	2.01	1
3	7-10	Hoop	CFRP	89.85	2.01	1
4	11, 12	Helical	CFRP	25.00	2.01	1
5	13	Hoop	CFRP	89.85	2.01	1
6	14, 15	Helical	CFRP	25.00	2.01	1
7	16, 17	Hoop	CFRP	89.85	2.01	1
8	18-20	Helical	CFRP	25.00	2.01	1
9	21	Hoop	CFRP	89.85	2.01	1
10	22-24	Helical	CFRP	25.00	2.01	1
11	25	Hoop	CFRP	89.85	2.01	1
12	26-28	Helical	CFRP	25.00	2.01	1
13	29	Hoop	CFRP	89.85	2.01	1
14	30-32	Helical	CFRP	25.00	2.01	1
15	33	Hoop	CFRP	89.85	2.01	1
16	34-36	Helical	CFRP	25.00	2.01	1
17	37	Hoop	CFRP	89.85	2.01	1
18	38-40	Helical	CFRP	25.00	2.01	1
19	41	Hoop	CFRP	89.85	2.01	1
20	42-44	Helical	CFRP	25.00	2.01	1
21	45	Hoop	CFRP	89.85	2.01	1
22	46-48	Helical	CFRP	25.00	2.01	1
23	49	Hoop	CFRP	89.85	2.01	1
24	50-52	Helical	CFRP	25.00	2.01	1
25	53	Hoop	CFRP	89.85	2.01	1
26	54-56	Helical	CFRP	25.00	2.01	1
27	57	Hoop	CFRP	89.85	2.01	1
28	58-60	Helical	CFRP	25.00	2.01	1
29	61	Ноор	CFRP	89.85	2.01	1
30	62-64	Helical	CFRP	25.00	2.01	1
31	65	Hoop	CFRP	89.85	2.01	1
32	66-68	Helical	CFRP	25.00	2.01	1
33	69	Hoop	CFRP	89.85	2.01	1
34	70-72	Helical	CFRP	25.00	2.01	1
35	73	Hoop	CFRP	89.85	2.01	1

Sr.	n	Layer Type	Material	WA (\circ)	BW (mm)	$N_s \text{ (mm)}$
36	74-76	Helical	CFRP	25.00	2.01	1
37	77	Hoop	CFRP	89.85	2.01	1
38	78-80	Helical	CFRP	25.00	2.01	1
39	81	Hoop	CFRP	89.85	2.01	1
40	82-84	Helical	CFRP	25.00	2.01	1
41	85	Hoop	CFRP	89.85	2.01	1
42	86, 87	Helical	CFRP	25.00	4.00	2
43	88	Hoop	CFRP	89.85	4.00	2
44	89	Helical	CFRP	25.00	4.00	2
45	90	Hoop	CFRP	89.85	4.00	2
46	91	Helical	CFRP	25.00	4.00	2
47	92	Hoop	CFRP	89.85	4.00	2
48	93	Helical	CFRP	25.00	4.00	2
49	94	Hoop	CFRP	89.85	4.00	2
50	95	Helical	CFRP	25.00	4.00	2
51	96	Hoop	CFRP	89.85	4.00	2
52	97	Helical	CFRP	25.00	4.00	2
53	98	Hoop	CFRP	89.85	4.00	2
54	99	Helical	CFRP	25.00	4.00	2
55	100	Hoop	CFRP	89.85	4.00	2
56	101, 102	Helical	CFRP	25.00	4.00	2
57	103	Hoop	CFRP	89.85	4.00	2
58	104-112	Helical	CFRP	25.00	4.00	2

A.2 Finite Element Formulation of Hydrogen Transport Model for Polymeric Liners in Type IV COPVs

The FE equation for H_2 permeation is derived according to the standard FE formulation using Galerkin method. Let's consider a body with volume V bounded by surface S which consists of a part S_c where the hydrogen concentration is prescribed and a part S_j where the flux through the surface is prescribed by value 'j' such that

$$J \cdot n = j$$

Parts of the surface are such that $S = S_c \bigcup S_j$.

Weak Form

The weak form of the governing differential equation is derived by multiplying the equation by a test function δC and integrating over the volume V. This results in the following equation:

$$\int_{V} \delta C \left\{ \frac{\partial C}{\partial t} - \nabla \cdot (D \nabla C) + \nabla \cdot \left(\frac{D C V_{H}}{R T} \nabla \sigma_{h} \right) \right\} dV = 0 \tag{A.1}$$

We know that,

$$\nabla \cdot (\delta C D \nabla C) = \nabla \delta C D \nabla C + \delta C \nabla \cdot (D \nabla C) \tag{A.2}$$

and

$$\delta C \nabla \cdot \left(\frac{DCV_H}{RT} \nabla \sigma_H \right) = \nabla \cdot \left(\delta C \frac{DCV_H}{RT} \nabla \sigma_H \right) - \nabla \delta C \cdot \frac{DCV_H}{RT} \nabla \sigma_H \tag{A.3}$$

$$\begin{split} \int_{V} \left\{ \delta C \frac{\partial C}{\partial t} - \nabla \cdot (\delta C D \nabla C) + \nabla \delta C \cdot (D \nabla C) + \nabla \cdot \left(\frac{\delta C D C V_{H}}{R T} \nabla \sigma_{h} \right) \right. \\ \left. - \nabla \delta C \cdot \left(\frac{D C V_{H}}{R T} \nabla \sigma_{h} \right) dV = 0 \end{split} \tag{A.4}$$

Applying Gauss Divergence Theorem

$$\int_{V} \left\{ \delta C \frac{\partial C}{\partial t} + \nabla \delta C \cdot (D \nabla C) - \nabla \delta C \cdot \left(\frac{DCV_{H}}{RT} \nabla \sigma_{h} \right) \right\} dV + \int_{S} \delta C j dS = 0$$
 (A.5)

From weak form derived earlier can be rewritten as

$$\int_{V} \delta C f dV - \int_{V} \nabla \delta C \cdot J dV + \int_{S} \delta C j dS = 0$$
 (A.6)

Here, f is the function of C and \dot{C} .

Incremental form

The incremental form of the equation is derived by expanding the equation in terms of the incremental changes in concentration ΔC and its rate of change $\Delta \dot{C}$. The incremental form of E=0 in C and \dot{C} is and j is known boundary condition. This results in the following equation:

$$E + \frac{\partial E}{\partial C}\Delta C + \frac{\partial E}{\partial \dot{C}}\Delta \dot{C} = 0 \tag{A.7}$$

$$\int_{V} \delta C f dV - \int_{V} \nabla \delta C \cdot J dV + \int_{A} \delta C j dS + \int_{V} \delta C \frac{\partial f}{\partial C} \Delta C dV - \int_{V} \nabla \delta C \frac{\partial J}{\partial C} \Delta C dV + \int_{V} \delta C \frac{\partial f}{\partial \dot{C}} \Delta \dot{C} dV = 0$$
(A.8)

$$\int_{V} \delta C \left[\dot{C} \right] dV + \int_{S} \delta C \, j dS - \int_{V} \nabla \delta C \cdot \left[-D \nabla C + \frac{DCV_{H}}{RT} \nabla \sigma_{h} \right] dV
- \int_{V} \nabla \delta C \cdot \left[-D \nabla + \frac{DV_{H}}{RT} \nabla \sigma_{h} \right] \Delta C dV + \int_{V} \delta C \Delta \dot{C} dV = 0$$
(A.9)

Discrete form

The discrete form of the equation is obtained by discretizing the weak form using the FE method. The interpolation function N_c is used to approximate the concentration C, and the gradient of the interpolation function B_c is used to approximate the gradient of C. The discrete form of the equation is given by:

$$\Delta C = N_c \{ \Delta C \}$$

$$\dot{\Delta C} = N_c \{ \Delta \dot{C} \}$$

$$\delta C = N_c \{ \delta C \}$$

and the gradient of shape function is

$$B_c = \nabla N_c \tag{A.10}$$

$$\nabla \sigma_H = [B_c] \{ \sigma_H \} \tag{A.11}$$

Rate of change of nodal mass concentration

$$\frac{\partial \{C\}}{\partial t} = \left\{\dot{C}\right\} \tag{A.12}$$

Since, previous equation holds for any δC , it must also hold for any δC . So,

$$\int_{V} N_{c} \dot{C} dV
+ \int_{S} N_{c} j dS
- \int_{V} B_{c}^{T} \cdot \left[-D_{eq} \nabla C + \frac{D_{eq} C V_{H}}{R T} \nabla \sigma_{h} \right] dV
- \int_{V} B_{c}^{T} \cdot \left[-D_{eq} \nabla + \frac{D_{eq} V_{H}}{R T} \nabla \sigma_{h} \right] N_{c} \Delta C dV
+ \int_{V} N_{c} \Delta \dot{C} N_{c} dV = 0$$
(A.13)

Matrix Form

The discrete form is then converted into a matrix form using the FE method. The matrix form is given by:

$$[M_c] \cdot \Delta \dot{C} + [K_1 + K_2] \cdot \Delta C = F \tag{A.14}$$

Where $[M_c]$, $[K_i]$ and [F] denote the concentration capacity matrix, mass diffusivity matrix, and H_2 flux matrix given by Eqn.

$$[M_c] = \int_V [N_c]^T [N_c] dV \tag{A.15}$$

$$K_1 = \int_V B_c^T D_{eq} N_c dV \tag{A.16}$$

$$K_2 = \int_V B_c^T \left[\frac{D_{eq} V_H}{RT} \nabla \sigma_h \right] N_c dV \tag{A.17}$$

$$F = -\int_{V} B_{c}^{T} \cdot \left[-D_{eq} \nabla C + \frac{D_{eq} C V_{H}}{RT} \nabla \sigma_{h} \right] dV + \int_{V} N_{c} \dot{C} dV + \int_{A} N_{c} j dS$$
 (A.18)

Time integration

The matrix form is then integrated in time using the finite difference method. The resulting equation is given by:

$$([M_c] + \Delta t[K])\{C\}^{t+\Delta t} = [M_c]\{C\}^t + \Delta t\{F\}$$
(A.19)

The time-varying hydrogen concentration is given by:

$$\left\{\dot{C}\right\} = \Delta t (\left\{\mathcal{C}\right\}_{t+\Delta t} - \left\{\mathcal{C}\right\}_{t}) \tag{A.20}$$

Final equation

The final equation that ensures the symmetry of the left part is given by:

$$(\Delta t[M] + [K_1])\{C\}_{t+\Delta t} = (\Delta t[M] - [K_2])\{C\}_t + [F]$$
(A.21)

This equation is used to solve the FE equation for H₂ permeation using the Abaqus FE software.